University of Southampton

Faculty of Physical Science & Engineering

Electronics and Computer Science

SPACE CHARGE BEHAVIOUR OF THICK OIL AND PRESSBOARD IN A HVDC CONVERTER TRANSFORMER

By

Bo Huang

A thesis submitted for the degree of Doctor of Philosophy

August 2018

Acknowledgements

Firstly, I would like to express my deep gratitude to my supervisors Prof. George Chen and Prof. Steve Gabriel. George always gives me patient guidance and essential suggestions on the research topic. Steve also gives me valuable suggestions to the project. Without their encouragement, guidance and support to the project, this thesis would not have reached its present form.

I would present my sincere appreciation to my colleagues Dr Zhiqiang Xu and Dr Miao Hao. Zhiqiang gave me great guidance on build of a new PEA system. A great thank to Miao for sharing his knowledge, experience and kindly support through my PhD study.

I am grateful to all my colleagues in the Tony Davies High Voltage Laboratory. Particular mention should go to the lab technical team of Neil Palmer, Mike Smith, Brian Rogers and Ian Virtanen, Mark Long and Charlie Reed, for their assistance in design and build of a new PEA system.

I would also like to express my gratitude to my colleagues Dr Kevin Goddard, Dr Chao Tang, Dr Xia Wang, Dr Matthew Praeger, Dr Ian Hosier, Dr Suvi Virtanen, Dr Xuan Wang, Dr Churui Zhou, Dr George Callender, Vaggelis Senis, Orestis Vryonis, Istebreq Saeedi, Allison Shaw, Ziyun Li, Sijun Wu and Qingbo Zhang for their kindly help and advice.

Finally, I would like to thank my parents for their love, patience, and understating through these years.

To all involved, thank you very much!

Bo

UNIVERSITY OF SOUTHAMPOTN

ABSTRACT

FACULTY OF PHYSICAL SCIENCES AND ENGINEERING

DEPARTMENT OF ELECTONICS AND COMPUTER SCIENCE

Doctor of Philosophy

SPACE CHARGE BEHAVIOUR OF THICK OIL AND PRESSBOARD IN A HVDC CONVERTER TRANSFORMER

By BO HAUNG

High Voltage Direct Current (HVDC) power transmission is essential for the development of long-distance power transmission. Within the HVDC conversion system, the most significant apparatus is a HVDC converter transformer. In converter transformers, on the one hand, the high operational electric field is desirable to decrease the dimension, weight, and material usage in converter transformers; on the other hand, the electric field must be lower compared to the dielectric strength to avoid the surface discharge or destructive breakdown of insulation materials. In addition the operation voltage, the electric field is also affected by space charge dynamics in insulation materials. For this reason, extensive efforts have been made to investigate space charge dynamics in the insulation material of converter transformers, such as the oil-impregnated paper. However, the space charge characteristics are not well understood for the thick oil and pressboard (PB) materials under a temperature gradient. Hence, a new purpose-built pulsed electroacoustic (PEA) system has been set up to measure the thick oil and PB space charge behaviour under a temperature gradient. This dissertation comprises the quantitative analysis of the space charge dynamics in thick oil and PB insulation materials under a temperature gradient through an experimental approach.

With the purpose-built PEA system, the influential factor of temperature gradient on dynamics of space charge in thick oil and PB has been investigated. The space charge measured from the PEA system depends on the acoustic wave propagation in the insulation materials. The temperature can affect the acoustic velocity and thus space charge distribution. Therefore, for a one-layer sample, the space charge recovery method under a temperature gradient is important to ensure that the correct space charge pattern is acquired. Furthermore, in multilayer

samples, an acoustic wave may experience different generation and transmission coefficients that lead to attenuation and dispersion after the propagation through the dispersive materials. Therefore, the space charge recovery method of multilayer samples under the temperature gradient is proposed.

With the proposed space charge recovery method under a temperature gradient, the space charge influential factors, such as temperature gradient and multilayer oil and PB, are investigated. Furthermore, the polarity reversal (PR) effect on dynamics of space charge in multilayer oil and PB under a temperature gradient is presented using an experimental approach. The measured space charge is further interpolated into the COMOSOL model to quantitatively evaluate the electric field oil and PB after PR. The difference between the electric field after PR calculated by the Maxwell-Wagner theory and space charge density is compared. The thickness effect on the space charge is investigated on two-layer oil and PB materials. The simulation model is also expanded into four and six layers for the electric field calculation based on the estimated space charge results.

Contents

List of Figures

List of Tables

Definitions and Abbreviations

AC\HVAC	Alternating current\ High voltage alternating current
Al	Aluminium
CSC	Current Sourced Converter technology
DC\HVDC	Direct current\ High voltage direct current
HV	High voltage
Hz	Hertz
IGBT	Insulated Gate Bipolar Transistor
kV	Kilovolt
LCC	Line commutated convertor
PEA	Pulsed electroacoustic method
PVDF	Polyvinylidene fluorid
VSC	Voltage source convertor
XLPE	Cross-linked polyethylene
ε	Permittivity
τ	Time constant
γ	Conductivity
E	Electric field
$q(t)$	Total charge amount
S	Electrode area
ε_0	Vacuum permittivity
ε_r	Relative permittivity
E_{max}	Maximum electric field
PR	Polarity reversal
PB	Pressboard
DP	Degree of polymerisation
AT	Ambient temperature
TG	Temperature gradient

Declaration of Authorship

I, Bo Huang, declare that the thesis entitled “Space charge behaviour of thick oil and pressboard in a HVDC converter transformer” and the work presented in it are my own and has been generated by me as the result of my own original research. I confirm that:

- This work was done wholly or mainly while in candidature for a research degree at this University;
- Where any part of this report has previously been submitted for a degree or any other qualification at this University or any other institution, this has been clearly stated;
- Where I have consulted the published work of others, this is always clearly attributed;
- Where I have quoted from the work of others, the source is always given. With the exception of such quotations, this report is entirely my own work;
- I have acknowledged all main sources of help;
- Where the report is based on work done by myself jointly with others, I have made clear exactly what was done by others and what I have contributed myself;
- Parts of this work have been published as::

Journals:

[1] B. Huang, M. Hao, J. Hao, J. Fu, Q. Wang, and G. Chen, “Space Charge Characteristics in Oil and Oil-Impregnated Pressboard Insulation and Electric Field Distortion after Polarity Reversal Operation,” *IEEE Trans. Dielectr. Electr. Insul.*, 2016.

[2] B. Huang, Z. Xu, M. Hao, and G. Chen, “Multilayers Oil and Oil-impregnated Pressboard Electric Field Simulation based on the Space Charge,” *IEEE Trans. Dielectr. Electr. Insul.*, 2018 (Submitted).

[3] C. Tang, B. Huang, M. Hao, Z. Xu, J. Hao, and G. Chen, “Progress of Space Charge Research on Oil-Paper Insulation Using Pulsed Electroacoustic Techniques,” *Energies*, vol. 9, no. 1, p. 53, 2016.

[4] J. Hao, B. Huang, G. Chen, J. Fu, G. Wu, and Q. Wang, “Space Charge Accumulation Behavior of Multilayer Structure Oil-paper Insulation and Its Effect on Electric Field Distribution,” *High Volt. Eng.*, vol. 43, no. 6, pp. 1973–1979, 2017.

[5] X. Wang, C. Tang, B. Huang, J. Hao, and G. Chen, “Review of Research Progress on the Electrical Properties and Modification of Mineral Insulating Oils Used in Power Transformers,” *Energies*, vol. 11, no. 3, pp. 1–31, 2018.

Conferences:

[6] B. Huang, M. Hao, G. Chen, J. Hao, J. Fu, and Q. Wang, “Space Charge Characteristics and the Electric Field Distortion after Polarity Reversal Operation in two Layers of Oil-impregnated Paper and Oil,” in *The 19th Internation Symposium on High Voltage Engineering,Pilsen,Czech Republic*, 2015.

[7] B. Huang, M. Hao, Z. Xu, G. Chen, C. Tang, and J. Hao, “Research on Thickness Ratio and Multilayers effect on the Oil and Paper Space Charge Distribution,” in *International Conference on Condition Monitoring and Diagnosis (CMD)*, 2016, pp. 40–43.

[8] B. Huang, M. Hao, Z. Xu, G. Chen, X. Wang, Q. Wang, and Y. Long, “Temperature Gradient Effect on the Space Charge Behaviour in Thick Oil and Oil-impregnated Pressboard,” in *IEEE International Conference on Dielectric Liquids (ICDL)*, 2017, pp. 1–5.

[9] B. Huang, M. Hao, Z. Xu, G. Chen, X. Wang, C. Tang, J. Hao, and Q. Wang, “Effect of Temperature gradient on Space Charge in Multilayers Pressboard Oil and Pressboard System,” in *IEEE Conference on Electrical Insulation and Dielectric Phenomenon (CEIDP)*, 2017, pp. 74–77.

[10] B. Huang, M. Hao, Z. Xu, G. Chen, and T. Chao, “Effect of Voltage Reversal on Space Charge in Oil and Oil-impregnated Pressboard under Temperature Gradient,” in *IEEE International Conference on the Properties and Application of Dielectric Materials (ICPADM)*, 2018, pp. 98–101.

[11] C. Tang, B. Huang, J. Hao, M. Hao, S. Guo, and G. Chen, “The Space Charge Behaviors of Insulation Paper immersed by Mineral Oil and MIDEL 7131 after Thermal Ageing,” in *International Conference on Condition Monitoring and Diagnosis (CMD)*, 2016, pp. 44–47

[12] Z. Xu, M. Hao, B. Huang, G. Chen, M. Praeger, and P. Lewin, “Space Charge Dynamics and Electric Field Distortion in the Laminated Insulation for HVDC Cable,” in *IEEE Conference on Electrical Insulation and Dielectric Phenomenon (CEIDP)*, 2017, vol. 3, pp. 605–608.

[13] Y. Hou, B. Huang, G. Chen, K. Ye, and X. Zhao, “The Improvement of the Pulsed-Electroacoustic (PEA) System Measurement from the Acoustic Wave Transportation Perspective,” in *International Conference on the Properties and Applications of Dielectric Materials (ICPADM)*, 2018, pp. 1063–1066.

Signed: _____

Date: _____

Chapter 1 Introduction

1.1 Space charge analysis within the converter transformer

High Voltage Direct Current (HVDC) power transmission has been applied for a long time and utilized in the long distance electric power transmission systems. Compared to High Voltage Alternating Current (HVAC) system, HVDC system has some advantages. Firstly, HVDC system can connect two large AC system, with different frequencies, without having to ensure synchronism and stability between them. Secondly, HVDC is more cost-efficient for long distance power transmission because only two conductors are employed by HVDC, compared to HVAC in which three cables are needed [1]. Thirdly, the fast control of converters within the HVDC system could quickly damp out the oscillation within the AC system [1]. The low cost, low electric losses and high reliability make HVDC power transmission technology as the main option especially for the long distance power transmission.

In recent years, the HVDC technology has been expanded to the modern power system including the energy storage, distribution power generation, wind farms and so on. Within these systems, the HVDC systems are operated in the harmony with the conventional AC power system, by introducing the AC-DC power conversion apparatus.

Within the conversion station, the most important apparatus are HVDC converters, which are connected with DC power transmission lines at both ends. The converter transformers mainly consist of the steel core, windings and insulation materials. The insulation materials are the combination of the oil and pressboard. The oil has the dual functions, served as the insulator and cooler. The insulation materials are the same as those used within the AC transformer. However, the applied stresses are different due to the valve winding of the converter transformer will withstand DC stress, AC stress and transient impulse voltages [2].

Under DC stress, the space charge formation has been regarded as major issues to affect the safe and reliable operation of converter transformers. The source of the space charge is either injected from electrodes or dissociated from ionization of impurities within the oil and oil-impregnated pressboard (PB) [3]. The existence of the space charge will distort the electric field distribution and lead to the local electric field enhancement, which could accelerate the degradation and lead to breakdown of insulation materials [4].

The space charge characteristics need to be carefully investigated in order to improve the life expectancy of the HVDC converter transformers. The space charge influential factors can be classified into three categories: the sample properties, the operation conditions and applied voltages. The sample properties include the degradation, moisture, thickness, and multilayers

structure. The operating conditions include temperature and humidity. The external voltage stresses include DC voltages, DC+AC voltages, transient impulse voltages and polarity reversal (PR) operation voltages.

Within above influential factors, less attention has been put on the temperature gradient effect that affects the space charge behaviour. The temperature gradient exists in all high voltage (HV) transformers including converter transformers. The mineral oil provides the dual functions of the insulator and cooling materials [5]. The oil inlet is always located at the bottom of the tank and the oil gradually circulates to the outlet at the top of the tank. Therefore, the temperature of the oil at the top parts is always higher than that at the bottom part of the transformer [6]. Moreover, the temperature gradient also presents between different voltage ratings of windings. The temperature of the low voltage winding near the core is higher compared with that of the high voltage winding, resulting in the temperature gradient across the intermediate insulation materials.

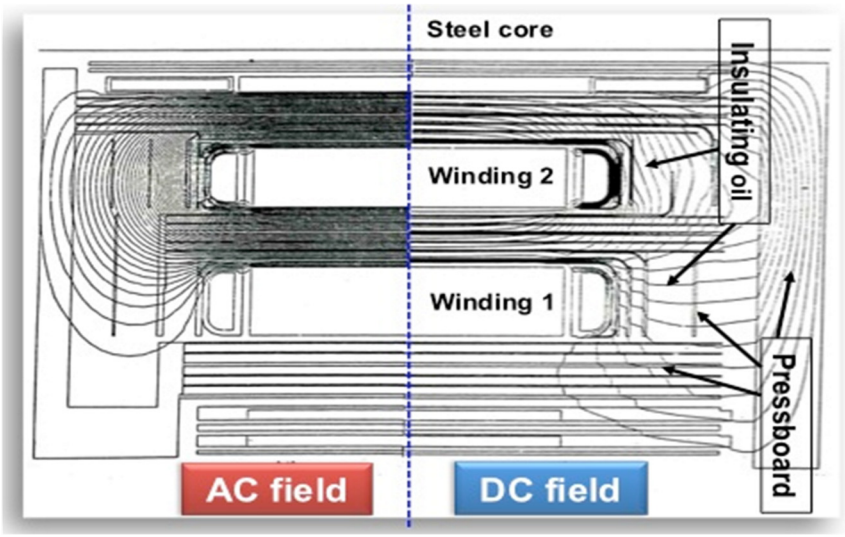

Figure 1-1: Different electric field distribution in a HVDC converter transformer between AC and DC voltage application [7].

Figure 1-1 shows the electric field distribution in a HVDC converter transformer and it is clear to see the difference of electric field distribution in oil and PB under AC and DC, separately. In a serviced converter transformer, the applied voltages include DC+AC voltages, transient impulse voltages and polarity reversal voltages. The maximum temperature is around 70 °C. The average DC electric field of 10 kV/mm is applied to the mixed oil and PB insulation system in a converter transformer [8]. Generally, in the oil and PB insulation system, the electric field distribution is related to the conductivity and permittivity of insulation materials based on Maxwell-Wagner theory. Under AC voltage or impulse voltage, the electric field is determined by the dielectric permittivity of the oil and pressboard. Under DC voltage, the electric field is determined by the conductivity of insulation materials. Therefore, the low permittivity of the oil will withstand the

higher voltage under the AC voltage while the major voltage will drop across in the PB due to its low conductivity.

As the conductivity is the function of both temperature and electric field [9], the steady state electric field of oil and PB calculated by conductivity is dependent on both temperature and external electric field. The different temperature can greatly vary the conductivity ratios between the oil and pressboard, thus affecting the electric field distribution within the converter transformers [10]. Therefore, it is advisable to conduct the calculations of field studies with various conductivity ratios, so that the worst situations can be identified [10] [11].

However, the existence of temperature gradient leads to the conductivity gradient. The discontinuous conductivity of the oil and PB will influence charge behaviour, which cannot be simply represented by various bulk conductivity ratios. Therefore, the temperature gradient effect on the space charge behaviour of oil and PB should be carefully investigated.

The equipotential lines under different voltage conditions for the parallel-lapped PB arranged within the oil are shown in Figure 1-2. When DC voltage is applied, the transient steady electric field is determined by the permittivity ratios of oil and PB. The electric field distribution can gradually change depending on the time constants to reach the steady state. Finally, the electric field of the oil/PB can be determined by the conductivity of oil/PB itself. The electric field during the polarity reversal (PR) depends on both permittivity and conductivity. During the PR operation, the existing of space charge cannot dissipate rapidly and it can create its own electric field superposed to the newly capacitive electric field after the polarity reversal operation. Consequently, the electric field in the oil gap is severely enhanced after the polarity reversal operation, which could be the most critical condition of the HVDC converter transformers [2] [9].

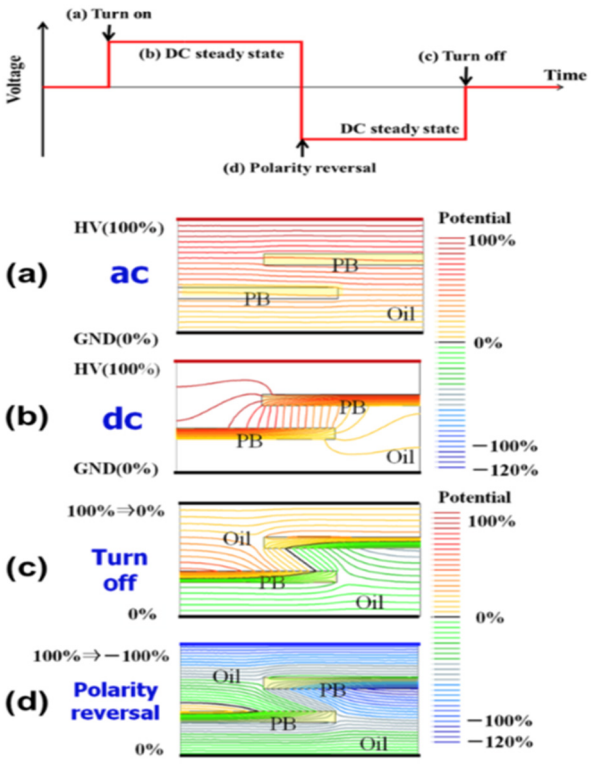

Figure 1-2: Electric field distribution under different voltage applications of oil/PB composite system [12].

Based on the above discussion, the temperature gradient and PR effect on the space charge behaviour of oil and PB should be carefully investigated. Moreover, the electric field simulation should be compared based on space charge and Maxwell-Wagner with the emphasis on the electric field after PR operation.

1.2 Research aims and objectives

The space charge data of oil-impregnated paper using pulsed electroacoustic (PEA) method was firstly presented in 1997 [13]. Since then, extensive space charge has been measured in past two decades in order to understand the correlation between the space charge characteristics and their influential factors. Currently, the majority of space charge measurement are carried out under the ambient temperature. As the temperature gradient is present in an operation converter transformer, the project research is aimed at a better knowledge and understanding of the space charge behaviour of thick oil and PB under the temperature gradient, to achieve safe and reliable operation of a converter transformer.

Due to the large attenuation and dispersion of acoustic wave during its propagation in oil and PB, the measurement of space charge in oil and paper is limited to the thickness around 200 um, which is smaller than that of the PB (≥ 1.0 mm) [14], typically used within the converter transformers.

With modifications of the previous PEA system, the current PEA system can measure the space charge with the maximum thickness up to 2 mm. However, for the thick PB such as 3 mm [9], it is still difficult to measure the space charge within the thick PB directly based on the current PEA equipment [8]. Therefore, it is desirable to propose a methodology that allows one to extend the space charge from the thinner oil and paper to the thicker ones, so that the electric field of the whole converter transformer could be estimated.

The following milestones were set for the dissertation:

- The design and build up of a new PEA system equipment capable of measuring the space charge under the temperature gradient
- The space charge recovery algorithm proposed to recover the space charge measurement under the temperature gradient.
- The understanding of the space charge behaviour of oil and PB under the temperature gradient
- The design of suitable test facility capable of measuring the PR voltage effect on the space charge characteristic of oil and PB under the temperature gradient.
- The implementation of a model to simulate the electric field of oil and PB considering the space charge effect.
- The methodology proposed to simulate the electric field of multilayers thick oil and PB considering the space charge effect.

1.3 Contributions of this research work

This dissertation contributes to the understanding of space charge behaviour in thick oil and PB through experimental investigations. The dynamics of space charge in oil and PB are firstly measured under the temperature gradient. The space charge results of oil/PB insulation will be experimentally obtained using the PEA method and they are incorporated in the simulation model. From the simulation, the electric field of two layers and multilayers oil/PB based on space charge is compared with the electric field based on the Maxwell-Wagner theory. The comparison results will be beneficial for the design and operation of converter transformers.

The equipment of the new PEA system is built up to measure the space charge of oil and PB under the temperature gradient. Compared with the conventional PEA system, the new PEA system can measure the space charge of thick oil and PB (<2mm) under the temperature gradient, which will be an important test facility to investigate the temperature gradient effect on the space charge characteristics of oil and PB in converter transformers.

The space charge recovery algorithm is proposed to recover the space charge under the temperature gradient. Based on the proposed recovery algorithm, the meaningful space charge

pattern can be collected for the electrically, acoustically and thermally inhomogeneous multilayers dielectric materials [15].

The temperature gradient effect on the space charge of oil and PB has been investigated. Under the temperature gradient, the experiment results reveal that a large amount of the space charge can be injected from the high temperature electrode. Extensive experiment efforts have been made to explain this phenomenon by using multilayers structure including one layer PB, two layers oil/PB and three layers PB/oil/PB. Experiment results show that a large amount of space charge can be injected due to the temperature gradient across the multilayers samples, which could severely distort the local electric field distribution.

The equipment capable of measuring voltage reversal effect on the space charge is set up. The polarity reversal effect on the space charge characteristics under the temperature gradient is observed in experiments. For two layers oil and PB, after the PR, the electric field of the oil increases under the temperature gradient while that decreases under the ambient temperature. More attention should be focused on the steady state electric field under the temperature gradient. The 'mirror image charge' cannot be seen with the voltage reversed from (+) to (-) under the temperature gradient effect due to the polarity effect under the temperature gradient. For the multilayers PB/oil/PB, a 'mirror image charge' can be seen with the comparison of the steady-state space charge under the voltage with different polarities under the temperature gradient.

The thickness effect on space charge behaviour is investigated under the ambient temperature. The same thickness ratios of the PB and oil could lead to approximately similar space charge distribution under the same external electric field. This allows us to extend the space charge from thinner samples to thicker samples. The methodology is proposed to simulate the electric field of two layers oil/PB and multilayers oil/PB with the consideration of the space charge effect. After polarity reversal, the oil electric field based on the space charge of two layers and multilayers is higher compared with that based on the Maxwell-Wagner theory.

1.4 Structure of the dissertation

This dissertation reports the investigations on space charge characteristics in oil and PB by experiments. The measured space charge is further incorporated into the numerical model to simulate multilayers layers electric field of oil and PB. This dissertation is divided into the following 8 chapters to describe the research work.

Chapter 1 introduces contributions and structure of the dissertation.

Chapter 2 reports the basics of space charge and existing research in oil and PB.

Chapter 3 describes the design of the new PEA system under the temperature gradient.

Chapter 4 reports the proposed space charge recovery algorithm to recover the space charge measurement under the temperature gradient.

Chapter 5 describes the space charge characteristics of oil and PB under the temperature gradient.

Chapter 6 reports the polarity reversal effect on the space charge behaviour under the temperature gradient.

Chapter 7 describes the electric field simulation of multilayers oil and PB calculated by the space charge and Maxwell-Wagner theory.

Chapter 8 summarizes the conclusions based on the above work and discusses the future work.

The detailed research was performed according to the following chapters:

Chapter 2 gives the brief introduction about converter technology: Current Source Convert (CSC) and Voltage Source Converter (VSC) are utilised in HVDC technology (Section 2.1). Within the conversion system, the most important apparatus are HVDC converter transformers. The insulation materials of oil and PB are described (Section 2.2). Considering the complex electric field including DC, AC and impulse voltage applied on the valve winding of converter transformers, the fundamental electric field calculation based on Maxwell-Wagner theory is introduced (Section 2.3). Under the DC voltage, the space charge existence can affect the safe and reliable operation of converter transformers. The existing space charge measurement techniques are reviewed including the most popular technique Pulsed electroacoustic (PEA) method (Section 2.4), as well as the basic space charge calibration method (Section 2.5). The general influential factors of space charge characteristics of oil and PB are discussed (Section 2.6).

Chapter 3 gives the design of the new PEA system capable of measuring the space charge characteristics under the temperature gradient. The PEA system consists of three different parts: the upper electrode, the bottom electrode and temperature control system (Section 3.1). The performance of the new PEA system is tested and technical test performance including the temperature and space charge measurement is summarised (Section 3.2).

Chapter 4 proposes the space charge recovery algorithm utilized for space charge recovery under the temperature gradient. The existing recovery technique for space charge under the temperature gradient is reviewed (Section 4.1). The one layer space charge recovery algorithm is proposed under the temperature gradient (Section 4.2). The more complex space charge recovery algorithm for multilayers is developed. The two-layer samples (Section 4.3) and three-layer samples (Section 4.4) space charge recovery algorithm are developed. Based on these methods, the correct space charge pattern can be collected for the electrically, acoustically and thermally

inhomogeneous multilayers dielectric materials [16].

Chapter 5 discusses the space charge characteristics of multilayers oil and PB under the temperature gradient. The space charge characteristic and electric field distribution of single layer PB under the temperature is presented (Section 5.1). Considering the multilayers structure of converter transformers, the oil and PB interface effect on the space charge behaviour is investigated. Two layers oil and PB (Section 5.2) and three layers PB/oil/PB (Section 5.3) space charge characteristics are further investigated.

Chapter 6 explores the polarity reversal effect on the space charge behaviour of oil and PB under the temperature gradient. The previous PR research has been reviewed and the motivations in this research has been introduced (Section 6.1). The experiment methodology has been proposed (Section 6.2). It is considered that temperature gradient, the polarity of voltage, PR time, the multilayers are dominated factors determining the transient electric field after PR. The above factors are investigated (Section 6.3). The experiment results are discussed and explained (Section 6.4).

Chapter 7 describes the electric field simulation of multilayers oil and PB considering the space charge effect. The transient and steady state electric field is calculated based on the existing Maxwell-Wagner theory (Section 7.1). The real electric field is dependent on the space charge distribution. The space charge is directly incorporated into a model to simulate the electric field of two layers oil and PB. From the simulation results, the transient and steady state electric field is calculated considering the space charge effect (Section 7.2). The thickness and multilayers effect on the space charge behaviour is investigated (Section 7.3). Based the space charge characteristics, the methodology is proposed to simulate the transient and steady state electric of multilayers thick oil and PB considering the space charge effect (Section 7.4).

Chapter 2 Space charge behaviours in converter transformers

2.1 Converter technology in the HVDC system

The HVDC transmission converter technology can be classified into two different categories: current source converter (CSC) and voltage source converter (VSC). Traditionally, the HVDC power scheme has utilized the thyristors with the DC current flowing in the same direction, which is called the CSC. In Figure 2-1(a), the scheme utilizes thyristors and a large inductor connected to the DC side. The inductor maintains the constant DC current. These thyristors are triggered by the gate pulse and are turned off when the current falls to zero. Therefore, the switching losses are quite low.

Since 2000, an alternative method based on large transistors called Insulated Gate Bipolar Transistors (IGBTs) have been used in the HVDC scheme called voltage source converters (VSC). In Figure 2-1 (b), the scheme uses IGBTs and large capacitors on the DC side, leading to constant DC voltage. IGBT can be turned on and off independently by their gate voltages. As the current is not zero when turning off, the switching losses are higher compared to CSC.

CSC have some obvious advantages. It can be made up to high power and DC voltage ratings. The thyristors are more robust with a significant transient overload capacity. The switching losses are low due to the current through thyristors dropping to zero when switching off. However, CSC still suffers from some disadvantages. The conventional valve hall and filters occupy a large area, increasing the investment cost. The filters are required to damp out some harmonics generated within the AC system. The harmonics lead to the commutation failure between different valves, which may be caused by the fault occurring on the AC network. The commutation between valves is required because of the synchronous drawing of reactive power for both rectifier and inverter at each end from the AC networks [1].

VSC have some obvious advantages. Firstly, the IGBT could connect any combination of the active and reactive power. Thus the VSC technology can connect the large two AC systems without guaranteeing the synchronism. Secondly, even if some faults occur on the AC networks, the VSC could still operate. Thirdly, VSC can generate good sine wave shape in the AC networks and thus less filters are required. However, low power rating and high switching losses of VSC are main obstacles to the development of the VSC [1].

For the PR operation based on the conventional CSC, in order to reverse load flow direction, the polarity of voltage needs to be reversed as the thyristor valves must carry the current in the same

direction. With the rise of the VSC with the IGBT switching transistors, the power flow direction can be reversed by reversing the current direction. Therefore, the polarity of the voltage is not required to be reversed any more [10].

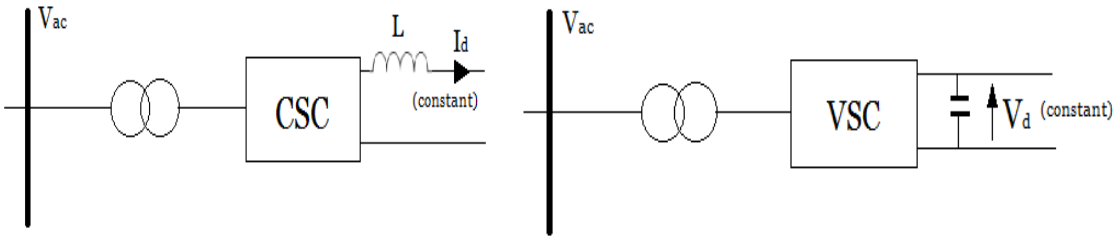

(a) Current source converter (CSC) (b)Voltage source converter (VSC)

Figure 2-1: The configuration of VSC and CSC [1].

2.2 Converter transformers insulation materials

The converter transformers are using oil and pressboard as the main insulation materials to meet the various needs for power transmission in HVDC power systems. The pressboard and oil are refined by industry procedures to produce the best electrical and mechanical properties of them. The fundamental aim of using these two materials is to separate regions of different electric areas and provide the mechanical support to the electrical system [14]. Each material contributes to the goals by providing complimentary electrical and mechanical functions and works in harmony with each other.

The oil and pressboard are selected as the main insulation materials based on the following reasons [14]:

- The pressboard possesses the excellent dielectric strength and low loss and its flexibility facilitates the insulation layers over the complex shapes.
- The insulation oil has the dual function as the coolant and insulator.
- With the impregnation of the oil and PB, the oil fills the space in the pressboard within transformers to prevent any formation of the gas void, which is a possible source of the partial discharge (PD) activity.

2.2.1 The pressboard

The pressboard is manufactured from the wood pulp, which largely consists of cellulose [10]. Cellulose is regarded as the condensation of the monomer of glucose [10]. The basic structure of cellulose is the glucose unit ($C_6H_{10}O_5$) shown in Figure 2-2 [17]. The glucose units connect together in a long chain to form the cellulose polymers with an atom of oxygen forming the link

between the glucose units.

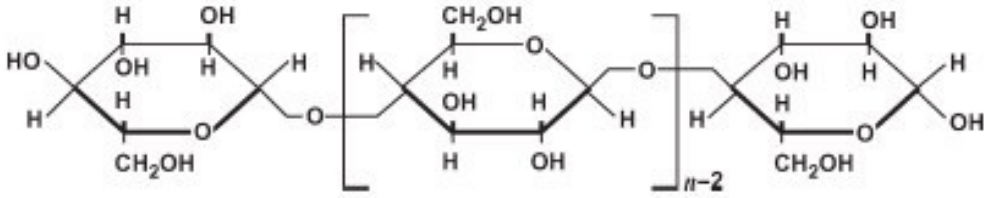

Figure 2-2: Cellulose polymer structure [17].

The pressboard is made of cellulose (40%-80%) , hemicelluloses (10%-40) and lignin (5-25%) [5] [6]. The intrinsic mechanical and electrical characteristics are determined by the polymer chain structure of cellulose molecules [14]. For example, the number of glucose units which form the cellulose polymer chain of pressboard is around 1200. The length of the polymer chain is characterised by the number of links (i.e. n-2) shown in Figure 2-2, which is called the degree of polymerisation (DP). The DP has become an effective diagnostic tool to indicate the degradation of the pressboard. The hemicellulose is the second significant component which facilitates the hydrogen bonding process [5]. The polymer chain is straight (i.e. not coiled) which allows parallel chains to cross link through hydrogen bonding between the polar hydroxyl groups. By this, crystalline areas are created which increase a fibrous structure with capillaries and create a large surface area [10]. This explains the hygroscopic character of cellulose, which means that the pressboard absorbs moisture easily [14]. Considering the lignin, it can bind the fibre to strengthen its matrix rigidity [18].

Some new types of the Nano-modified cellulose paper has been put forward recently in order to improve the electric properties of the paper. The general addition of the nanoparticles includes TiO_2、SiO_2、Al_2O_3、ZnO [20][21][22][23]. From some preliminary experimental results [24], the nano-TiO_2 paper with the mass fraction of 3% can prohibit the charge injection and improve the electric field distribution of the paper [24].

2.2.2 The mineral oil

Mineral oil is generated from refining natural crude petroleum [14]. Mineral oil can be classified into three hydrocarbon molecules groups: paraffins ($C_{2n}H_{2n}$), naphthenes ($C_{2n}H_{2n}$) and the aromatic compounds (C_nH_n). The molecular structures of three hydrocarbon groups can be seen in Figure 2-3. The paraffinic hydrocarbons consist of straight and branched hydrogen and carbon atoms. The naphthenic components have a saturated ring-like structure. The aromatic components contain the unsaturated ring-like structures where double bonds exist between different carbon atoms.

Long chain paraffins obstruct the flow of oil at the low temperature. As the insulation oil should be able to flow at the low temperature, the higher proportion of naphthenes should be included in the mineral oil [10] as the naphthenes can lead to low viscometric properties of the oil. Aromatic compounds can result in accelerated ageing on exposure to light and oxygen. They can oxidize to polar groups and chemically bond once the double bonds are broken or cross link with one another [10]. The proportions of aromatics should be less in order to achieve the long-term resistance to oxidation of mineral oil [25]. The aromatic compound has the property of gas absorbing behaviour, i.e. the aromatic compound can absorb the hydrogen generated from partial discharge.

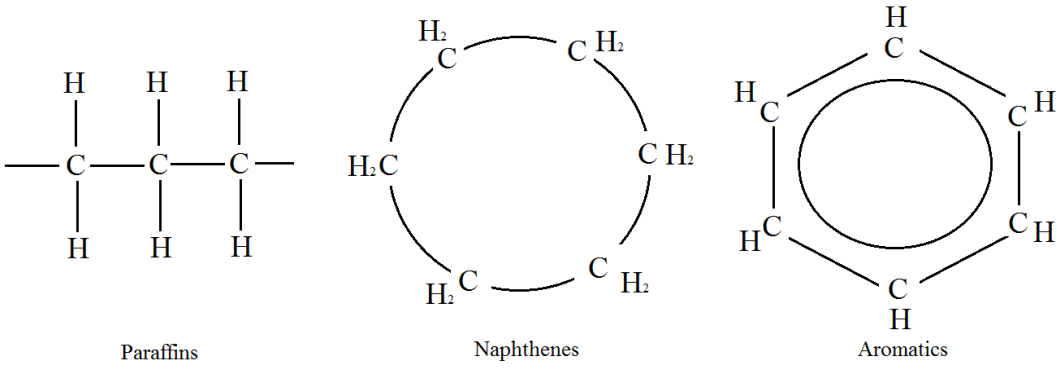

Figure 2-3: The three chemical components within the mineral oil [26].

Some other insulation oil includes the silicone oil, the natural ester oil, and nanocomposite oil. The silicone oil contains linear polymers of limited length without spatial cross-linkages [10]. The natural ester oil is from the chemical process of natural seed oils.

The natural ester oil has basic similarities and differences compared to the mineral oil:

- the breakdown strength is comparable;
- the natural ester is less stable under the oxidation;
- the natural ester can dissolve much water compared to mineral oil;
- the viscosity of the natural ester is higher compared to mineral oil;
- the pour point and flash point of natural ester oil are higher; the biodegradability is much better of the natural ester oil [27][28].

The nanocomposite oil contains the particles: Al_2O_3、 Fe_3O_4、 SiC、 TiO_2、SiO_2、 ZnO and MgO. From some preliminary results, the addition of nanoparticles can improve the thermal conductivity of the insulation oil [29]. However, more other properties such as ageing stability, the degree of nanoparticle agglomeration should be further investigated. Some researchers investigated to use the natural ester oil, silicone oil or nanocomposite oil to replace the mineral oil [30][31][32]. The motivations are cost reduction and environment concerns considering the

better biodegradability of natural ester oil. However, this dissertation concentrates mainly on mineral oil due to its wide usage.

2.3 The electric field and interfacial charge from Maxwell-Wagner theory

The configuration consist of two different samples "1" and "2" with the different conductivity γ and permittivity ε shown in Figure 2-4. Based on Maxwell-Wagner theory, the sample is regarded as the parallel of capacitor and resistor. The electric field of two layers based on Maxwell-Wagner theory can be calculated as follows:

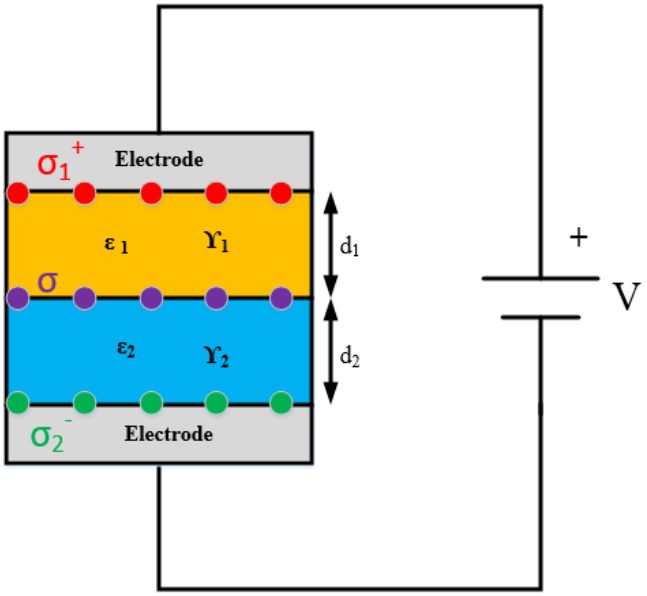

Figure 2-4: Two layers based on Maxwell-Wagner theory.

In stationary conduction field (at DC voltage):

$$J_{1n} = J_{2n} \tag{2-1}$$

where J represents conduction current.

In transient dielectric displacement field (at AC voltage):

$$D_{1n} = D_{2n} \tag{2-2}$$

where D is displacement flux.

The difference between the displacement densities D_{1n} and D_{2n} is equal to the surface charge density σ:

$$\sigma = D_{2n} - D_{1n} \tag{2-3}$$

According to equation (2-1):

$$D = \varepsilon E \tag{2-4}$$

$$J = \gamma E \tag{2-5}$$

The following equations (2-6) and (2-7) describe a parallel plate capacitor and resistor:

$$C = \frac{\varepsilon A}{d} \tag{2-6}$$

$$R = \frac{d}{\gamma A} \tag{2-7}$$

where A is the electrode area, d is the sample thickness.

For the configuration of two different dielectric materials, the electric field calculated based on the Maxwell-Wagner theory can be shown based on above equations (2-1) to (2-7) [33][34][35]:

$$E_1(t) = \frac{R_1 V}{(R_1 + R_2)d_1} + \left(\frac{C_2}{C_1 + C_2} - \frac{R_1}{R_1 + R_2}\right)\frac{V}{d_1} e^{\frac{-t}{\tau}} \tag{2-8}$$

$$E_2(t) = \frac{R_2 V}{(R_1 + R_2)d_2} + \left(\frac{C_1}{C_1 + C_2} - \frac{R_1}{R_1 + R_2}\right)\frac{V}{d_2} e^{\frac{-t}{\tau}} \tag{2-9}$$

where V is the applied voltage, the τ is the time constant:

$$\tau = \frac{C_1 + C_2}{\frac{1}{R_1} + \frac{1}{R_2}} \tag{2-10}$$

With the combination of equations (2-6), (2-7), (2-8), (2-9):

$$E_1(t) = \frac{\gamma_2}{\gamma_1 d_2 + \gamma_2 d_1} V(1 - e^{-\frac{t}{\tau}}) + \frac{\varepsilon_2}{\varepsilon_1 d_2 + \varepsilon_2 d_1} V e^{-\frac{t}{\tau}} \tag{2-11}$$

$$E_2(t) = \frac{\gamma_1}{\gamma_1 d_2 + \gamma_2 d_1} V(1 - e^{-\frac{t}{\tau}}) + \frac{\varepsilon_1}{\varepsilon_1 d_2 + \varepsilon_2 d_1} V e^{-\frac{t}{\tau}} \tag{2-12}$$

$$\tau = \frac{d_2\varepsilon_1 + d_1\varepsilon_2}{d_2\gamma_1 + d_1\gamma_2} \tag{2-13}$$

In dielectric displacement field (at AC voltage):

$$E_{1c} = \frac{\varepsilon_2}{\varepsilon_1 d_2 + \varepsilon_2 d_1} V \tag{2-14}$$

$$E_{2c} = \frac{\varepsilon_1}{\varepsilon_1 d_2 + \varepsilon_2 d_1} V \tag{2-15}$$

where E_{xc} is the capacitive electric field.

In the stationary conduction field (at DC voltage):

$$E_{1r} = \frac{\gamma_2}{\gamma_1 d_2 + \gamma_2 d_1} V \tag{2-16}$$

$$E_{2r} = \frac{\gamma_1}{\gamma_1 d_2 + \gamma_2 d_1} V \tag{2-17}$$

where E_{xr} is the resistive electric field.

The stationary state accumulated surface charge ${\sigma_1}^+$ and ${\sigma_2}^-$:

$${\sigma_1}^+ = \varepsilon_1 E_{1r} = \frac{\varepsilon_1 \gamma_2}{\gamma_1 d_2 + \gamma_2 d_1} V \tag{2-18}$$

$${\sigma_2}^- = \varepsilon_2 E_{2r} = \frac{\varepsilon_2 \gamma_1}{\gamma_1 d_2 + \gamma_2 d_1} V \tag{2-19}$$

Then stationary interface charge density:

$$\sigma = {\sigma_2}^- - {\sigma_1}^+ = \frac{\varepsilon_2 \gamma_1 - \varepsilon_1 \gamma_2}{\gamma_1 d_2 + \gamma_2 d_1} V \tag{2-20}$$

2.4 Space charge detection techniques

2.4.1 The evolution of the space charge detection techniques

Space charge has received wide attention from both industry and research institute. Extensive efforts have been made to improve the detection techniques of space charge distribution within dielectrics over the last two decades [36]. The early techniques include the dust figure method [37] and probe method [38]. These methods were destructive to the sample where cutting and sample preparation could affect the space charge distribution before the measurement. The first non-destructive technique for space charge in solids was proposed by Collins in the middle of 1970s [39]. After several decades of development, modern space charge detection techniques are divided into two categories: thermal, and acoustic. The thermal techniques involve the thermal expansion, resulted from the varied temperature of one or two surfaces of samples. Such thermal expansions result in a current containing the space charge distribution information. The current signal is processed by a mathematic deconvolution method and is transformed to the spatial charge distribution in the sample. The popular thermal methods include laser intensity modulation method (LIMM) [40], thermal pulse method (TPM) [41] and thermal step method (TSM) [42]. The acoustic technique generates a pressure wave to travel through charged dielectric materials. The propagation of the pressure wave leads to the displacement of the charge and induces an external current containing the space charge distribution information. Acoustic methods include laser induced pressure pulse (LIPP), piezoelectric induced pressure pulse (PIPP) and pressure wave propagation (PWP) methods [43]. The comparison between the PWP and PEA method could

be summarized in the Table 2-1 below. The widely used pulsed electro-acoustic method (PEA) method has its own typical features. The external pulse electric field induces a perturbing coulomb force on the space charge and generates an acoustic wave containing the space charge distribution. The acoustic wave detected by the piezoelectric transducer converts to an electric signal which is proportional to the acoustic wave signal. The electric signal is processed by a mathematic deconvolution method and is transformed into the spatial distribution of charge in samples.

Table 2-1: The comparison between PEA and PWP [44]

Categories	PEA	PIPP	LIPP
Sample thickness/ mm	0.1~20	0.1~1	0.05~20
Resolutions / μm	5	5	2
Detection signal	Voltage	Current	Current
Comments	Deconvolution is required	Resolution improved with deconvolution	No deconvolution required

2.4.2 The principle of pulsed electro-acoustic (PEA) method

A PEA system is composed of several parts shown in Figure 2-5. The system is mainly consisted of upper and ground electrodes, a coupling capacitor, a protective resistance, a piezoelectric transducer and an amplifier. The top electrode is made of brass and bottom electrode is made of aluminium (Al). A semiconducting (SC) layer is usually inserted between the sample and upper electrode to improve the acoustic impedance matching [36]. A sample is inserted between the and bottom electrode. The electrode should be adequately parallel to the sample to avoid any reflection of the acoustic wave at the air gap between the electrodes and sample. DC voltage and pulsed voltage are respectively applied to the sample through a protecting resistance and a coupling capacitor. The acoustic wave generated from the interaction between the pulsed electric field and space charge are detected by the piezoelectric transducer, which is attached to the ground Al electrode. The material of the piezoelectric transducer is polyvinylidene fluoride (PVDF). The PVDF sensor is an acoustic sensor to detect and convert the acoustic pressure to the electric signal. The thickness of the sensor is important to determine the resolution and sensitivity of the PEA system [43] [45]. After the PVDF sensor, an absorber made of the same acoustic property as the sensor is used to absorb the reflected acoustic wave. The output signal from transducer is then amplified by an amplifier and eventually displayed in the oscilloscope.

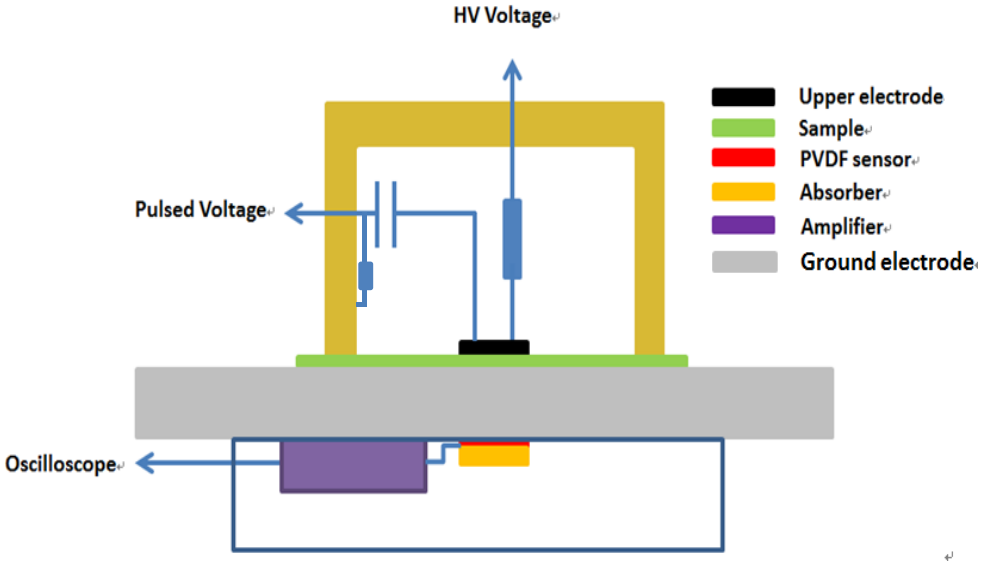

Figure 2-5: Typical structure of PEA system [8].

The principle of PEA system is illustrated in Figure 2-6. V_{dc} is the DC voltage; $\rho(t)$ is the charge distributed in the sample; $w(t)$ is the generated acoustic wave; $V_s(t)$ is the output voltage signal. After the application of the DC voltage V_{dc}, the space charge can be injected in the dielectric insulation materials [36]. When a pulse is applied, the pulsed field perturbs the charge on the surface of the specimen, generating acoustic wave $w(t)$. The acoustic wave propagates the sample and is detected by the PVDF sensor. The acoustic wave $w(t)$ converts to the electric signal $V_s(t)$, which is proportional to the acoustic wave. The electric signal $V_s(t)$ contains the magnitude and spatial distribution of the space charge information. Through the mathematic deconvolution method, the electric signal $V_s(t)$ is transformed into the spatial distribution of space charge density in dielectric materials.

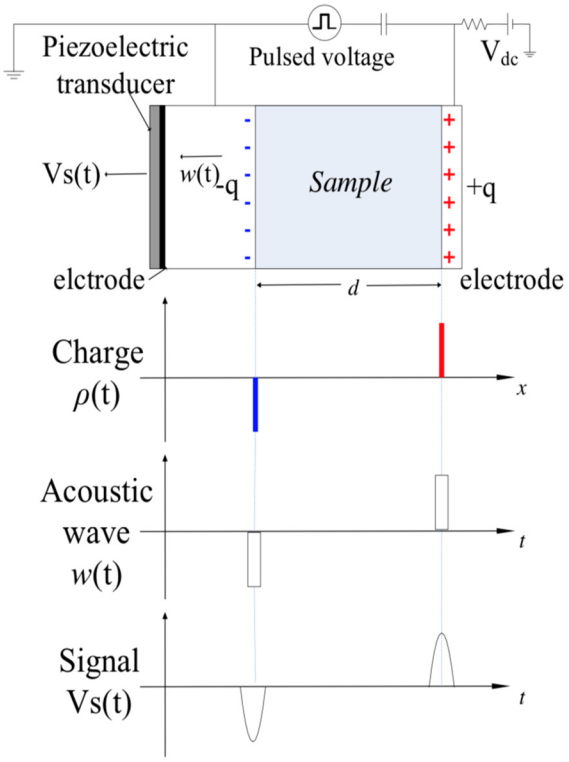

Figure 2-6: The principle of pulsed electro-acoustic method [36].

2.5 Space charge waveform recovery method

The PEA output signal does not directly represent the spatial charge distribution in samples. There are two main reasons. Firstly, the pulsed electric field perturbs internal charge and surface charge generating the acoustic wave. The acoustic wave travels through different materials before reaching the piezoelectric transducer, and may experience different generation, transmission, reflection, attenuation, and dispersion coefficients, leading to the difficulty of interpreting the original acoustic signal after the acoustic wave propagation process. Secondly, the acoustic wave detected by the piezoelectric transducer converts to the electric signal. The capacitance of piezoelectric transducer and resistance of the amplifier forms the high pass filter circuit. Due to the limitation of the frequency response of the piezoelectric transducer and the unit of the amplifier, the PEA output signal always presents the overshoot peak after the entry peak representing the charge of the ground electrode shown in Figure 2-7. The overshoot peak does not represent the real charge and should be removed from the output signal for space charge evaluation. Thus a mathematic deconvolution is used to gain the transfer function, and is implemented to transform the electric signal to space charge results shown in Figure 2-8 [36].

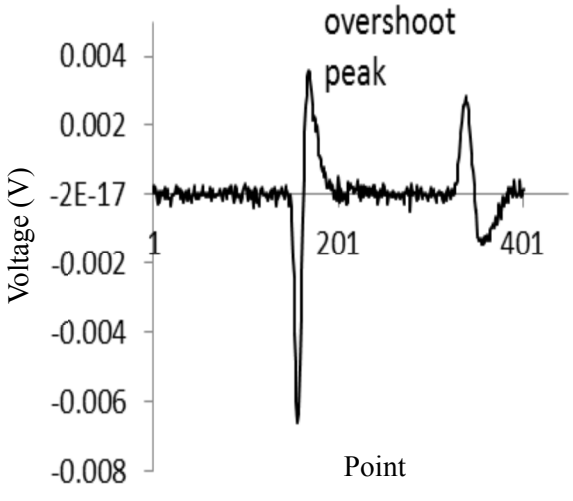

Figure 2-7: A typical PEA output signal [36].

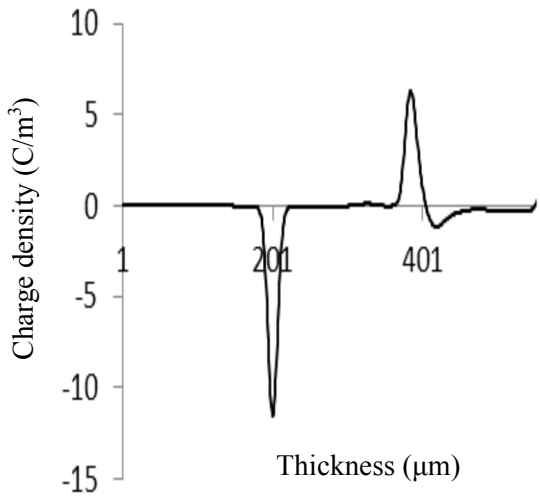

Figure 2-8: A profile of calibrated signal [36].

A Numerical algorithm has been made to recover the space charge under ambient temperature from the acoustic perspective. Li et al. [46] and Vazquez et al. [47] proposed the space charge recovery method for a one-layer sample under the ambient temperature. The attenuation and dispersion of the acoustic recovery have been considered. The new transfer function has been acquired to recover the space charge of a one-layer sample under the ambient temperature. For the two layers of space charge recovery, Wu et al. [34] and Tang et al. [48] proposed the space charge recovery method. The attenuation and dispersion of each dielectric material have been calculated separately to gain the transfer function, which is used to make the acoustic wave recovery. The transportation of the acoustic wave in two layers has been studied in terms of the acoustic wave generation, propagation, and reflection phenomena. For multilayers space charge recovery, Bodega [16] proposed the space charge recovery method of multilayers samples under the ambient temperature. The interface on acoustic wave generation, propagation and reflection have been carefully investigated.

Several efforts have also been made to recover the space charge under the temperature gradient from the acoustic perspective. Wang et al. [49] proposed one layer space charge recovery under the temperature gradient. However, the recovery methodology does not consider the acoustic wave attenuation and dispersion under the temperature gradient. Zhu et al. [50] and Wang et al. [51] proposed the new method to recover the space charge of one layer sample under the temperature gradient. The attenuation factor $\alpha(f, z)$ and dispersion factor $\beta(f, z)$ including the higher-order terms' effect on the attenuation and dispersion is investigated. The dispersion factor $\beta(f, z)$ is amended by adding quadratic-order terms to generate new transfer function to recover the space charge waveform under the temperature gradient. For the space charge recovery of a

coaxial cable under the temperature gradient, Fu et al. [52] detected the space charge under the temperature gradient and also investigated the acoustic wave attenuation and dispersion equations of coaxial cable under the temperature gradient. Wang et al. [53] proposed coaxial cable recovery methodology under the temperature gradient. The transfer function was amended by adding the dispersion coefficients' quadratic approximation to generate the solution of the general wave propagation equation. With this new methodology, the cables' coaxial structure, acoustic wave attenuation and dispersion and temperature gradient effect are recovered successfully.

2.6 Influential factors of space charge behaviours within oil and pressboard insulation materials

2.6.1 Temperature gradient

The temperature gradient exists within converter transformers. The mineral oil provides the dual functions as the insulator and cooling materials [5]. The oil ducts are always designed at the bottom of the tank and the oil gradually circulates to the outlets at the top of the tank. The temperature of the oil at the top parts is always higher than the bottom part of transformers [6]. Moreover, the temperature gradient is existing between the different voltage of windings. The temperature of the low voltage winding near the core is higher compared to the high voltage winding. Several reasons lead to this phenomenon. Firstly, the core losses transfer to low voltage winding through heat conduction. Secondly, the low voltage winding has the higher current. More heat is generated in the lower voltage winding due to Joule's Law. Thirdly, the narrow space between the low voltage winding and core lead to the difficulty of extracting the heat by the circulation of oil. As temperature gradient exists between the different voltages of the windings, the intermediate insulation materials experiences a temperature gradient as well.

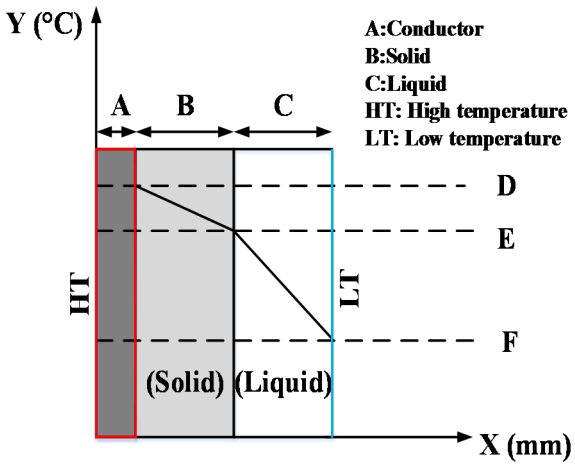

Figure 2-9: The temperature gradient from conductor to liquid.

Figure 2-9 is a schematic diagram indicating the temperature gradient from conductor to liquid. X axis is the distance from the conductor. Y axis is the temperature. A, B and C are the thickness of the conductor, solid and liquid insulation materials. D, E and F are the temperature of the HT part, interface and LT part.

The temperature can severely affect the space charge characteristics. The space charge injection is related to the threshold electric field. Below the threshold, little charge is trapped within the insulation materials (Ohmic behaviour) [54]. It has been found that onset of charge accumulation coincides with the occurrence of the transition from the Ohmic behaviour to space charge limited current (SCLC) conduction [54]. The threshold electric field is highly dependent on the electrode temperature. The higher temperature reduces the threshold and facilitates the space charge injection [54][55]. Typical results shown in Figure 2-10 indicate the threshold of XLPE cable decreases from 8 kV/mm to 3 kV/mm when the temperature increases from 25°C to 70°C.

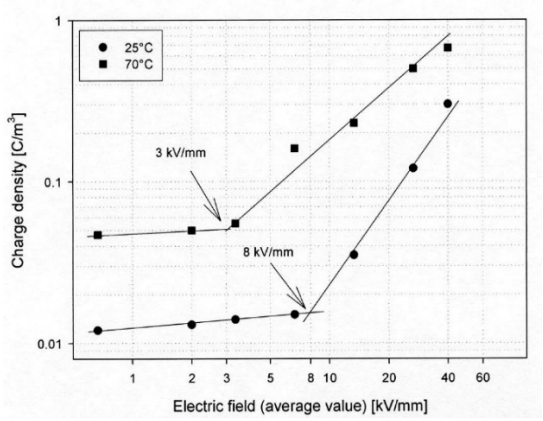

Figure 2-10: Space charge characteristics of XLPE cable at 25°C and 70°C [54].

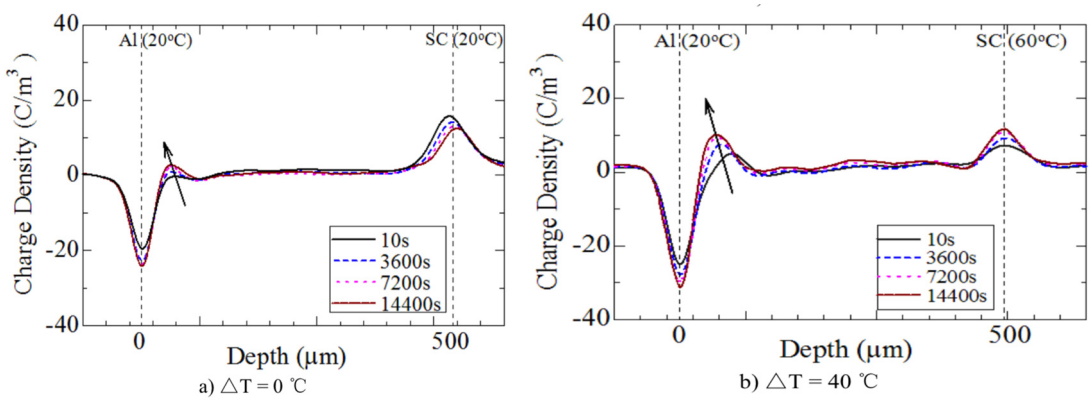

Figure 2-11: The space charge characteristics in LDPE at ambient temperature (ΔT = 0 °C) and temperature gradient (ΔT = 40 °C) [56].

Figure 2-11 (a) shows the space charge characteristics in LDPE at ambient temperature (ΔT = 0 °C) and temperature gradient (ΔT = 40 °C) in Figure 2-11 (b). The larger amount of the heterocharge accumulates near the low temperature Al electrode under the 40 °C temperature

gradient compared to the ambient temperature. The increased temperature of electrode facilitates the charge injection and higher temperature region accelerates charge movement, which accounts for the heterocharge formation.

2.6.2 Voltage reversal

For CSC technology, the valve side winding of the converter transformer will withstand not only AC and DC but also different polarities of applied voltage [2]. During the PR operation, the existing space charge may not dissipate quickly enough and it creates its own electric field superposed with the newly applied electric field after the PR operation. Consequently, the electric field in the oil gap is severely enhanced after the PR operation, which affects the safe and reliable operation of converter transformers [12].

The PR operation has been established as one of the routine tests to verify the insulation properties of the high voltage devices [2]. Based on the current standards [57] [58], it shows that the key factors affecting the electric field after the PR operation are the voltage magnitude, the PR counts, the DC voltage application time and PR duration time. The current standard [59] indicates that 90 minutes of voltage application time is capable to achieve the steady state of the electric field distribution of oil and pressboard insulation. Moreover, the PR operation is defined as a double PR test with both PR operation time taking place within two minutes [57] [58].

The typical PR operation voltage is generally classified into four different stages with the voltage reversing from positive to negative shown in Figure 2-12. (1) DC positive voltage transient state (2) DC positive voltage steady state (3) PR state (4) DC negative voltage steady state.

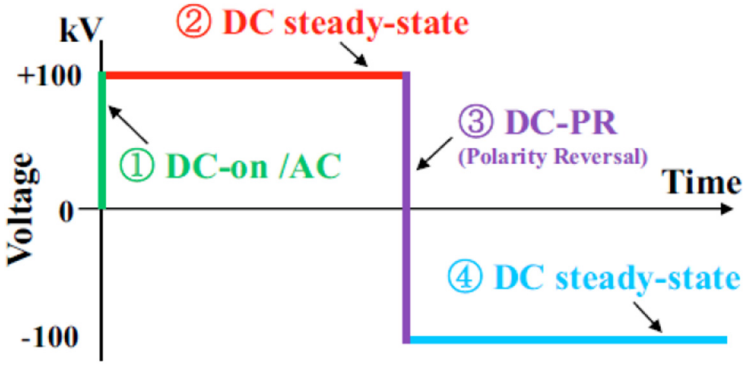

Figure 2-12: PR operation voltage in HVDC system [11].

The electric field after the PR E_{PR} is determined by the field before the voltage reversal E_{bef} and the electric field during the PR ΔE_{AC} shown in the equation (2-21). During the polarity reversal, a dielectric displacement field ΔE_{AC} is superimposed to the initial electric field E_{bef}, with the magnitude of the voltage changing from $\Delta V = +V - (-V) = 2V$. Two factors can determine the

electric field after the polarity reversal: the E_{bef} and time constant τ. The time constant τ can be calculated by the above equation (2-10). The time constant determines the charge dissipation rate and affects the ΔE_{AC}.

$$E_{PR} = E_{bef} + \Delta E_{AC}(\Delta V = 2V) \quad (2\text{-}21)$$

Experiment results show that the time constant τ affects the electric field of the oil and pressboard samples after the PR operation. Qi [2] investigated different PR operation time on the transient electric field of oil using the Kerr effect method under the ambient temperature. It has been found that the impact of the PR operation time on the transient electric field of the oil is based on the ratio between the PR duration (T_r) and time constant τ for the charge accumulation and dissipation [2]. When the T_r is longer or close compared to the time constant τ, the T_r has the significant influence on the transient electric field of oil. Otherwise, the T_r time has less impact on the electric field of oil.

2.6.3 Degradation

When a transformer is energised, its natural operation creates an internal environment subjected to time-varying electromagnetic fields and heat resulted from joule effects generated by the circulating currents in the copper windings and the magnetic core. The internal structure of transformer is subject to the electrical, thermal, chemical and mechanical stresses. Each stress mechanism acts on the oil and pressboard insulation system and gradually alters the structure of the materials, which in turn change the electrical and mechanical properties of the insulation materials [14].

The number of glucose units forming the cellulose polymer chain is called the degree of polymerisation (DP). New cellulose molecules contain around 1200 glucose molecules. Cellulose chains are shortened with the ageing process. The limit of the reliable operation for the DP value varies from150 to 200, at which the cellulose is brittle and fragile [10]. Therefore, the DP has become an effective diagnostic tool to indicate the degradation of the pressboard.

2.6.4 Electrode materials

The PEA system typically has the configuration of the semicon (SC)/ aluminium (Al) electrode. The work function of the Al is (4.08$\pm$ 0.05 eV) and the SC is (3.5eV), which has the lower work function compared to Al [60]. The bulk space charge or the polarity of two same materials interfacial charge density is determined by the voltage polarity of SC materials due to its low work function. This has been verified by one or two layers of space charge results under the SC/Al electrode system[56] [61].

Some preliminary experiments have also been conducted indicating the relationship between the

electrode materials and space charge characteristics. Chen et al. [60] measured the space charge of LDPE under different electrode materials using the PEA method. From the charge injection perspective, both holes and electrons can inject easily from SC compared to Al (SC>Al). From the injection rate perspective, holes > electrons from Al and electrons > holes from SC.

2.6.5 Moisture

Within the transformers, there is a large amount of hydrophilic pressboard and a large volume of hydrophobic oil. The majority of the moisture is always held in the pressboard. It has been accepted that the existence of the moisture content has great influence on the performance of high voltage transformers. The existence of the moisture decreases the dielectric strength of both oil and pressboard and reduces the mechanical strength of the pressboard [14] [62]. This explains why great care has been taken in order to reduce initial moisture content during the construction of transformers. Hence the pressboard must be extremely well dried to a maximum moisture content range from 0.3% to 0.5% [10] and the residual water content within the mineral oil ranges from 0.5 to 5 ppm [10] after the drying process.

The pressboard and oil do not work in isolation but interact as a system. A significant interaction between the oil and pressboard is the exchange of the moisture, which form the moisture equilibrium. Figure 2-13 is the typical moisture equilibrium between the paper and oil shown as Oommen curves [63]. At each temperature, a set of equilibrium curves can be used for the estimation of moisture content in the paper based on the moisture content of the oil, which is easier to acquire. The most significant part is the lower left in Figure 2-13 rectangular section shown in Figure 2-14. The logarithmic scale improves the readability of the data for the practical interest.

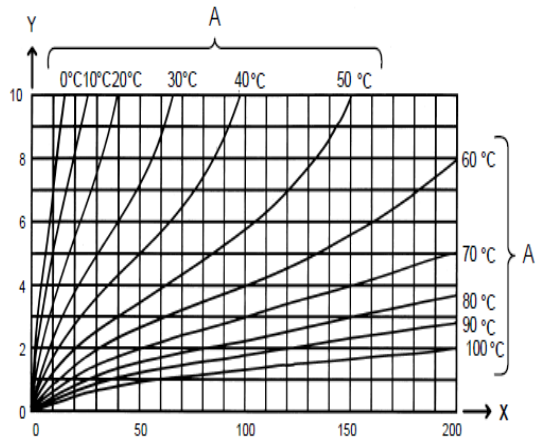

Figure 2-13: Moisture equilibrium curves for paper and oil [63].

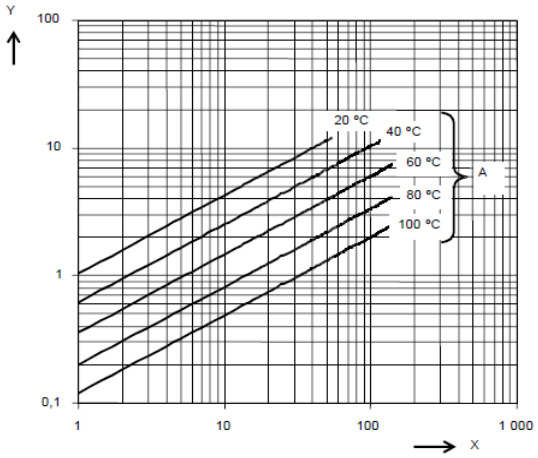

Figure 2-14: Logarithmic moisture equilibrium curves for paper and oil [63].

For both graphs, the X axis represents the water in oil (mg/kg), Y axis is water in paper (%), A is the mean temperature.

Some preliminary efforts have been made to investigate the relationship between the moisture content and the space charge characteristics of oil-impregnated paper. Hao et al. [64] investigated different moisture levels: 0.28%, 1.32%, 4.96% and how they affect the space charge behaviour of the oil-impregnated paper. The moisture content is correlated with mobility of the charge carriers, the higher moisture content leads to the higher conductivity and the mobility, leading to less space charge accumulation in the samples.

2.6.6 Multilayers

In a high voltage insulation system, the combination of different dielectric materials is inevitably used. As a consequence, interfaces are very common in high voltage electric equipment [65]. Typical examples are converter transformers, where the combination of two different dielectric materials contain both oil and pressboard. Under the DC voltage application, the interface is the favourite position for the space charge accumulation. This is due to the broken bonds and some extra chains at the interface, which may be regarded as the deep traps for the space charge accumulation [4] [34] [66] [67].

Currently, the effect of space charge in layered insulation systems has been considered theoretically based on the Maxwell-Wagner theory. It relies on the difference in conductivity and dielectric constant of two different materials. For the electric field of multilayers shown in Figure 2-15, the electric field of multilayers is deduced based on following equations for both transient and steady state.

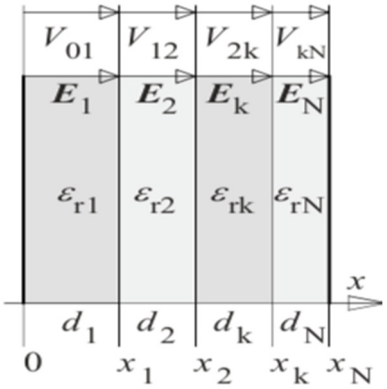

Figure 2-15: Plane multilayers insulation materials arrangement [10].

Because the continuity of the displacement field, in transient dielectric displacement field (at AC voltage)

$$\mathrm{D_k}(x_k) = \mathrm{D_{k+1}}(x_{k+1}) \tag{2-22}$$

$$E_k = \frac{V}{\varepsilon_k \sum_{i=1}^{N} \frac{d_i}{\varepsilon_i}} = \frac{V}{\varepsilon_k (\frac{d_1}{\varepsilon_1} + \frac{d_2}{\varepsilon_2} + \cdots + \frac{d_N}{\varepsilon_N})} \tag{2-23}$$

Because the continuity of the current density, in stationary conduction field (at DC voltage)

$$\mathrm{J_k}(x_k) = \mathrm{J_{k+1}}(x_{k+1}) \tag{2-24}$$

$$E_k = \frac{V}{\gamma_k \sum_{i=1}^{N} \frac{d_i}{\gamma_i}} = \frac{V}{\gamma_i (\frac{d_1}{\gamma_1} + \frac{d_2}{\gamma_2} + \cdots + \frac{d_N}{\gamma_N})} \tag{2-25}$$

It has been found that the Maxwell-Wagner theory only works for linear materials without consideration of charge traps and recombination. In reality, there is a significant deviation from the above as the influence of charge traps and surface states of the materials are not considered in the theory. The surface of the oil-impregnated pressboard contain lots of traps considering broken bonds and chain folds, leading to extra space charge accumulation at the interface [9][34].

Comparisons between the electric field based on space charge and Maxwell-Wagner theory is presented in [68]. It has been found that the polarity of the interfacial charge is consistent with the Maxwell-Wagner theory but the magnitude is not. The electric field caused by the space charge is higher compared to that from Maxwell-Wagner theory [68]. The temperature and electric field effect on the conductivity of the insulation materials is considered and the relative equation is interpolated into the numerical model. The electric field calculated by space charge and Maxwell-Wagner theory are also compared under different temperature and electric fields [68].

There are some difficulties to measure the space charge of multilayers under ambient temperature. Firstly, considering the acoustic wave propagation within the multilayers of samples, reflection may occur due to the mismatch of the impedance of two different materials such as Epoxy oil and Epoxy, which is shown in Figure 2-16. Some researchers have tried to adjust the thickness and arrangement of multilayers samples to delay the reflection signal from the useful space charge signal [69]. Secondly, there is severe attenuation and dispersion of the acoustic wave in the thick oil and pressboard. Anode charge peak is quite small after the acoustic propagation, which leads to the difficulty of calibrating the space charge of multilayers samples.

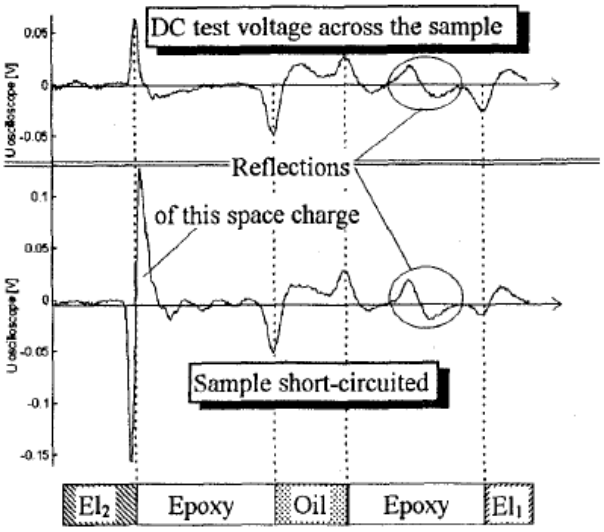

Figure 2-16: Space charge of multilayers of Epoxy oil and Epoxy under ambient temperature.

2.7 Summary

The converter technologies including CSC and VSC have been introduced in the HVDC system. The most important apparatus are HVDC converter transformers. The insulation materials in converter transformers are the combination of the oil , kraft paper and pressboard. Generally, in the oil and PB system, the electric field distribution is related to the conductivity and permittivity of insulation materials based on Maxwell-Wagner theory. The space charge results may defy part of the Maxwell-Wagner theory. The existence of the space charge has been regarded as a major issue to affect the safe and reliable operation of converter transformers. The space charge result should be used to evaluate the electric field of insulation materials. Morden space charge detection techniques including thermal and acoustic method have been reviewed and the widely used pulsed electro-acoustic method (PEA) method has been introduced. The space charge recovery methodology has been briefly discussed. The space charge influential factors such as the temperature, polarity reversal, electrode materials, moisture and multilayers have been discussed.

Current research is focused on investigating the influential factors on the space charge behaviour with the aim to improve the interpretation and understanding of the electrical performance of converter transformers. From the review of influential factors on the space charge behaviour, it has been found that less attention has been focused on temperature gradient effect on the space charge behaviour. The dissertation topic is to explore the temperature gradient effect on the space charge of oil and pressboard and the setup of new space charge equipment are described in the next chapter.

Chapter 3 The design of new PEA system with temperature gradient

3.1 The design of new PEA system with temperature gradient

Pulsed electro-acoustic method (PEA) was firstly introduced in the 1980s [36] and has been developed for around 40 years. The majority of space charge measurements are conducted with ambient temperature. To fulfil the objectives of the present research, a new pulsed electro-acoustic (PEA), which is capable of measuring space charge accumulation with a temperature gradient, needs to be designed, built, and tested.

This chapter contains two parts. Firstly, it introduces the design of the new PEA system, which includes, the upper electrode, bottom electrode and temperature control system. Secondly, the temperature and electric signal measurement of the new PEA system will be presented.

Figure 3-1 shows a schematic diagram of the new PEA system. It includes a HVDC input, pulse generator, temperature control system, upper electrode, bottom electrode, oscilloscope and a computer. DC voltage is applied to the sample through the upper electrode. The interaction of the pulse voltage and charge generates the acoustic wave. The temperature control system is used to control the temperature of both electrodes. The output signal is displaced in the oscilloscope and eventually received by the computer for further processing.

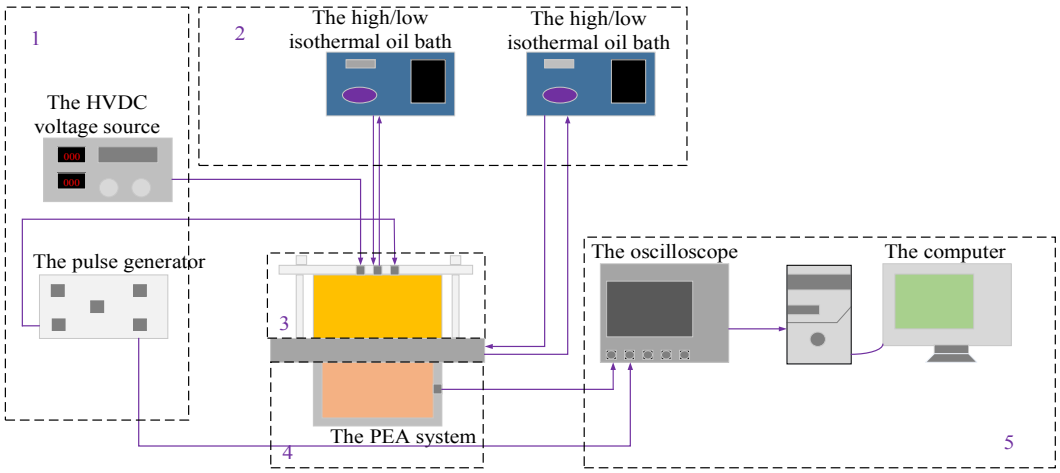

Figure 3-1: A schematic diagram of the new PEA system.

3.1.1 The design of the upper electrode

In the PEA system, DC voltage is applied to the sample through the upper electrode. Under the DC voltage, the surface charges at the ground electrode and at the top electrode are formed. The space charge in the sample, appears once the electric field exceeds the threshold value for charge

injection of the sample [54]. The system was designed to apply a maximum DC voltage of 20 kV with sample thickness varies from 0.3 mm to 1.5 mm.

Since the space charge measurement is based on the average technique, a repeatable pulse voltage generation is required [45]. The pulse width determines the spatial resolution. In general, the pulse width should be close to the travelling time of the pressure wave through the piezo-transducer and thus high sensitivity of the measurement is achieved. The sensitivity of the measurement also depends on the magnitude of the pulse voltage. The higher voltage leads to the higher sensitivity of measurement. Generally, the pulse width varies from 5 ns to 40 ns with the magnitude up to 2 kV [70]. The pulse voltage used in this experiment is 800V, 1 kHz with a pulse width of 10 ns.

The upper electrode of the system is made of brass. The combination of the pulse voltage and DC voltage is applied to the upper electrode. The edge of the electrode was rounded, in order to avoid discharge. Since the electrode should be parallel to the sample, fixed pressure needs to be applied to the sample. A semi-conductive layer is inserted between the sample and electrode to acquire better acoustic impedance matching [36].

To apply a DC voltage to the sample, a resistor R_1 is required. The equivalent circuit of the upper electrode is shown in Figure 3-2. The bias resistor R_1 is connected in series with the DC supply V_1, the sample is represented by the parallel connected resistor R_2 and capacitor C_2. The coupling capacitor is C_1 and the matched resistance is R_3. V_2 is pulse voltage. The capacitance of the sample C_2 (in the order of pF) is small compared to the coupling capacitor C_1 (in the order of nF) and the capacitance of the DC supply (in the order of mF). The pulse voltage V_2 is mainly applied to the coupling capacitor C_1 if there is no resistor R_1 in the circuit. The current from the pulse voltage should mainly flow through the sample, thus the value of the resistor R_1 was selected to be much higher compared to the higher frequency impedance of C_2. For example, for the 0.5 mm aged pressboard with sample capacitance of 5.8423 pF, requires the resistor R_1 to satisfy equation (3-1): where f_p is given by equation (3-2) and ΔT_p is the pulse duration which is 10 ns in this experiment.

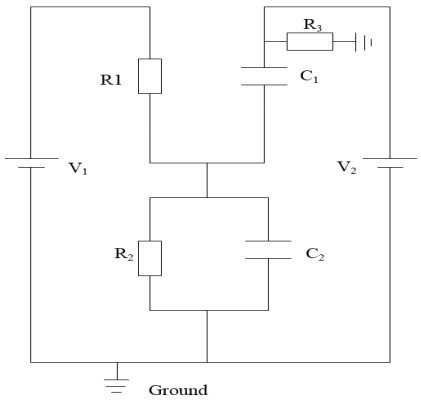

Figure 3-2: The equivalent circuit of the upper electrode.

$$R_1 \gg 1000 \times \frac{1}{2\pi f_p C_2} \tag{3-1}$$

$$f_p = \frac{1}{\Delta T_p} \tag{3-2}$$

The minimum resistor R_1 is calculated to be 0.27 MΩ.

For the steady state analysis, the voltage meets the resistive distribution. As the voltage is mainly applied to the sample, R_2 should be much higher compared to R_1. The following equation should be satisfied.

$$\frac{R_1}{R_1 + R_2} \leq 1\% \tag{3-3}$$

For example, for the resistor of 0.5 mm aged pressboard R_2 with a resistance of 1.9 TΩ, requires the resistor R_1 to satisfy equation (3-3). The maximum resistor R_1 is calculated to be 19 GΩ. Eventually, the value to 30 MΩ of resistor R_1 is selected.

The resistor R_1 is also used as the protective resistor for the power supply. When breakdown occurs, currents flow through the resistor. High current can lead to serious damage to the power supply. Therefore, a high resistor is placed to protect the high voltage power supply. The resistor R_1 is selected with a rating of 16W which is calculated sufficiently to protect the power supply.

A coupling capacitor is necessary to apply a pulse voltage to the sample. If there is no coupling capacitor C_1 in the circuit, the DC voltage is applied to the resistor R_1, and less voltage is applied to R_3 and as it would be in parallel with R_2. When the coupling capacitor C_1 (in the order of nF) is connected in the circuit, the majority of the DC voltage is applied to the sample, because R_2 (1.9 TΩ) is much large compared to resistor R_1 (30 MΩ). In addition, the capacitance of C_1 should be much larger compared to the capacitance of the sample C_2 and the coupling capacitor C_1 is calculated based on the following equation:

$$\frac{C_2}{C_1 + C_2} \leq 1\% \tag{3-4}$$

$$C_1 \geq 99 C_2 \tag{3-5}$$

The capacitance of 0.5 mm aged pressboard C_2 is 5.8423 pF. C_1 is higher than 0.58 nF. Eventually, the value of 1.3 nF is selected for the capacitance of coupling capacitor. Since most of the sample capacitance is about several pF, the capacitance of few nF is adequate for the coupling capacitor.

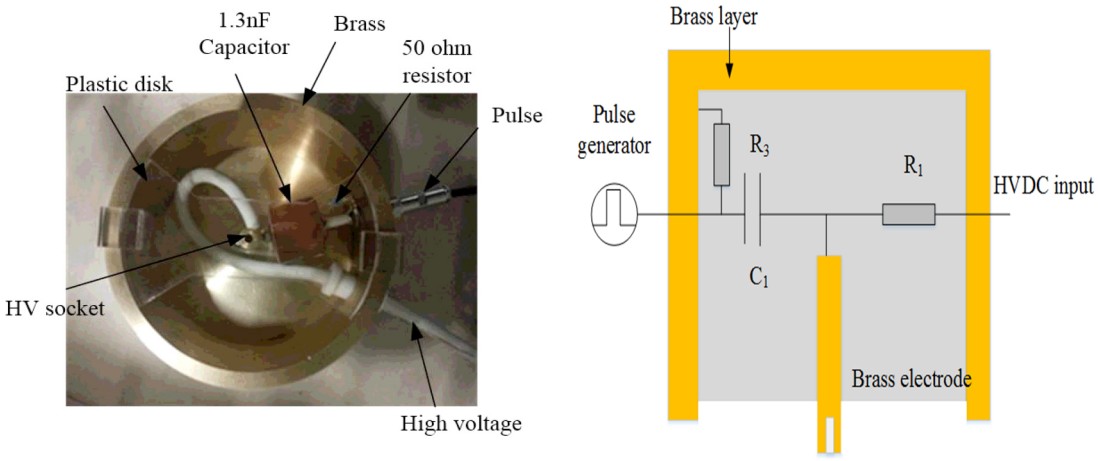

(a) Image of real object (b) A schematic diagram of the upper electrode

Figure 3-3: The upper electrode of new PEA system.

Figure 3-3 (a) shows the image of upper electrode and Figure 3-3 (b) shows the schematic diagram of an upper electrode of the new PEA system. A hole was drilled on the top of the brass electrode, shown in Figure 3-3 (a), for the easy connection to the brass electrode in PTFE container shown in Figure 3-4 (a). Figure 3-4 (a) is the image of the brass electrode within the PTFE container. A plastic connector is assembled on the surface of the PTFE part served as the oil inlet. The circulation of the oil increase the temperature of the brass electrode. Figure 3-4 (b) shows the schematic diagram of the brass electrode in the PTFE container. The banana plug attached to the brass electrode is directly inserted into the upper electrode shown in Figure 3-3 (a) to achieve the firm electric connection between two brass electrodes. Two O-rings are inserted in the PTFE part to prevent any oil leakage.

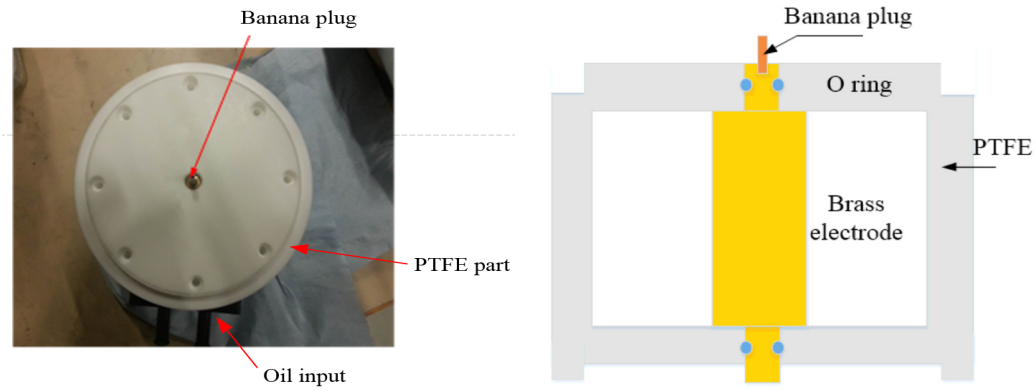

(a) Image of real object (b) Schematic diagram of the upper electrode in PTFE container

Figure 3-4: The upper electrode in PTFE container of the new PEA system.

Epoxy resins are excellent electrical insulator. Thus the epoxy has been poured into the upper electrode shown in Figure 3-3 (a) as the excellent electrical insulator. The flow chart in Figure 3-5 illustrates the preparation process of the epoxy resin. The process includes firstly, preheating the resin at 50 °C for around 30 minutes to reduce its viscosity. The next step is to weight out the required mass of the epoxy resin DER-332 and the curing agent D-230. A stoichiometric resin: hardener ratio of 1000:344 was used according to the supplier recommendation. Then, a magnetic stirrer is used to mix the mixture. After that, the mixture is degassed for about 50 min in vacuum oven to ensure no bubbles trapped in the mixture. Finally, after degassing, the mixture of liquid was slowly poured into the upper electrode. To avoid the heat generation during the curing, which may affect the electric components within the upper electrode such as the coupling capacitor and matched resistance, the curing process lasts around 3 days under the ambient temperature to avoid unnecessary heat generation. Due to the fact that epoxy resins shrink after curing, [71], extra epoxy resin mixture was added to compensate for reduced size of epoxy.

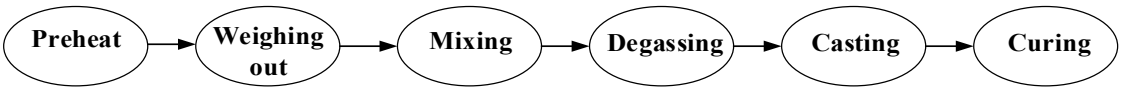

Figure 3-5: Flow chart of preparation of epoxy resin and hardener.

3.1.2 The design of the bottom electrode

The thickness of the bottom electrode should be in harmony with the thickness of the sample considering the acoustic reflection in the bottom electrode. Figure 3-6 indicates the acoustic wave propagation in the bottom electrode. Y-axis represents the thickness Where d_{sa} and d_{Al} are the thickness of sample and aluminium electrode, respectively. X-axis is the width of the sample. When a pulse is applied, the pulse perturbs the internal charge and generates the acoustic wave. The acoustic wave propagates in bi-direction. The acoustic wave propagates in the Y direction is ignored as the delayed time compared to the original acoustic wave. For the design of the aluminium electrode, equation (3-6) needs to be satisfied to avoid the superposition of the original and reflected acoustic waves.

$$\frac{3d_{\mathrm{Al}}}{u_{\mathrm{Al}}} > \frac{d_{\mathrm{Al}}}{u_{\mathrm{Al}}} + \frac{d_{\mathrm{sa}}}{u_{\mathrm{sa}}} \tag{3-6}$$

Where $u_{\mathrm{Al}} = 6000\ m/s$ and $u_{\mathrm{sa}} = 2000\ m/s$ are the acoustic wave velocity in Al and sample respectively. If the maximum thickness of the sample d_{sa} is 6 mm, then:

$$d_{\mathrm{Al}} > 9\mathrm{mm} \tag{3-7}$$

The thickness of the aluminium electrode is selected to be 10 mm to avoid the acoustic wave reflection within the aluminium electrode.

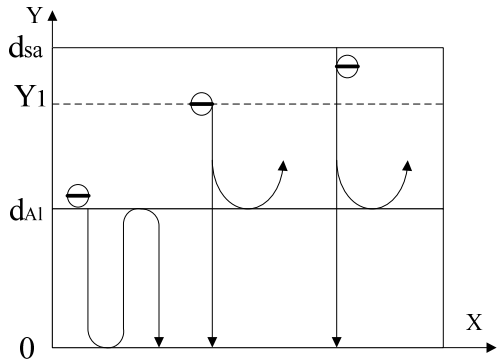

Figure 3-6: Acoustic wave transmission within the bottom electrode.

The Piezo-electric transducer is an acoustic sensor which is commonly used to detect acoustic waves and convert waves to an electric signal in the PEA method. The thickness of piezo-transducer and acoustic velocity in the sample are important in terms of determining the spatial resolution of the PEA system. The thickness of the piezo-transducer should satisfy the following equation:

$$b < \Delta T_{\mathrm{p}} u_{\mathrm{b}} \tag{3-8}$$

Where b is the thickness of the piezo-transducer sensor, ΔT_{p} (10 ns) is the width of the pulse voltage, and u_{b} (2250 m/s) is the acoustic velocity in the P(VDF-TrFE) sensor [72]. Based on equation (3-8), the thickness of the piezo-transducer should be less than 22.5 μm. However, considering the severe attenuation of the acoustic wave after its propagation in the pressboard and oil [8], 40 μm thickness of sensor is selected despite loss some spatial resolutions of space charge results. The increase in the thickness of the sensor result in increased sensitivity of the space charge measurement [73].

Furthermore, the capacitance of piezoelectric transducer and resistance of the amplifier form a high pass filter circuit. Due to the limitation of the frequency response of the filter, the PEA output signal always presents overshoot peak. To eliminate overshoot peak, some researchers [45][74] suggest to decrease the cutoff frequency via the increased capacitance of the transducer and the resistance of the amplifier. The capacitance of the transducer increases via the decrease of the thickness of sensor and increase of the surface area. Moreover, considering the current manufacture technology, it is difficult to eliminate the overshoot peak from the hardware perspective, thus a mathematic deconvolution is used to eliminate the overshoot peak and

transform the electric signal to space charge results.

The absorber uses polyvinylidene fluoride (PVDF) materials and has the same acoustic impedance compared to the piezo-transducer. The acoustic wave propagates directly from the piezoelectric transducer to the absorber without reflection at the interface. The acoustic wave transport in the sensor and absorber shown in Figure 3-7. The thickness of the absorber should meet the following equation:

$$\frac{2d_{\mathrm{ab}}}{u_{\mathrm{ab}}} > \frac{d_{\mathrm{Al}}}{u_{\mathrm{Al}}} + \frac{d_{\mathrm{sa}}}{u_{\mathrm{sa}}} \tag{3-9}$$

where u_{ab} =2250 m/s is acoustic velocity of the absorber.

$$d_{\mathrm{ab}} > 5.25\ mm \tag{3-10}$$

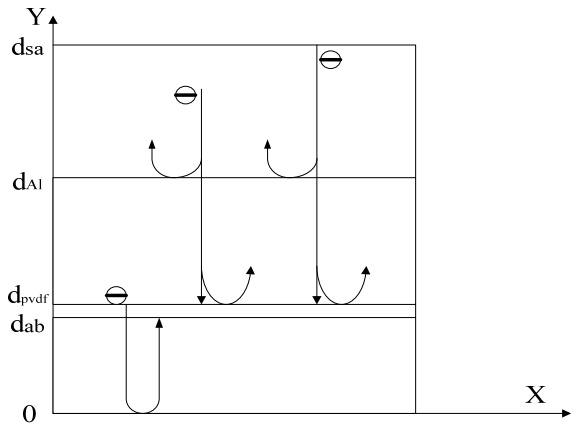

Figure 3-7: Acoustic wave transmission including the sensor and absorber.

thus a thickness of 10 mm absorber was selected.

The electric signal detected from the piezo-transducer is very small, the amplifier is used for signal amplification. AU-1332 is used with gain (48dB) and frequency ranges from (1kHz to 500 MHz).

A schematic diagram of the aluminium bottom electrode is shown in Figure 3-8. With circulation of the oil from the external oil bath, the temperature of the bottom electrode can be controlled.

There are two shield boxes including the brass inner shield and brass outer shield. Since the application of the pulse voltage to the sample can generate high frequency noise and there is some noise from the background, a brass shield is utilized to reduce the noise level.

A fan is used to cool down the temperature of the amplifier as the maximum operating temperature of the amplifier is 70 °C.

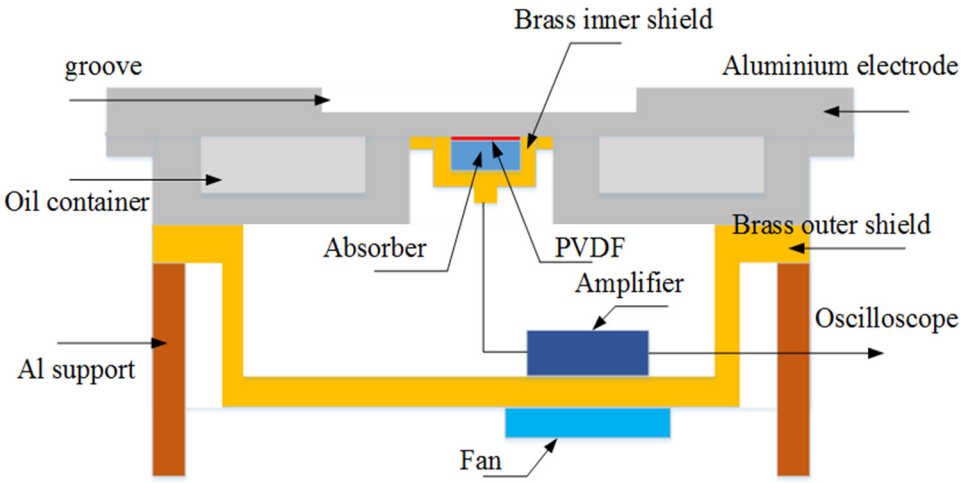

Figure 3-8: A schematic diagram of the bottom electrode.

The spatial resolution of the PEA system [43] is determined by the following equation based on the assumption that the pulse voltage duration ΔT_{p} equals to the pressure wave travelling through the piezo-electric transducer with time duration of ΔT_{s}:

$$\Delta l = u_{\mathrm{sa}} \times \Delta T_{\mathrm{p}} \tag{3-11}$$

Where Δl is the spatial resolution, $u_{\mathrm{sa}} = 2000\, m/s$ is the acoustic velocity of sample and ΔT_{p}=10 ns is the width of the pulse, the calculated spatial resolution is around 20 μm. However, considering the 40 μm thickness of sensor is selected previously, it leads to the case of $\Delta T_{\mathrm{s}} > \Delta T_{\mathrm{p}}$, and spatial resolution of the PEA system is determined by the following equation that [45]:

$$\Delta T_{\mathrm{s}} = d_{\mathrm{b}}/u_{\mathrm{b}} \tag{3-12}$$

$$\Delta l' = u_{\mathrm{sa}} \times \Delta T_{\mathrm{s}} \tag{3-13}$$

where d_{b}=40 μm is the thickness of sensor, $\Delta l'$ is the real spatial resolution. The real calculated spatial resolution is around 36 μm.

3.1.3 Assembly of the new PEA system

The top electrode is a cylindrically shape column designed with a diameter of 10 mm. The edge of the electrode is rounded to prevent discharge due to the electric field enhancement at the sharp edge. The top electrode is connected to the resistor (30 MΩ) and the coupling capacitor (1.3 nF). A DC voltage is applied to the resistor and the coupling capacitor which is connected to the pulse voltage via a matched resistance (50Ω). Epoxy resin is filled in the top electrode to serve as an insulating material and also to fix the electronic components in place.

Figure 3-9 shows the schematic diagram of the PEA sensor. The sensor is cut into a circle with

diameter of 10 mm and thickness of 40 μm. Prior to placing the sensor or the absorber on the bottom Al electrode, both surfaces of the sensor and the absorber were wetted with silicone oil to remove any possible air bubbles trapped at the interface.

To reduce the acoustic reflection, the same acoustic impedance polyvinylidene fluoride (PVDF) rod was attached on the PVDF sensor. The rob was cut into a column with the diameter of 10 mm and thickness of 10 mm. The PVDF absorber serves as a backing material to ensure the continuity of the acoustic transportation without acoustic reflection at the interface between the PVDF absorber and sensor. The gold was sputtered on the surface of the PVDF column to transfer the electric signal generated from the sensor. The edge of the PVDF column was rounded to prevent the short circuit. After securing the inner brass shield using screws, the output signal from the SMA socket was checked to prevent the short circuit.

The output signal is connected to the amplifier through a coaxial cable. The length of the coaxial cable was selected to be as short as possible as the output electric signal is small before the amplification. The output amplified signal from the amplifier is connected to the SMA female to SMA female connector installed on the surface of the brass outer shield. Then the amplified signal is connected to the oscilloscope. The purpose of using a coaxial cable is that it is well shielded to reduce the electromagnetic noise arising from the energising system.

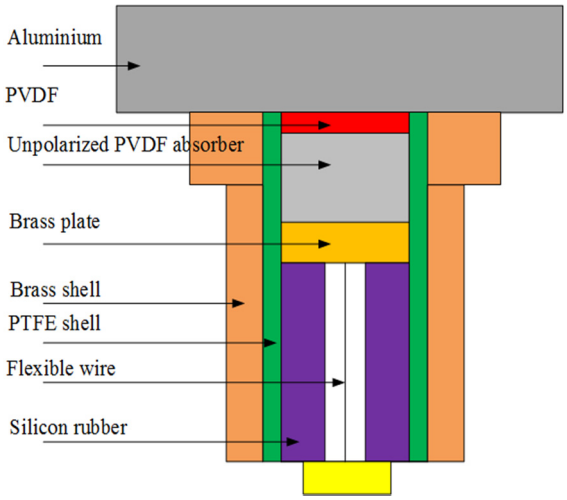

Figure 3-9: A schematic diagram of the PEA sensor.

3.2 The performance of the new PEA system under the temperature gradient

3.2.1 Temperature gradient measurement

The temperature control system needs to be calibrated. To measure the temperature of the upper and bottom electrode, two T type (±1°C) thermal couples were inserted between the electrode

and sample to measure the actual temperature across the sample.

Two oil baths TXF200-ST5 were used to control the temperature of the two electrodes by circulation of the silicone oil. The temperature of the upper electrode ranges from 30 °C to 70 °C while the temperature of the bottom electrode is maintained at 24 °C by a chiller. Figure 3-10 illustrates the temperature gradient across the sample. The actual temperature setting of the oil bath is higher for the upper electrode compared to the displayed temperature due to thermal losses. The calibration for temperature between the oil bath and upper electrode is shown in Figure 3-11.

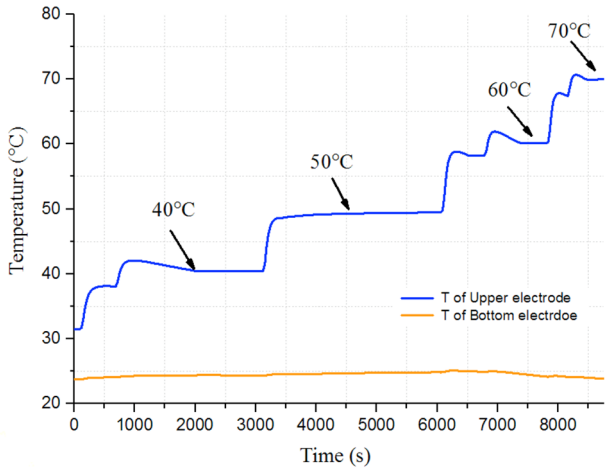

Figure 3-10: Compression between the temperature of the upper and bottom electrode.

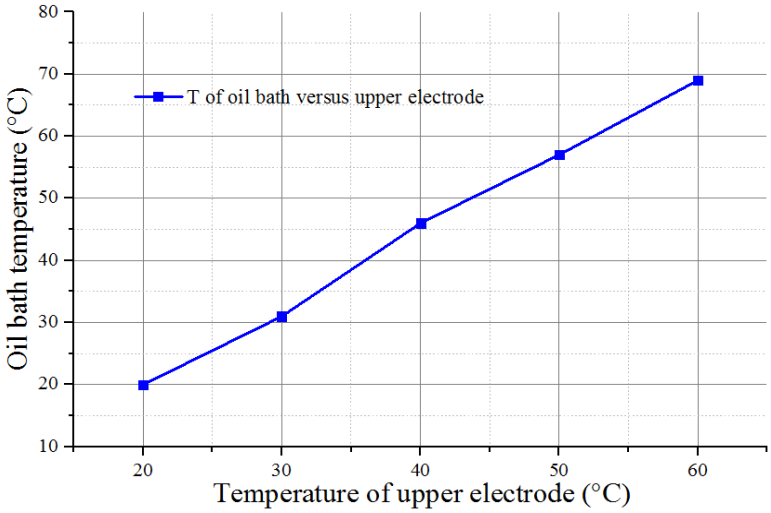

Figure 3-11: Calibration for the temperature between the oil bath and upper electrode.

3.2.2 Space charge measurements

Figure 3-12 (a) shows space charge result of 0.5 mm PMMA under 1 kV. The capacitance of piezoelectric transducer and resistance of the amplifier forms a high pass filter circuit. The data

obtained from the oscilloscope generally includes some distortion due to the nature of the detection circuit [45]. In order to remove the overshoot peak from the output signal, a mathematic deconvolution method is used to transform the electric signal to the space charge. After the calibration, the space charge results are shown in Figure 3-12 (b).

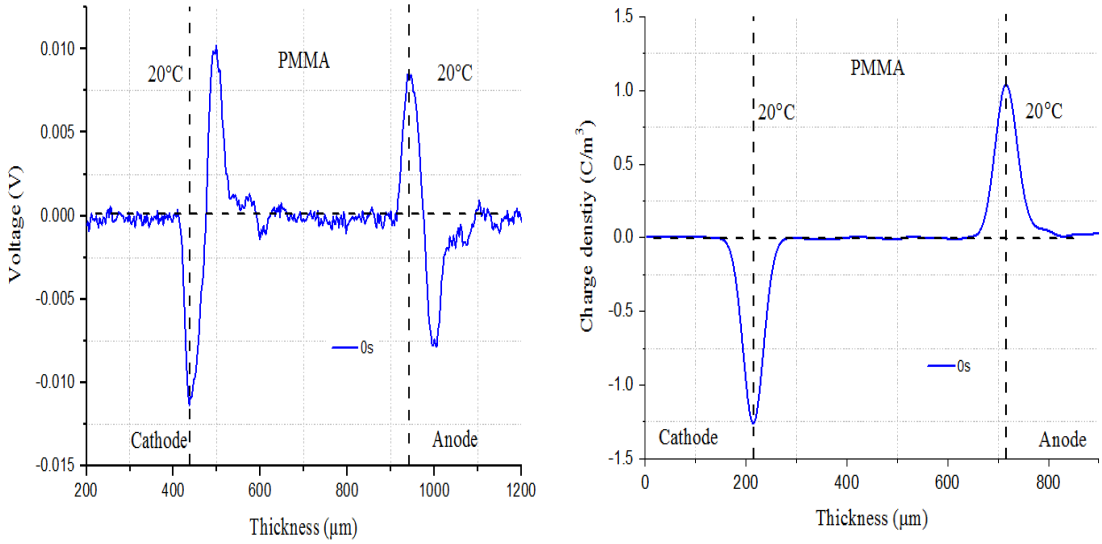

(a) Before calibration (b) After calibration

Figure 3-12: Space charge results of 0.5 mm PMMA under 1 kV.

3.3.3 Summary of technical parameters of the new PEA system

Figure 3-13 illustrates the schematic diagram of the purpose-built PEA system. Table 3-1 below summaries the technical parameters of the new PEA system. The test shows that the designed PEA system meets the requirements and is capable of measuring the space charge under a temperature gradient.

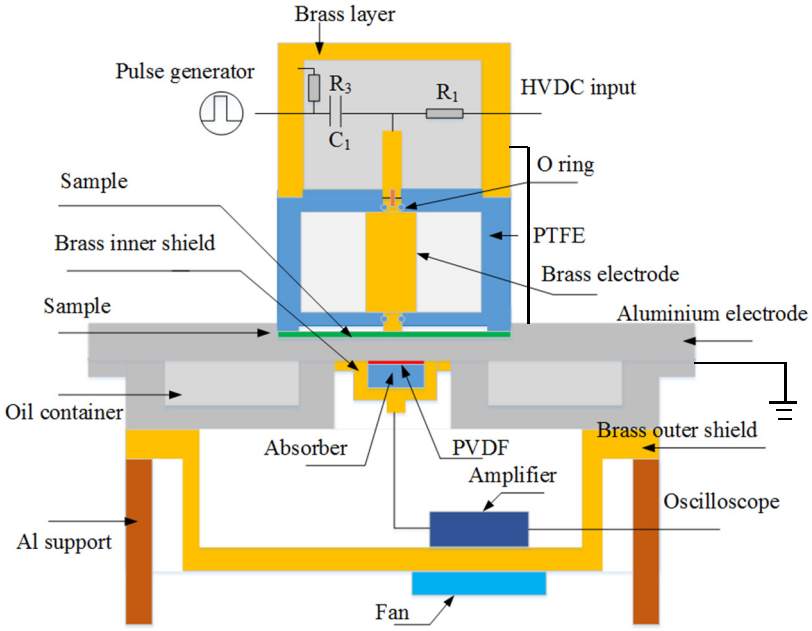

Figure 3-13: Configuration of the PEA system.

Table 3-1: Parameters of the manufactured temperature PEA system

Electrical components of PEA	Parameters
HV electrode diameter in mm	10
Maximum voltage in kV	20
Maximum pulse voltage	800 V
Pulse width in ns	10 ns
Sensor P(VDF-TrFE)	40 µm
Spatial resolution	36 µm
Amplifier	48 dB
Maximum Upper electrode Temperature	70 ℃
Maximum Bottom electrode Temperature	60 ℃
Minimum sample thickness	180 µm
Maximum sample thickness	1.5mm

3.3 Summary

This Chapter mainly discusses the requirements, main components, design, build and test of the new PEA system. The new PEA system meets the requirement and is capable of measuring the space charge under a temperature gradient. The performance of the temperature and space charge behaviours for the new PEA system are presented. The technical parameters of new PEA system are summarized.

Chapter 4 Space charge waveform recovery under a temperature gradient

4.1 The principles of the PEA measurement method

Under a DC voltage, positive and negative charges are induced at the interfaces between the sample and the electrodes. When an electric pulse is applied, an acoustic pressure wave is generated from each charge. This pressure wave is detected by the piezoelectric transducer and converted into an electrical signal. Using a mathematical deconvolution method, a space charge distribution can be calculated. The theoretical equations representing the process of acoustic wave propagation and recovery of the space charge distribution under a temperature gradient will be described in this chapter.

4.1.1 Generation of the acoustic wave

When a DC voltage is applied, an amount of surface charge, σ_{dc}^{+} (C/m^2), is generated at the interface between the sample and the electrodes. The surface charge density is described by following equation:

$$\sigma_{\mathrm{dc}}^{+} = \varepsilon E_{\mathrm{dc}} \tag{4-1}$$

where ε is the dielectric permittivity (F/m), and E_{dc} (V/m) is the constant electric field. The dielectric permittivity is described by the following equation:

$$\varepsilon = \varepsilon_0 \varepsilon_{\mathrm{r}} \tag{4-2}$$

where $\varepsilon_0 = 8.854 \times 10^{12}$ (F/m) is the permittivity in a vacuum and ε_{r} is called the relative permittivity.

When a pulsed voltage, $V_{\mathrm{p}}(t)$, is applied, a pulsed electric field, $e_{\mathrm{p}}(t)$, is established and can be calculated using the following equation:

$$e_{\mathrm{p}}(t) = V_{\mathrm{p}}(t)/d \tag{4-3}$$

where d is the sample thickness. When dealing with volumes, space charge, $\rho(x)$ (C/m^3), exists in the bulk of the sample and induces charges at both the anode and the cathode, σ_{ρ}^{+} and σ_{ρ}^{-}, respectively, the magnitudes of which depend on the distance between the space charge position and the electrode [33][36][75] and can be calculated based on following equations:

$$\sigma_{\rho}^{+} = -\int_0^d \frac{x}{d}\rho(x)dx \tag{4-4}$$

$$\sigma_{\rho}^{-} = -\int_{0}^{d} \frac{d-x}{d}\rho(x)dx \tag{4-5}$$

Thus, the total surface charge, σ^{+} and σ^{-}, under the positive voltage can be calculated by the following equations:

$$\sigma^{+} = \sigma_{\mathrm{dc}}^{+} + \sigma_{\mathrm{pulse}}^{+} + \sigma_{\rho}^{+} = \varepsilon E_{\mathrm{dc}} + \varepsilon e_{\mathrm{p}}(t) - \int_{0}^{d} \frac{x}{d}\rho(x)dx \tag{4-6}$$

$$\sigma^{-} = \sigma_{\mathrm{dc}}^{-} + \sigma_{\mathrm{pulse}}^{-} + \sigma_{\rho}^{-} = -\varepsilon E_{\mathrm{dc}} - \varepsilon e_{\mathrm{p}}(t) + \int_{0}^{d} \frac{d-x}{d}\rho(x)dx \tag{4-7}$$

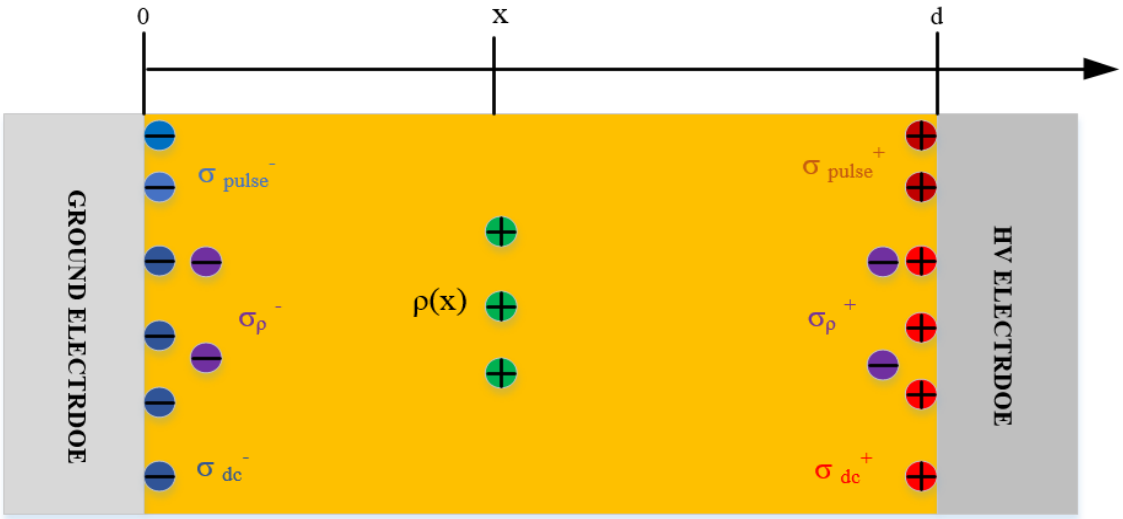

Figure 4-1: The distribution of surface charge under a positive voltage.

where σ^{+} and σ^{-} are the total surface charge densities at the anode (position x=0) and cathode (position x=d) interfaces, respectively, as shown in Figure 4-1. When a pulsed voltage superposed on a DC voltage is applied to the sample, an acoustic wave, $P(t)$ (Pa=N/m^2), is generated from the surface charges, σ^{+} and σ^{-}, and the space charge, $\rho(x)$.This space charge has the width of Δx that exists in the bulk of the sample.

$$P(t) = P_0(t) + P_{\rho}(t) + P_{\mathrm{d}}(t) = \sigma^{-}e_{\mathrm{p}}(t) + \rho(x)\Delta x e_{\mathrm{p}}(t) + \sigma^{+}e_{\mathrm{p}}(t) \tag{4-8}$$

4.1.2 Propagation of the acoustic wave

The propagation of the pressure wave through different materials depends on their acoustic impedance. Acoustic impedance, Z (N s/m^3), is described as:

$$Z = \rho u \tag{4-9}$$

where ρ (kg/m^3) is the material density, and u (m/s) is the acoustic velocity of the material.

When an acoustic wave propagates through different materials, it is partially transmitted and partially reflected. These phenomena are described by the acoustic generation coefficient, $G_{\mathrm{i-j}}$, the transmission coefficient, $T_{\mathrm{i-j}}$, and the reflection coefficient, $R_{\mathrm{i-j}}$, which can be calculated as follows [10]:

$$G_{\mathrm{i-j}} = \frac{Z_{\mathrm{j}}}{Z_{\mathrm{i}} + Z_{\mathrm{j}}} \tag{4-10}$$

$$T_{\mathrm{i-j}} = \frac{2Z_{\mathrm{j}}}{Z_{\mathrm{i}} + Z_{\mathrm{j}}} \tag{4-11}$$

$$R_{\mathrm{i-j}} = \frac{Z_{\mathrm{j}} - Z_{\mathrm{i}}}{Z_{\mathrm{i}} + Z_{\mathrm{j}}} \tag{4-12}$$

The subscript i indicates the material that the acoustic wave comes from, and the subscript j is the material that the acoustic wave propagates to.

Figure 4-2 shows acoustic wave propagation in the PEA system. The pressure propagates towards a piezo transducer attached to the bottom of an aluminium electrode. For example, if the pressure wave, $P_0(t)$ (N/m^2), is generated at the interface between the sample and the ground electrode, the pressure wave, $P_1(t)$, that is propagating towards the ground electrode can be described as:

$$P_1(t) = \frac{Z_{\mathrm{Al}}}{Z_{\mathrm{Al}} + Z_{\mathrm{sa}}} P_0(t) = \frac{Z_{\mathrm{Al}}}{Z_{\mathrm{Al}} + Z_{\mathrm{sa}}} \sigma^{-} e_{\mathrm{p}}(t) \tag{4-13}$$

where Z_{Al} and Z_{sa} are the acoustic impedances of aluminium and the sample material, respectively.

When $P_2(t)$ is generated from the space charge in the bulk of the sample, it can be described as:

$$P_2(t) = \frac{1}{2} \frac{2Z_{\mathrm{Al}}}{Z_{\mathrm{Al}} + Z_{\mathrm{sa}}} \rho(x) \Delta x e_{\mathrm{p}} \left(t - \frac{x}{u_{\mathrm{sa}}} \right) \tag{4-14}$$

Acoustic waves propagate bidirectionally after their generation, so half of the wave travels towards the ground electrode. When such a wave propagates through the interface between different materials, part of it is transmitted and part of it is reflected. Therefore, it is important to consider its transmittance factor. u_{sa} is the acoustic velocity of the sample and x is the position of the space charge density.

$P_3(t)$ can be described as the acoustic wave generated at the interface between the sample and the upper electrode:

$$P_3(t) = \frac{Z_{sa}}{Z_{ba} + Z_{sa}} \frac{2Z_{Al}}{Z_{Al} + Z_{sa}} \sigma^+ e_p(t - \frac{d}{u_{sa}}) \quad (4\text{-}15)$$

where Z_{ba} is the acoustic impedance of the backing material.

Taking into account the delay, the transmittance, the generation coefficients, and the observed pressure,$P(t)$, at the piezoelectric transducer can be determined as:

$$P(t) = P_1(t) + P_2(t) + P_3(t) \quad (4\text{-}16)$$

$$P(t) = \frac{Z_{Al}}{Z_{Al} + Z_{sa}} \sigma^- e_p(t) + \frac{1}{2} \frac{2Z_{Al}}{Z_{Al} + Z_{sa}} \rho(x) \Delta x e_p\left(t - \frac{x}{u_{sa}}\right) + \frac{Z_{sa}}{Z_{ba} + Z_{sa}} \frac{2Z_{Al}}{Z_{Al} + Z_{sa}} \sigma^+ e_p(t) \left(t - \frac{d}{u_{sa}}\right). \quad (4\text{-}17)$$

where Z_{ba} is the acoustic impedance of the semi-conductive material attached to the HV electrode. The semi-conductive material selected generally has an acoustic impedance that is close to that of the sample and it will be now be assumed that $Z_{ba} = Z_{sa}$.

Equation (4-18) can be deduced from Equation (4-17). In Equation (4-17), the second item is generated from a single layer of charge distribution, while in Equation (4-18), the second item is generated from the total charge distribution, using the integral form, as follows:

$$P(t) = \frac{Z_{Al}}{Z_{Al} + Z_{sa}} [\sigma^- e_p(t) + u_{sa} \int_{-\infty}^{+\infty} \rho(u_{sa}\, \tau) e_p(t - \tau)\, d\tau + \sigma^+ e_p(t - \frac{d}{u_{sa}})] \quad (4\text{-}18)$$

where τ is the time constant, defined as $x = u_{sa}\, \tau$.

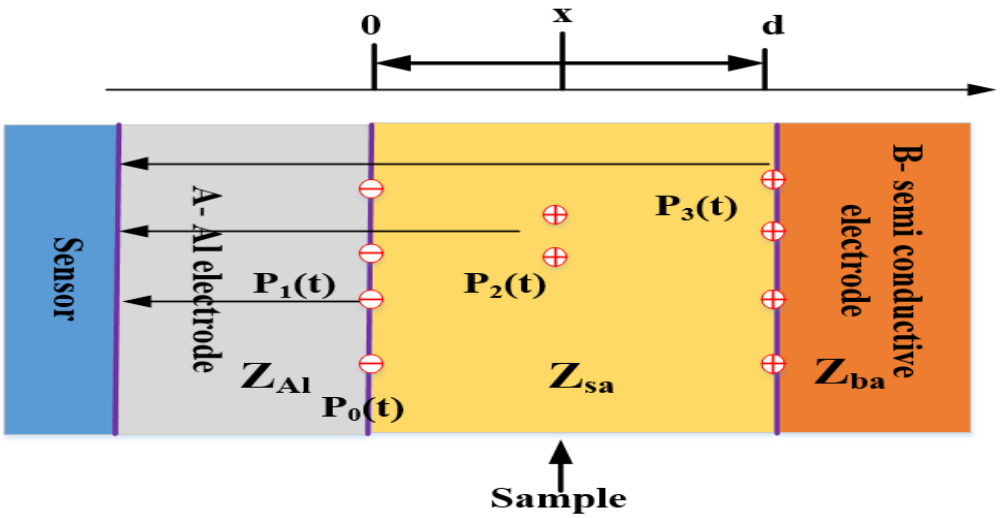

Figure 4-2: Acoustic propogation in a one-layer sample.

4.1.3 Transformation of the acoustic wave to an electric signal

When the acoustic wave, $P(t)$, propagates through the aluminium and applies to a piezo electric transducer, an amount of charge, $Q(t)$, is induced on both surfaces of the transducer, which can be expressed by the following equation:

$$Q(t) = \frac{2Z_{\mathrm{p}}}{Z_{\mathrm{Al}} + Z_{\mathrm{p}}} d_{33} P(t) S \tag{4-19}$$

where d_{33} (C/N) describes the piezoelectric constant, S (m^2) is the surface area of the piezoelectric transducer and Z_{p} is its acoustic impedance. The voltage across the piezoelectric transducer can be calculated by:

$$V_{\mathrm{PVDF}}(t) = \frac{Q(t)}{C_{\mathrm{p}}} \tag{4-20}$$

where C_{p} (F) is the capacitance of the piezo electric transducer, whose value is equal to $\frac{\varepsilon_{\mathrm{p}}}{d_{\mathrm{p}}} S$, and d_{p} and ε_{p} are the thickness and dielectric constant of the piezoelectric transducer, respectively. Equation (4-19) can be inserted into Equation (4-20), to give the following:

$$V_{\mathrm{PVDF}}(t) = \frac{2Z_{\mathrm{p}}}{Z_{\mathrm{Al}} + Z_{\mathrm{p}}} \frac{d_{33} d_{\mathrm{p}}}{\varepsilon_{\mathrm{p}}} P(t) \tag{4-21}$$

If we setting that $g_{33} = \frac{d_{33}}{\varepsilon_{\mathrm{p}}}$ (Vm/N), it can be deduced that:

$$V_{\mathrm{PVDF}}(t) = \frac{2Z_{\mathrm{p}}}{Z_{\mathrm{Al}} + Z_{\mathrm{p}}} g_{33} d_{\mathrm{p}} P(t) \tag{4-22}$$

According to Equation (4-22), the induced voltage, $V_{\mathrm{PVDF}}(t)$, is dependent on the thickness of the piezoelectric transducer. The $V_{\mathrm{PVDF}}(t)$ is always very small, and an amplifier is used to amplify the output voltage, $V_{\mathrm{s}}(t)$.

4.1.4 Deconvolution

As described in Chapter 2, a mathematical deconvolution is used to transform the electric signal into space charge density. The obtained voltage signal, $V_{\mathrm{s}}(t)$, uses the deconvolution method to calculate the distribution of the space charge, $\rho(t)$. The voltage, $V_{\mathrm{s}}(t)$, is described as the convolution of the impulse response of the system, $g(t)$, and the space charge distribution, $\rho(t)$:

$$V_{\mathrm{s}}(t) = g(t) * \rho(t) = \int_{-\infty}^{+\infty} h(t-\tau)\rho(\tau) d\tau \tag{4-23}$$

In order to acquire the impulse response, $g(t)$, the space charge is calculated based on the

deconvolution method. Using fast Fourier transforms (FFT), Equation (4-23) can be re-written as follows:

$$V_s(f) = \rho(f)G(f) \tag{4-24}$$

where $V_s(f)$, $\rho(f)$, and $G(f)$ are Fourier transforms of $V_s(t)$, $\rho(t)$, and $g(t)$ respectively. $G(f)$ is the transfer function and needs to be acquired. The PEA system is assumed to be a linear, time-invariant (LTI) system [76], thus the transfer function, $G(f)$, under high and low voltage should be the same. However, if a space charge exists in a bulk sample, the induced charge on the electrode alters. Therefore, it is important to obtain the transfer function under a low DC stress without the presence of space charge in the sample. The reference signal should consist of the same two peaks; however, the acoustic wave generated at the electrode far away from the piezoelectric transducer is sometimes distorted due to acoustic attenuation and dispersion, therefore the signal derived from the bottom electrode is used for calibration.

The reference voltage signal from the induced charge, $V_r(f)$, under low voltage in the frequency domain can be expressed as:

$$V_r(f) = \rho_r(f)G(f) \tag{4-25}$$

where $\rho_r(f)$ is a Fourier transform of the impulse response of induced charge density under a low voltage in the frequency domain.

With a combination of the transfer function from Equation (4-24) and Equation (4-25), the space charge density in the frequency domain can be expressed as:

$$\rho(f) = \rho_r(f)\frac{V_s(f)}{V_r(f)} \tag{4-26}$$

After an inverse Fourier transformation of Equation (4-26), the space charge, $\rho(t)$, is acquired. The calculation flow of the deconvolution method can be summarized in Figure 4-3.

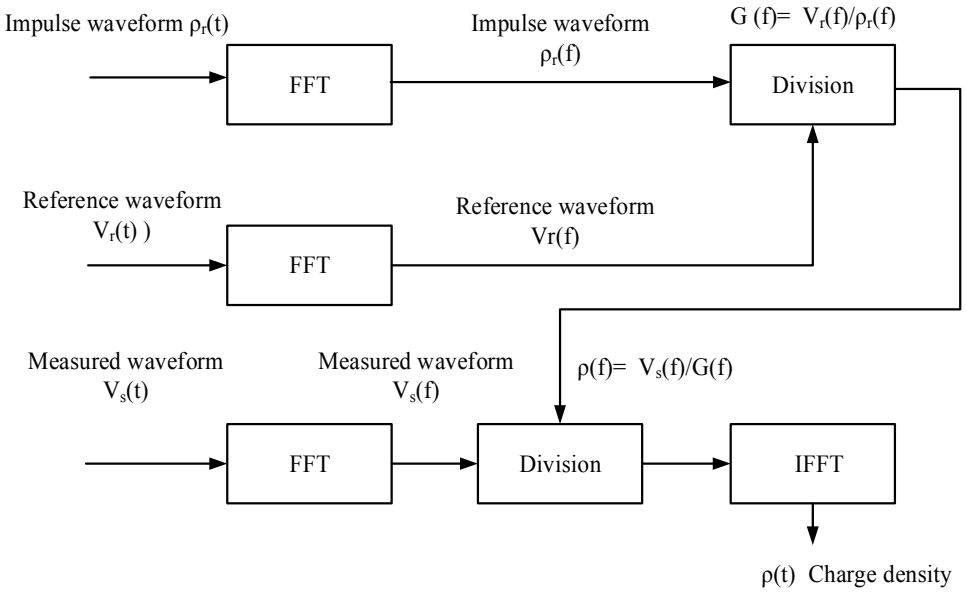

Figure 4-3: A schematic diagram of deconvolution method.

4.1.5 Attenuation and dispersion of the acoustic wave

An acoustic wave in a dispersive medium can be expressed as:

$$P(f,\mathrm{x}) = P(f,0)\exp(-\alpha(f)\mathrm{x})\exp(-\mathrm{j}\beta(f)\mathrm{x}) \tag{4-27}$$

where $P(f,0)$ is the magnitude of the acoustic wave at the position $\mathrm{x} = 0$, and $a(f)$ and $\beta(f)$ are the attenuation and dispersion factors, respectively [46][47]. The procedures to acquire $a(f)$ and $\beta(f)$ are described as below.

The frequency spectra of the acoustic wave at positions x=0 and x=d can be expressed as:

$$P(f,0) = |P(f,0)|e^{-j\phi(f,0)} \tag{4-28}$$

$$P(f,\mathrm{d}) = |P(f,d)|e^{-j\phi(f,d)} \tag{4-29}$$

where $|P(f,0)|$ and $|P(f,d)|$ are the amplitude spectra of the acoustic wave at positions x=0 and x=d, respectively, and $\phi(f,0)$ and $\phi(f,d)$ are the phase spectra of the acoustic wave at these positions.

By inserting Equations (4-28) and (4-29) into Equation (4-27), Equations (4-30) and (4-31) can be acquired. Thus, the attenuation $a(f)$ and dispersion $\beta(f)$ factors are obtained, as shown in Equations (4-32) and (4-33):

$$|P(f,d)| = |P(f,0)|e^{-a(f)d} \tag{4-30}$$

$$\phi(f,d) = \phi(f,0) + \beta(f)d \tag{4-31}$$

$$a(f) = -\frac{1}{d}\ln\left|\frac{P(f,d)}{P(f,0)}\right| \tag{4-32}$$

$$\beta(f) = \frac{1}{d}|\phi(f,d) - \phi(f,0)| \tag{4-33}$$

The transfer function which takes into account attenuation and dispersion can described as:

$$G(f,x) = \frac{P(f,x)}{P(f,0)} = e^{-a(f)x}e^{-j\beta(f)x} \tag{4-34}$$

4.2 Recovery of the space charge in a single layer sample under a temperature gradient

4.2.1 Recovery of attenuation and dispersion

In an ideal material, there is no loss of the acoustic wave; it propagates with unchanged magnitude and width. However, the general insulation of materials such as oil and PB can absorb part of the acoustic wave, and lead to attenuation and dispersion. The magnitude of the acoustic wave becomes lower, and it becomes wider after its propagation [51]. Figure 4-4 shows the typical space charge that results in 0.5 mm oil-impregnated PB at a 10 kV/mm electric field. The anode peak is wider and lower than the cathode peak. Thus, the recovery of the acoustic wave due to its attenuation and dispersion needs to be considered. Recovery procedures are described as below.

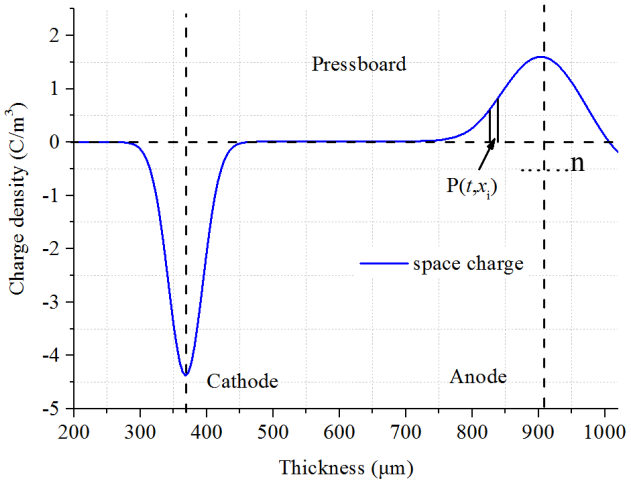

Figure 4-4: The space charge distribution without the attenuation and dispersion recovery.

The output voltage of the acoustic wave can be expressed as:

$$V(t,x_{\mathrm{i}}) = [V(t,x_1), V(t,x_2), \ldots V(t,x_{\mathrm{n}})] \tag{4-35}$$

where x_{i} indicates the charge layer at the position x_{i} for i = 1 to n, for a sample that is divided into n layers, as shown in Figure 4-4.

The charge profile can be converted into the frequency domain shown in Equation (4-36) using a fast Fourier transform (FFT), where $V(f, x_\mathrm{i})$ is the frequency domain of layer x_i of the sample:

$$V(f, x_\mathrm{i}) = FFT\{[V(t, x_1), V(t, x_2), \dots V(t, x_\mathrm{n})]\} = [V(f, x_1), V(f, x_2), \dots V(f, x_\mathrm{n})] \quad (4\text{-}36)$$

$V(f, x_\mathrm{i})$ is the FFT of one layer at position x_i in the time domain. Thus, the sum of each layer in the frequency domain, $V_s(f)$, is the FFT of the total time domain wave:

$$V_s(f) = \sum_{\mathrm{i}=1}^{n} V(f, x_\mathrm{i}) = FFT(\sum_{i=1}^{n} V(t, x_\mathrm{i})) \quad (4\text{-}37)$$

To recover the signal, due to the attenuation and dispersion effect, the inverse of the transfer function, $G^{-1}(f, x_\mathrm{i})$, is acquired from Equation (4-34). The signal recovery is shown in Equation (4-38) below:

$$\rho(f) = G^{-1}(f, x_\mathrm{i}) V_s(f) \quad (4\text{-}38)$$

Using an inverse fast Fourier transform (IFFT), the recovered space charge $\rho(t)$ in the time domain can be represented using the following equation:

$$\rho(t) = IFFT[\rho(f)] \quad (4\text{-}39)$$

4.2.2 Recovery of the space charge under a temperature gradient

(1) Charge magnitude recovery at the vertical axis

The acoustic wave at the anode can be expressed as:

$$P(t) = \mathrm{k}\frac{u}{d}\sigma^{+} e_\mathrm{p}(\mathrm{t}) \quad (4\text{-}40)$$

where u is the acoustic velocity of the sample, d is the sample thickness, and k is the matching coefficient of the acoustic impedance [77].

The acoustic wave generated at the anode at the ambient temperature, $P_0(t)$, can be expressed as:

$$P_0(t) = \mathrm{k}\frac{u_0}{d_0}\sigma^{+} e_\mathrm{p}(t) \quad (4\text{-}41)$$

where u_0 is the acoustic velocity of the sample at ambient temperature.

The acoustic wave generated under a temperature gradient, $P_{\Delta\mathrm{T}}(t)$, can be expressed as:

$$P_{\Delta\mathrm{T}}(t) = \mathrm{k}\frac{u_{\Delta\mathrm{T}}}{d_{\Delta\mathrm{T}}}\sigma^{+} e_\mathrm{p}(t) \quad (4\text{-}42)$$

where $u_{\Delta\mathrm{T}}$ is the acoustic velocity of the sample under the temperature gradient.

By combining Equations (4-41) and (4-42), Equation (4-43) can be obtained in order to recover the charge magnitude at the temperature gradient:

$$P_0(t) = P_{\Delta T}(t)\frac{u_0}{u_{\Delta T}}\frac{d_{\Delta T}}{d_0} \tag{4-43}$$

Thus, the temperature distribution of a single layer sample can be expressed as [15]:

$$T = 20 + \frac{T_h - 20}{d}x \ (0 < x < d) \tag{4-44}$$

The temperature of the bottom electrode is fixed at 20 °C. T_h is the temperature in °C of the upper electrode, and T is temperature in °C at the position x.

The acoustic wave velocity of the PB at different temperatures is presented in Equation (4-45) [15]:

$$u_{\Delta Top} = 3.5137T + 2376 \tag{4-45}$$

where 2376 m/s is the acoustic velocity constant, and 3.5137 is a constant with unit of m/(s°C). By combining Equations (4-43), (4-44) and (4-45), the vertical of the space charge density can be recovered.

(2) Time calibration at the horizontal axis

The resolution of the system, Δx, at ambient temperature can be expressed as:

$$\Delta x = u_0/f_s \tag{4-46}$$

where f_s is the sampling frequency of the oscilloscope.

The resolution of the system under a temperature gradient can be expressed as:

$$\Delta x' = u_{\Delta T}/f_s \tag{4-47}$$

where $\Delta x'$ is the resolution of the system under a temperature gradient.

Based on Equation (4-47), the time calibration at the horizontal axis can be recovered. The recovery of the space charge that results from a sample of single-layer oil-impregnated PB with a 20 °C temperature gradient at 1 kV is shown in Figure 4-5. Raw space charge represents the space charge in the sample after the attenuation and dispersion recovery. Figure 4-5 also shows the space charge that results from both vertical and horizontal recovery.

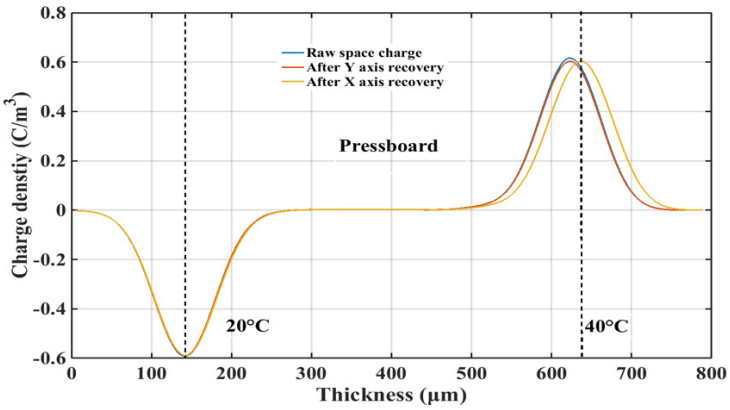

Figure 4-5: The recovery of the space charge in a sample of single-layer PB with a 20 °C temperature gradient.

The algorithm for space charge recovery under a temperature gradient is summarised in Figure 4-6.

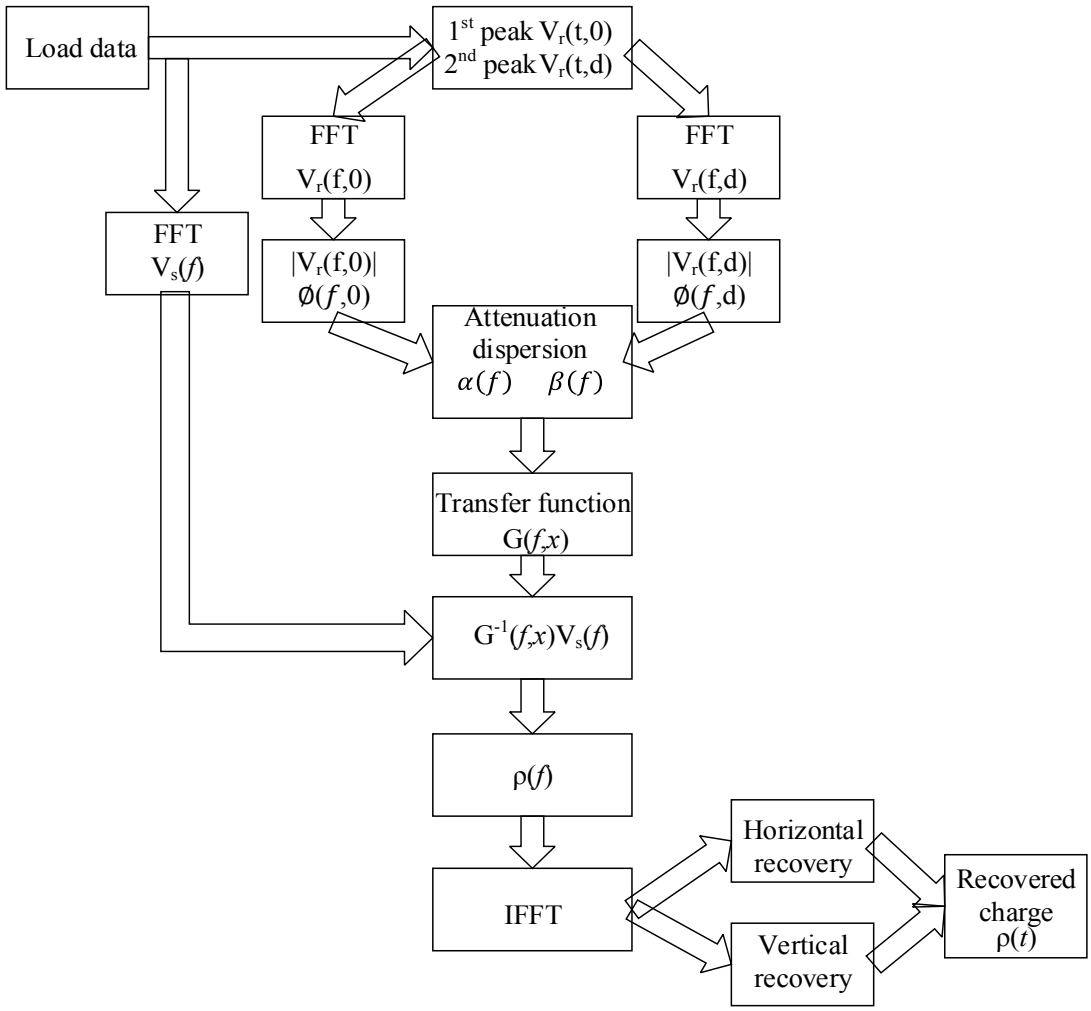

Figure 4-6: The algorithm for space charge recovery under a temperature gradient.

4.3 Space charge recovery in two-layer samples under a temperature gradient

The PEA output signal does not directly represent the space charge distribution in multilayer samples [16] in the presence of temperature gradient. There are three main reasons for this. Firstly, a transient pulse voltage induces transient forces within the layers, which generates the acoustic wave to be detected. Considering the fact that a multilayer sample has different electric properties to a single layer sample, the transient force will not only depend on the space charge, but also on the dielectric permittivities of the different materials. Secondly, the PEA signal depends on the propagation of acoustic waves within the materials. In multilayer samples, the acoustic wave may experience different generation, transmission, reflection, attenuation, and dispersion coefficients, leading to difficulties in interpreting the original acoustic signal propagation of the wave. Thirdly, temperature affects the velocity of the acoustic wave, changing the magnitude and resolution of the PEA system. Therefore, recovery of the space charge is important to ensure that the correct pattern is acquired for electrically, acoustically, and thermally inhomogeneous multilayered dielectric materials [78]. The methodology for space charge recovery in multilayer samples is described below, based on the following aspects.

4.3.1 Temperature measurement

The temperature distribution in two layers of insulated materials is not uniform due to thermal resistance in the presence of a temperature gradient. The temperature distribution should be obtained for both layers at the given temperature to make the relevant space charge recovery. Therefore, both the thermal theatrical calculations and the real temperature measurements will be conducted for a two-layer sample, composed of oil and oil-impregnated PB.

The thermal resistance is calculated as follows:

$$\mathrm{B} = \frac{\mathrm{d}}{\lambda \mathrm{A}} \tag{4-48}$$

where B (K/W) is the thermal resistance, λ (W/(mK)) is the thermal conductivity, and A (m^2) is the area of the upper electrode. The thickness of the PB, $d_{PB,}$ and the oil, $d_{OIL,}$ are both 0.5 mm. The thickness of the semicon, d_{SC}, is 0.15mm. The thermal conductivity of the PB, λ_{PB}, the oil, λ_{OIL}, and the semicon, λ_{SC}, are 0.19 W/(mK), 0.15 W/(mK), and 0.3 W/(mK), respectively. A is 7.85×10^{-5} m^2.

The heat flow Φ (W) can be expressed as:

$$\Phi = \frac{T_{\mathrm{U}} - T_{\mathrm{L}}}{B_{\mathrm{SC}} + B_{\mathrm{OP}} + B_{\mathrm{OIL}}} \tag{4-49}$$

where Φ (W) is the heat flow, and T_{U} and T_{L} represent the temperatures of the upper and bottom

electrodes. $B_{\mathrm{SC}}, B_{\mathrm{OP}},$ and B_{OIL} are the thermal resistances of the semicon, the PB and the oil, respectively.

The temperature across the two layers of oil and PB can be expressed as:

$$\Delta \mathrm{T} = \Phi(B_{\mathrm{OP}} + B_{\mathrm{OIL}}) \tag{4-50}$$

where ΔT is the temperature drop across the two layers. The temperature of the bottom electrode, T_{L}, is fixed at 20 °C. The temperature of the upper electrode T_{U} can be calculated based on Equations (4-48), (4-49) and (4-50). The results of these calculations are shown in Table 4-1. The temperature drop across the semicon leads to the differences between the reference values and the calculation results.

Furthermore, the temperature of the upper electrode can be acquired using two thermocouples to measure the actual temperature gradient across the samples. These values are slightly higher than the calculated values due to thermal losses. For the following space charge experiments, the measured temperature values were used to guarantee the exact temperature gradient across the samples.

Table 4-1: The theoretical and experimental temperatures of the upper electrode

Description	Temperature				
Reference T_{U} °C	20	30	40	50	60
Calculation T_{U}°C	20	31	41	53	64
Measurement T_{U}°C	20	33	46	57	69

4.3.2 Acoustic velocity versus temperature

The acoustic velocities of the oil and the PB at different external temperatures should be measured when performing space charge recovery under a temperature gradient. In order to achieve this, the temperatures of both electrodes were increased from 20 °C to 60 °C at 10 °C intervals, and the acoustic velocities of the oil and the PB at each temperature were calculated based on the following equations:

$$u_{oil} = \frac{d_{\mathrm{oil}}}{t_{\mathrm{oil}}} \tag{4-51}$$

$$u_{op} = \frac{d_{\mathrm{op}}}{t_{\mathrm{op}}} \tag{4-52}$$

$$u_{\mathrm{a}}\left(t_{\mathrm{oil}} + t_{\mathrm{op}}\right) = d_{\mathrm{oil}} + d_{\mathrm{op}} \tag{4-53}$$

where u_{oil} (m/s) and u_{op} (m/s) represent the acoustic velocity of the oil and the PB, d_{oil} (m) and d_{op} (m) are the thickness of the oil and the PB, t_{oil} (s) and t_{op} (s) indicate the time interval of oil and PB, and u_a (m/s) is the average acoustic velocity of both the oil and the PB. Because the acoustic wave of the oil cannot be measured from the PEA equipment directly, it was calculated based on Equations (4-51) to (4-53).

Figure 4-7 shows the acoustic velocity versus temperature for both the oil and the oil-impregnated PB. It indicates that while the acoustic velocity of the PB increases with temperature, the acoustic velocity of the oil decreases with temperature. Based on the curve-fitting function in Matlab, the acoustic velocity versus temperature equations for oil and PB can be summarised as follows:

$$\text{Oil}: u_{\mathrm{oil}} = -7.476T + 1866 \tag{4-54}$$

$$\text{PB}: u_{\mathrm{op}} = 3.5137T + 2376 \tag{4-55}$$

where -7.476 is a constant with measured in m/(s°C) and 1866 m/s is the acoustic velocity constant.

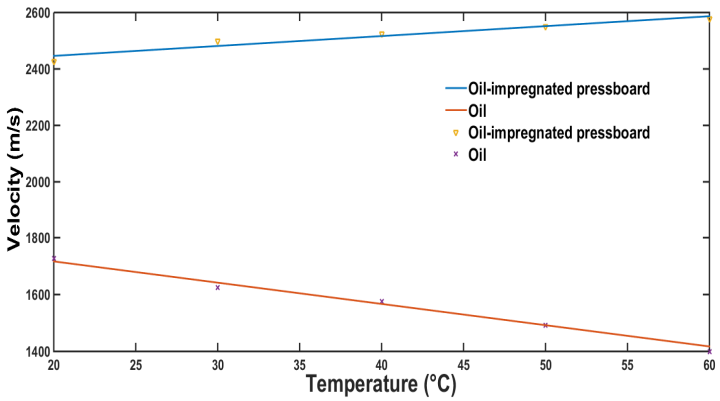

Figure 4-7: Acoustic velocity versus temperature for oil and PB.

The acoustic velocities of the oil and the PB are different at ambient temperature. Based on the equations (3-12) and (3-13). The calculated spatial resolutions of oil and PB are around 31 μm and 43 μm, respectively.

4.3.3 Temperature distribution simulation

The temperature at the interface of the oil and the PB is difficult to measure. To acquire this value, the temperature gradient distribution of the two layers was simulated using COMSOL. The model contains two parallel layers of oil and PB, each of thickness is 0.5 mm. The thermal conductivity of the PB, λ_{op}, and the oil, λ_{oil}, are 0.19 W/(mK) and 0.15 W/(mK), respectively. The density of the PB is 1200 kg/m^3 and the density of the oil is 910 kg/m^3. The heat capacity of the PB is 1381.644 J/(kgK) and of the oil is 1670 J/(kgK). The temperatures of the upper and bottom

electrodes were set to 41°C and 20°C, respectively according to the calculation results shown in Table 4-1.

Figure 4-8 shows that the temperature at the interface of the oil and PB layers in a 20 °C temperature gradient is 31.3 °C. The majority of the temperature change is seen across the oil due to its lower thermal conductivity. Furthermore, when the temperature of the upper and bottom electrodes is set to 20°C and 40°C respectively, the temperature at the PB and oil interface is 29.6 °C.

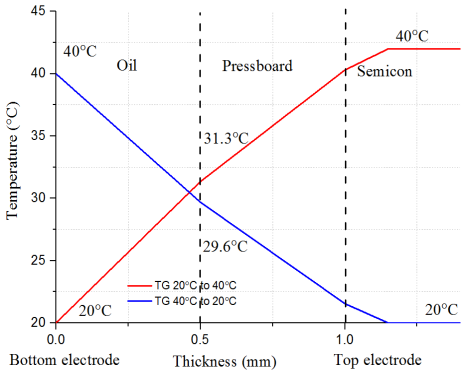

Figure 4-8: The temperature distribution of a two-layer sample consisting of oil and PB under a 20°C temperature gradient.

4.3.4 Acoustic wave propagation

Given that oil and PB are electrically and acoustically inhomogeneous, the recovery of the space charge needs to consider the following aspects.

(1) The non-uniformity of the pulse distribution

In multilayer samples, the pulse voltage distribution is not uniform across the oil and PB layers. The pulse electric field is capacitive distribution determined by the dielectric constant. A_{p} is the ratio between the transient pulse electric field of the oil and that of the PB, and can be expressed as follows:

$$A_{\mathrm{p}} = \frac{E_{\mathrm{oil}}}{E_{\mathrm{op}}} = \frac{\varepsilon_{\mathrm{op}}}{\varepsilon_{\mathrm{oil}}} = 1.46 \tag{4-56}$$

The transient pulse electric field of the oil is 1.46 times as high as that of the PB. Taking the acoustic wave of the oil as the point of reference, the acoustic wave of the PB should be multiplied by A_{p} to eliminate the differences caused by the different dielectric constants of the materials.

(2) Attenuation and dispersion

For a single layer sample, the attenuation, $a(f)$, and dispersion, $\beta(f)$, can be calculated directly based on Equations (4-32) and (4-33). Thus, the attenuation, $a_{\mathrm{op}}(f)$, and dispersion, $\beta_{\mathrm{op}}(f)$, of the PB are calculated directly. However, for a two-layer sample of oil and PB, the attenuation and dispersion of the individual materials should be calculated separately for recovering the space charge. To acquire the attenuation, $a_{\mathrm{oil}}(f)$, and dispersion, $\beta_{\mathrm{oil}}(f)$, of the oil, a transfer function can be calculated based on the definition expressed in the following equation:

$$G(f,x) = \frac{|P(f,d)|^{\frac{x}{d}}}{|P(f,0)|} e^{-j\frac{x}{d}[\emptyset(f,d)-\emptyset(f,0)]} \tag{4-57}$$

The transfer function of acoustic wave propagation in two layers oil and PB is shown in the following equation:

$$G(f,x) = \frac{P(f,d)}{P(f,0)} = \frac{1}{A_{\mathrm{p}}} TG e^{-\alpha_{\mathrm{op}}(f)d_{\mathrm{op}} - j\beta_{\mathrm{op}}(f)d_{\mathrm{op}}} e^{-\alpha_{\mathrm{oil}}(f)d_{\mathrm{oil}} - j\beta_{\mathrm{oil}}(f)d_{\mathrm{oil}}} \tag{4-58}$$

where T is the transmission factor at the oil–PB interface and G is the generation factor in the PB. With the combination of these two Equations (4-57) and (4-58), the attenuation factor, $a_{\mathrm{oil}}(f)$, and dispersion factor, $\beta_{\mathrm{oil}}(f)$, factors of the oil can be deduced, as shown in the following equations:

$$\alpha_{\mathrm{oil}}(f) = \frac{1}{d_{\mathrm{oil}}} \ln\left(\frac{|P(f,0)|}{|P(f,d)|} TG \frac{1}{A_{\mathrm{p}}}\right) - \alpha_{\mathrm{op}}(f)\frac{d_{\mathrm{op}}}{d_{\mathrm{oil}}} \tag{4-59}$$

$$\beta_{\mathrm{oil}}(f) = \frac{1}{d_{\mathrm{oil}}}[\emptyset(f,d) - \emptyset(f,0)] - \frac{d_{\mathrm{op}}}{d_{\mathrm{oil}}}\beta_{\mathrm{op}}(f) \tag{4-60}$$

(3) Acoustic propagation in a two-layer sample of oil and PB

Acoustic impedance is calculated based on Equation (4-9) above. The density and acoustic velocities of different materials are shown in Table 4-2. Based on these values, the generation, transmission, and reflection coefficients can be calculated based on Equations (4-10), (4-11) and (4-12).

Table 4-2: The acoustic properties of dielectric materials [79]

Materials	Density, ρ (kg/m^3)	Acoustic velocity, u (m/s)	Acoustic impedance, Z (10^6 kg/m^{2}s)
Mineral oil	0.85×10^3	1716	1.46
PB	1.2×10^3	2446	2.94
Semicon	1.1×10^3	2300	2.5
Aluminium	2.69×10^3	6420	17.3

Figure 4-9 shows the propagation of the acoustic wave in a two-layer sample of oil and PB. The pressure wave generated by the oil and the PB towards the ground electrode in the frequency domain is described as:

$$P_1(f) = P(f)G_1T_{1A}e^{-\alpha_{oil}(f)x-j\beta_{oil}(f)x} = A_1(f,x)P(f) \qquad 0 < x < d_{oil} \tag{4-61}$$

$$P_{1i}(f) = P(f)G_{21}T_{1A}e^{-\alpha_{oil}(f)d_{oil}-j\beta_{oil}(f)d_{oil}} = A_{1i}(f,x)P(f) \qquad x = d_{oil} \tag{4-62}$$

$$P_2(f) = \frac{1}{A_p}P(f)G_2T_{1A}T_{21}e^{-\alpha_{op}(f)(x-d_{oil})-j\beta_{op}(f)(x-d_{oil})}e^{-\alpha_{oil}(f)d_{oil}-j\beta_{oil}(f)d_{oil}} \tag{4-63}$$

$$= A_2(f,x)P(f) \qquad d_{oil} < x < d_{oil} + d_{op}$$

$$P_{2i}(f) = \frac{1}{A_p}PG_{B2}T_{21}T_{1A}e^{-\alpha_{op}(f)(d_{oil}+d_{op})-j\beta_{oil}(d_{oil}+d_{op})} \tag{4-64}$$

$$= A_{2i}(f,x)P(f) \qquad x = d_{oil} + d_{op}$$

where $P_1(f)$, $P_{1i}(f)$, $P_2(f)$ and $P_{2i}(f)$ are the acoustic waves generated in the oil, at the oil–PB interface, in the PB, and at the PB–semicon interface, respectively. $P(f)$ is generated acoustic wave. G_1, G_{21} G_2, G_{B2} are the generation factors of the oil, the oil–PB interface, the PB, and the PB–semicon interface, respectively. T_{1A} and T_{21} are the transmission factors at the oil–aluminium interface and the oil–PB interface, respectively.

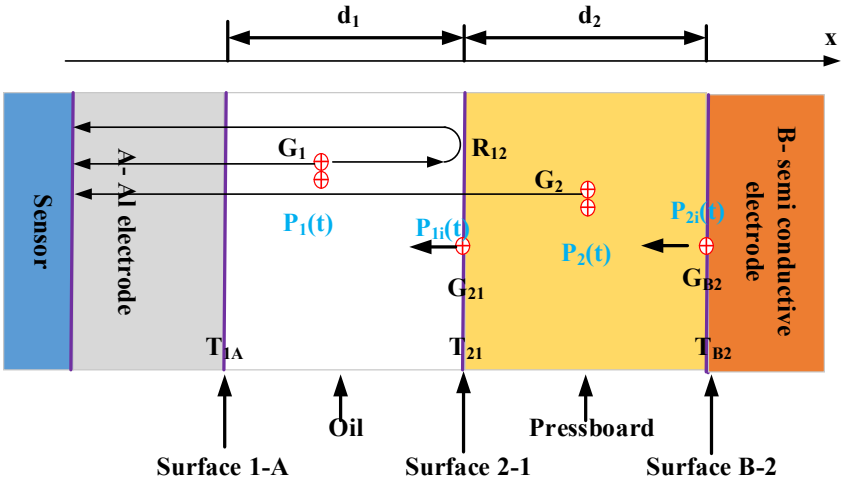

Figure 4-9: The propagation of the acoustic wave in a two-layer sample of oil and PB.

The transfer function $A_{s1}(f,x)$ can be simplified into the equation below:

$$A_{s1}(f,x) = [A_1(f,x), A_{1i}(f,x), A_2(f,x), A_{2i}(f,x)] \tag{4-65}$$

where $A_1(f,x), A_{1i}(f,x), A_2(f,x)$ and $A_{2i}(f,x)$ show the transfer functions in the oil, at the oil–PB interface, in the PB, and at the PB–semicon interface, respectively.

To recover the signal, considering the acoustic generation, transportation, and different dielectric properties of multilayer materials, the inverse of the transfer function, ${A_{s1}}^{-1}(f,x)$, which can be calculated from Equation (4-65), as shown below:

$$\rho(f) = {A_{s1}}^{-1}(f,x)V_s(f) \tag{4-66}$$

Using an inverse fast Fourier transform (IFFT), the recovered space charge, $\rho(t)$, in the time domain can be represented using the following equation:

$$\rho(t) = IFFT[\rho(f)] \tag{4-67}$$

4.3.5 Recovery of the space charge under a temperature gradient

For a two-layer sample of oil and PB, the recovery of the space charge under a temperature gradient can be used to obtain the vertical magnitude of the acoustic wave recovery, based on the following equation:

$$P_0(t) = \begin{cases} P_{\Delta\mathrm{T}}(t)\dfrac{u_{\mathrm{oil}}}{u_{\Delta\mathrm{Toil}}}\dfrac{d_{\Delta\mathrm{Toil}}}{d_{\mathrm{oil}}}, & x < d_{\mathrm{oil}} \\ P_{\Delta\mathrm{T}}(t)\dfrac{u_{\mathrm{op}}}{u_{\Delta\mathrm{Top}}}\dfrac{d_{\Delta\mathrm{Top}}}{d_{\mathrm{op}}}, & d_{\mathrm{oil}} < x < d_{\mathrm{oil}} + d_{\mathrm{op}} \end{cases} \tag{4-68}$$

where x is the position of the acoustic wave, and u_{oil} and u_{op} are the acoustic wave velocity of the oil and the PB at the ambient temperature, respectively. $u_{\Delta\mathrm{Toil}}$ and $u_{\Delta\mathrm{Top}}$ are the acoustic waves of the oil and the PB with a temperature gradient, d_{oil} and d_{op} are the thickness of the oil and the PB at ambient temperature, and $d_{\Delta\mathrm{Toil}}$ and $d_{\Delta\mathrm{Top}}$ are the thickness of oil and the PB under the temperature gradient.

The time recovery of the horizontal axis can be expressed by the following equations:

$$\Delta x = \begin{cases} u_{\mathrm{oil}}/f_{\mathrm{s}} \\ u_{\mathrm{op}}/f_{\mathrm{s}} \end{cases} \tag{4-69}$$

$$\Delta x' = \begin{cases} u_{\Delta\mathrm{Toil}}/f_{\mathrm{s}} \\ u_{\Delta\mathrm{Top}}/f_{\mathrm{s}} \end{cases} \tag{4-70}$$

where Δx and $\Delta x'$ are the resolution of the system at ambient temperature and under a temperature gradient. f_{s} is the sampling frequency of the oscilloscope.

Figure 4-10 shows the recovery of the space charge in a two-layer sample of 0.5 mm oil and 0.5 mm PB with a temperature gradient of 20 °C. The oil and PB are stressed at 10 kV. The graph shows both the vertical and horizontal recovery. The anode makes a shift to the left as a result of the horizontal axis recovery , mostly because the acoustic wave velocity of the oil decreases as the temperature increases, which leads to a lower average velocity across the oil and the PB.

Conversely, Figure 4-11 shows the space charge recovery in a two-layer sample of 0.5 mm oil and 0.5 mm PB with a reversed temperature gradient of 20 °C. The oil and PB are again stressed at 10 kV, the graph once again shows both the vertical and horizontal recovery. This time the cathode makes a shift to the left as a result of horizontal axis recovery because the acoustic wave velocity of the oil decreases as the temperature increases, so it takes longer for the acoustic wave generated in the oil to reach the piezoelectric transducer.

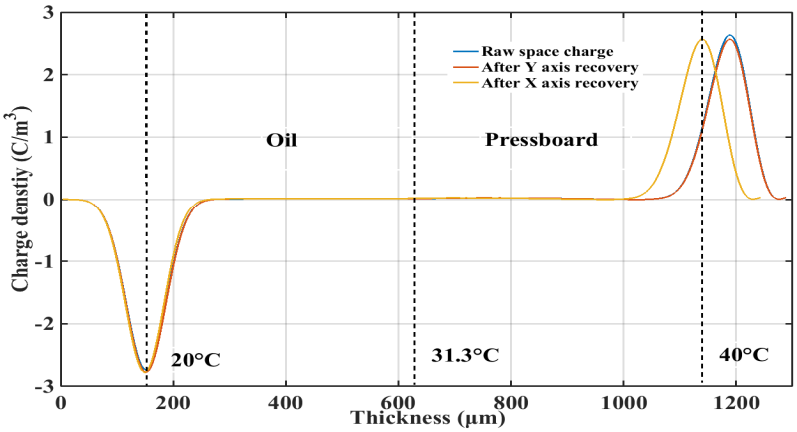

Figure 4-10: The space charge recovery of a two-layer sample of oil and PB with a 20 °C temperature gradient.

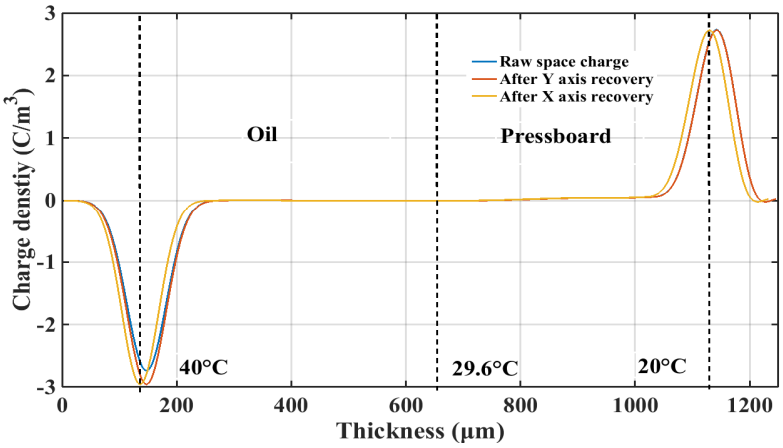

Figure 4-11: The space charge recovery of a two-layer sample of oil and PB with a reversed 20 °C temperature gradient.

4.4 The recovery of the space charge in three-layer samples with a temperature gradient

4.4.1 Temperature gradient distribution

Figure 4-12 shows the temperature gradient distribution in a three-layer sample of PB, oil, and

PB with a temperature gradient. The temperature of the upper and bottom electrodes is set to 41°C and 20 °C, respectively. The two intermediate interface temperatures are 33.8 °C and 26.1 °C. Moreover, when the temperature gradient is reversed, with the temperature of the upper and bottom electrodes set to 20 °C and 40 °C, respectively, the two intermediate interface temperatures are 34.2 °C and 26.9 °C.

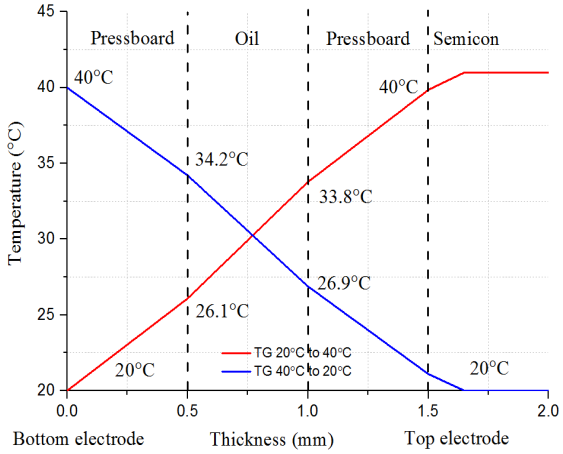

Figure 4-12: The temperature distribution in a three-layer sample of PB, oil, and PB.

4.4.2 Propagation of the acoustic wave in a three-layer sample.

For recovery of the space charge in multilayer samples, the attenuation and dispersion of the materials should be calculated separately.

The general transfer function can be expressed as equation (4-57).

Moreover, the acoustic wave propagation in a multilayer sample of oil and PB can be expressed as:

$$G(f,x)=\frac{P(f,d)}{P(f,0)}=\frac{1}{A_{\mathrm{p}}}TGe^{-N\alpha_{\mathrm{op}}(f)d_{\mathrm{op}}-jN\beta_{\mathrm{op}}(f)d_{\mathrm{op}}}e^{-M\alpha_{\mathrm{oil}}(f)d_{\mathrm{oil}}-jM\beta_{\mathrm{oil}}(f)d_{\mathrm{oil}}} \tag{4-71}$$

It is assumed that the samples have N layers of PB and M layers of oil. It is also assumed that layers made of the same materials have similar attenuation and dispersion factors.

By combining Equations (4-57) and (4-71), the attenuation and dispersion factors of the oil can be deduced as shown in Equations (4-72) and (4-73). If N=2 and M=1, the Equations (4-72) and (4-73) can be simplified to Equations (4-74) and (4-75), respectively.

$$\alpha_{\mathrm{oil}}(f)=\frac{1}{Md_{\mathrm{oil}}}ln\frac{|P(f,0)|}{|P(f,d)|}TG\frac{1}{A_{\mathrm{p}}}-\frac{N}{M}\alpha_{\mathrm{op}}(f)\frac{d_{\mathrm{op}}}{d_{\mathrm{oil}}} \tag{4-72}$$

$$\beta_{\mathrm{oil}}(f)=\frac{1}{Md_{\mathrm{oil}}}[\emptyset(f,d)-\emptyset(f,0)]-\frac{N}{M}\frac{d_{\mathrm{op}}}{d_{\mathrm{oil}}}\beta_{\mathrm{op}}(f) \tag{4-73}$$

$$\alpha_{oil}(f) = \frac{1}{d_{\mathrm{oil}}} ln \frac{|P(f,0)|}{|P(f,d)|} TG \frac{1}{A_{\mathrm{p}}} - 2\alpha_{\mathrm{op}}(f) \frac{d_{\mathrm{op}}}{d_{\mathrm{oil}}} \tag{4-74}$$

$$\beta_{\mathrm{oil}}(f) = \frac{1}{d_{\mathrm{oil}}} [\emptyset(f,d) - \emptyset(f,0)] - 2\frac{d_{\mathrm{op}}}{d_{\mathrm{oil}}} \beta_{\mathrm{op}}(f) \tag{4-75}$$

Figure 4-13 indicates the acoustic wave propagation process in a three-layer sample of PB, oil, and PB. The pressure wave generated in the oil and the PB towards the ground electrode can be described as follows:

$$P_1(f) = \frac{1}{A_{\mathrm{p}}} P(f) G_1 T_{1\mathrm{A}} e^{-\alpha_{\mathrm{op}}(f)x - j\beta_{\mathrm{op}}(f)x} = A_1(f,x)P(f) \qquad 0 < x < d_{oil} \tag{4-76}$$

$$P_{1\mathrm{i}}(f) = \frac{1}{A_{\mathrm{p}}} P(f) G_{21} T_{1\mathrm{A}} e^{-\alpha_{\mathrm{op}}(f)d_{\mathrm{op}} - j\beta_{\mathrm{op}}(f)d_{\mathrm{op}}} = A_{1\mathrm{i}}(f,x)P(f) \qquad x = d_{oil} \tag{4-77}$$

$$P_2(f) = P(f) G_2 T_{1\mathrm{A}} T_{21} e^{-\alpha_{\mathrm{oil}}(f)(x-d_{\mathrm{op}}) - j\beta_{\mathrm{oil}}(f)(x-d_{\mathrm{op}})} e^{-\alpha_{\mathrm{op}}(f)d_{\mathrm{op}} - j\beta_{\mathrm{op}}(f)d_{\mathrm{op}}} \tag{4-78}$$

$$= A_2(f,x)P(f) \qquad d_{oil} < x < d_{oil} + d_{op}$$

$$P_{2\mathrm{i}}(f) = P(f) G_{32} T_{21} T_{1\mathrm{A}} e^{-\alpha_{\mathrm{oil}}(f)(d_{\mathrm{oil}}+d_{\mathrm{op}}) - j\beta_{oil}(d_{\mathrm{oil}}+d_{\mathrm{op}})} \tag{4-79}$$

$$= A_{2\mathrm{i}}(f,x)P(f) \qquad x = d_{oil} + d_{op}$$

$$P_3(f) = \frac{1}{A_{\mathrm{p}}} P(f) G_3 T_{1\mathrm{A}} T_{21} T_{32} e^{-\alpha_{\mathrm{op}}(f)(x-d_{\mathrm{op}}-d_{\mathrm{oil}}) - j\beta_{\mathrm{oil}}(f)(x-d_{\mathrm{op}}-d_{\mathrm{oil}})} \tag{4-80}$$

$$e^{-\alpha_{\mathrm{oil}}(f)d_{\mathrm{oil}} - j\beta_{\mathrm{oil}}(f)d_{\mathrm{oil}}} e^{-\alpha_{\mathrm{op}}(f)d_{\mathrm{op}} - j\beta_{\mathrm{op}}(f)d_{\mathrm{op}}}$$

$$= A_3(f,x)P(f) \qquad d_{oil} + d_{op} < x < d_{oil} + 2d_{op}$$

$$P_{3\mathrm{i}}(f) = \frac{1}{A_{\mathrm{p}}} P(f) G_{\mathrm{B3}} T_{1\mathrm{A}} T_{21} T_{32} e^{-2\alpha_{\mathrm{op}}(f)d_{\mathrm{op}} - 2j\beta_{\mathrm{oil}}(f)d_{\mathrm{op}}} e^{-\alpha_{\mathrm{oil}}(f)d_{\mathrm{oil}} - j\beta_{\mathrm{oil}}(f)d_{\mathrm{oil}}} \tag{4-81}$$

$$= A_{3\mathrm{i}}(f,x)P(f) \qquad x = d_{oil} + 2d_{op}$$

where $P_1(f)$, $P_{1\mathrm{i}}(f)$, $P_2(f)$, $P_{2\mathrm{i}}(f)$,$P_3(f)$, $P_{3\mathrm{i}}(f)$ are the acoustic waves generated in the first layer of PB, at the first PB–oil interface, in the oil layer, at the second oil–PB interface, in the second layer of PB, and at the PB–semicon interface, respectively. G_1, G_{21} G_2, G_{32}, G_3 and G_{B3} are the generation factors of the first layer of PB, the first PB–oil interface, the oil, the second oil–PB interface, and the second layer of PB, respectively. $T_{1\mathrm{A}}$, T_{21} and T_{32} are the transmission factors at PB–aluminium interface, the oil–PB interface, and PB–oil interface, respectively.

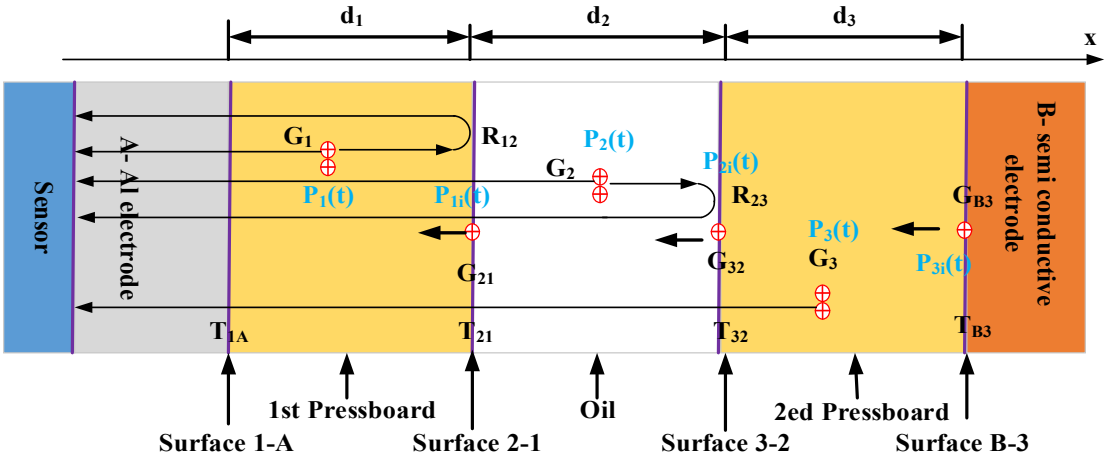

Figure 4-13: A schematic diagram of the acoustic wave propagation within a three-layer sample of PB, oil, and PB [8].

The transfer function $A_s(f,x)$ can be simplified into the equation below:

$$A_{s2}(f,x) = [A_1(f,x), A_{1\mathrm{i}}(f,x), A_2(f,x), A_{2\mathrm{i}}(f,x), A_3(f,x), A_{3\mathrm{i}}(f,x)] \qquad (4\text{-}82)$$

where $A_1(f,x), A_{1\mathrm{i}}(f,x), A_2(f,x), A_{2\mathrm{i}}(f,x), A_3(f,x)$ and $A_{3\mathrm{i}}(f,x)$ are transfer functions generated in the first layer of PB, at the first PB–oil interface, in the oil layer, at the second oil–PB interface, in the second layer of PB, and at the PB–semicon interface, respectively.

To recover the signal, considering the acoustic generation, transportation, and different dielectric properties of multilayer materials, the inverse of the transfer function, ${A_{s2}}^{-1}(f,x)$, can be calculated from Equation (4-82), as shown below:

$$\rho(f) = {A_{s2}}^{-1}(f,x)\, V_s(f). \qquad (4\text{-}83)$$

Using an inverse fast Fourier transform (IFFT), the recovered space charge, $\rho(t)$, in the time domain can be represented using the following equation:

$$\rho(t) = IFFT[\rho(f)] \qquad (4\text{-}84)$$

4.3.3 Recovery of the space charge under a temperature gradient

The vertical magnitude of the recovery of the acoustic wave in a three-layer sample of PB, oil, and PB under a temperature gradient can be expressed as follows:

$$P_0(t) = \begin{cases} P_{\Delta T}(t)\dfrac{u_{op}}{u_{\Delta Top}}\dfrac{d_{\Delta Top}}{d_{op}}, & x < d_{op} \\ P_{\Delta T}(t)\dfrac{u_{oil}}{u_{\Delta Toil}}\dfrac{d_{\Delta Toil}}{d_{oil}}, & d_{op} < x < d_{oil} + d_{op} \\ P_{\Delta T}(t)\dfrac{u_{op}}{u_{\Delta Top}}\dfrac{d_{\Delta Top}}{d_{op}}, & d_{oil} + d_{op} < x < d_{oil} + 2d_{op} \end{cases} \quad (4\text{-}85)$$

Using Equation (4-87) below, the horizontal time recovery can be acquired based on the real acoustic velocity under a temperature gradient.

$$\Delta x = \begin{cases} u_{op}/f_s \\ u_{oil}/f_s \\ u_{op}/f_s \end{cases} \quad (4\text{-}86)$$

$$\Delta x' = \begin{cases} u_{\Delta Top}/f_s \\ u_{\Delta Toil}/f_s \\ u_{\Delta Top}/f_s \end{cases} \quad (4\text{-}87)$$

Figure 4-14 shows the recovery of the acoustic wave in a three-layer sample of PB, oil, and PB with a temperature gradient of 20°C. The three-layer sample are stressed at 15 kV. The graph shows both the vertical and horizontal recovery. The acoustic wave velocity of the oil increases and that of the PB decreases as the temperature increases, leading to a lack of obvious change of the average velocity [15]. Therefore, the anode peak shifts slightly to the left after horizontal axis recovery.

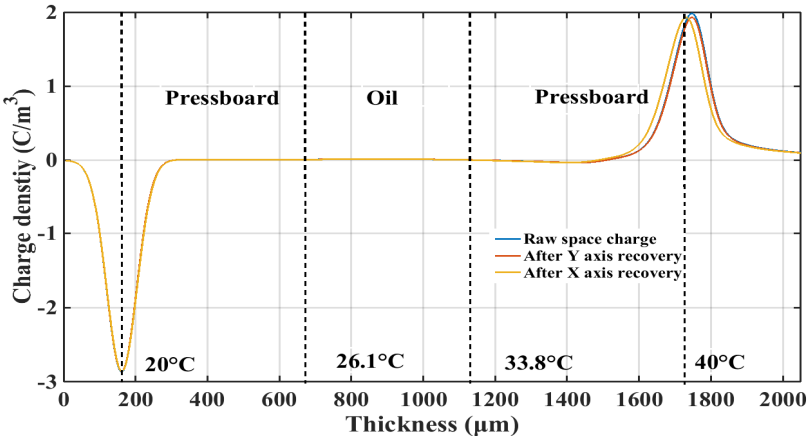

Figure 4-14: The recovery of the space charge in a three-layer sample of PB, oil, and PB with a 20 °C temperature gradient.

4.5 Summary

This chapter mainly describes the recovery of the space charge under a temperature gradient. Firstly, the basic principles of the PEA method were introduced. The pulse electric field perturbs

the charge and generates an acoustic wave. The acoustic wave, $P(t)$, propagates through the different materials depending on their acoustic impedance, Z. When it propagates through the aluminium and is applied to the piezo transducer sensor, an amount of charge, $q(t)$, is induced on both surfaces of the transducer, creating the induced voltage, $V_{\mathrm{PVDF}}(t)$. This voltage signal is amplified to give the output voltage $V_{\mathrm{s}}(t)$. Using the deconvolution method, the output voltage can be converted into the space charge, $\rho(t)$. During acoustic wave propagation, attenuation and dispersion may be experienced after its propagation into dispersive materials. Therefore, it is necessary to recover the acoustic wave.

A methodology for recovery of the space charge in oil and PB with a temperature gradient is firstly proposed. Based on the proposed recovery algorithm, the correct space charge pattern can be collected for the electrically, acoustically and thermally inhomogeneous multilayers dielectric materials. For one layer of PB, the attenuation and dispersion of the acoustic wave are considered. Both vertical magnitude and horizontal time recovery methods in one layer of PB are proposed. For multilayer samples of oil and PB, the attenuation factors, dispersion factors, and acoustic velocities of the individual materials must be calculated separately. The acoustic velocity of the PB and oil has the different trend with an increased temperature. The acoustic velocity of the PB increases while that of the oil decreases with an increased temperature. A transfer function, including different pulsed electric fields, acoustic wave generation and transmission factor effects, is considered for recovery of the space charge in multilayer samples. Based on the proposed space charge recovery methodology for multilayer samples with a temperature gradient, the effect of that temperature gradient on the space charge behaviour of such samples will be described in the next chapter.

Chapter 5 Space charge behaviour of oil and PB with a temperature gradient

The temperature gradient and multilayer structure of oil and PB raise concerns about space charge on the electrical performance and life expectation of converter transformers under high DC electric fields. This chapter firstly introduces research motivations and the procedures of sample preparation. The experimental investigation of space charge in the multilayers of oil and PB at a specific temperature gradient are reported. The effects of temperature gradient and the multilayer on dynamics of space charge results are presented and discussed.

5.1 Motivations and sample preparation

Space charge formation is regarded as a major issue to be addressed for the development of HVDC equipment such as converter transformers. The existence of space charge can distort electric fields and enhance local electric fields in some regions, which can subsequently accelerate the degradation and even breakdown of insulation [4]. Therefore, it is important to investigate the factors that affect space charge formation and dissipation such as temperature, moisture, ageing, multilayers, thickness, and electric fields [48][64][66][80][81].

Mineral oil provides dual functions as an insulator and cooling material [5]. This is because the oil duct is always designed to be located at the bottom of the transformer tank, and gradually circulate to the outlet at the top of the tank. Therefore, the temperature of the oil at the top part is always higher than that at the bottom part of the transformer [6]. Moreover, the temperature gradient exists between different voltage ratings of windings. The temperature of the low voltage winding near the core is higher compared to that of the high voltage winding, establishing the temperature gradient across the intermediate insulation materials.

In a high voltage insulation system, a combination of different dielectric materials is used. Consequently, interfaces are very common in high voltage electric equipment [65]. Typical examples are converter transformers, where two different dielectric materials are combined, containing both oil and PB. Under DC voltage, the interface is the preferred position for the space charge accumulation. The broken bonds and additional extra chains at the interface may be regarded as deep traps for the space charge accumulation [34][66][67]. Therefore, it is extremely important to investigate the temperature gradient effect on the space charge behaviour of multilayer oil and PB.

Sample preparations procedures are summarised via the flow chart in Figure 5-1. The PB was provided by Taizhou Weidmann High Voltage Insulation Co. Ltd, and had a thickness of 0.5 mm.

The oil was fresh mineral oil (ZXI-S3), provided by the Shell Company.

The PB was cut into circles with a diameter of 9 cm. As the performance of the PB is heavily determined by moisture content [10], the PB was dried at 105 °C in a fan-assisted oven for three days to ensure it was well-dried, with a maximum moisture content of 0.5%.

The electric properties of oil are significantly deteriorated by the absorption of gas and moisture [10]. Moisture and gas can be effectively eliminated by a vacuum-degassing system. Mineral oil should be degassed in a vacuum chamber to remove moisture and gas prior to oil and PB impregnation. A magnetic stirrer was used to facilitate gas and moisture removal from the mineral oil. Generally, mineral oil is degassed at 105°C for three hours. Typically, a residual water content in dried mineral oil is less than 5 ppm.

The cavities and pores between fibres in PB are eliminated via oil impregnation. Generally, the PB is impregnated with the oil in the vacuum phase in order to reduce the trapped gas [10]. Due to slow diffusion and dissolution processes, the oil and PB required three days of impregnation process at a temperature of 60°C and 200 mbar in a vacuum oven. Following the impregnation process, the samples were moved from the vacuum oven to the desiccator containing silicone gel to limit the moisture absorption. Four days of standing time was required at an ambient temperature prior to conducting the relative experiments [80].

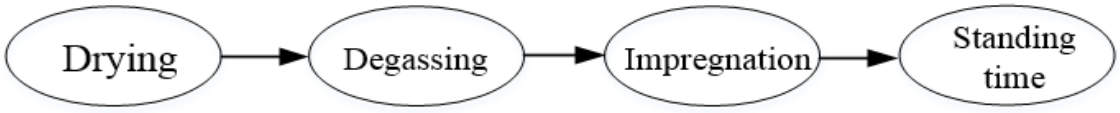

Figure 5-1: A schematic diagram of the oil and PB impregnation process.

Table 5-1: Experiment plan for space charge measurements

	Voltage	Sample	Thickness (μm)	Electric field (kV/mm)	Temperature gradient (°C)
One layer	DC (+)	PB	500	10	0, 20, 40, -20
Two layers	DC (+)	PB+oil	2×500	10	0, 20, 40, -20
Three layers	DC (+)	PB+oil+PB	3×500	10	0, 20, 40, -20

Following the sample preparation, in order to understand the temperature gradient effect on the space charge behaviour of the multilayer oil and PB, four test conditions were designed: i) no temperature gradient; ii) 20°C temperature gradient; iii) 40°C temperature gradient; iv) -20°C temperature gradient. The insulation samples comprised one-layer oil PB, two-layer PB and oil,

and three-layer PB oil and PB. Details are provided in Table 5-1.

5.2 Space charge behaviour of one-layer PB at the temperature gradient

5.1.1 Space charge behaviour

Figure 5-2 (a) shows space charge distribution in the 0.5 mm oil-impregnated PB at 10 kV/mm at an ambient temperature (AT). Homocharge injection is obvious from both electrodes. Figure 5-2 (b) is space charge in the one-layer 0.5 mm oil-impregnated PB with a 20°C temperature gradient (TG). A number of positive charges are injected from the high temperature electrode and migrate to the bulk of insulation materials, resulting in an increase in the electric field close to the cathode. Figure 5-2 (c) shows space charge in the one-layer 0.5 mm oil-impregnated PB with a 40°C temperature gradient. A significant amount of positive charges is injected from the high temperature anode and moves into the bulk of insulation materials, leading to electric field enhancement within the sample close to the cathode. Figure 5-2 (d) shows the space charge in one-layer oil-impregnated PB with a -20°C temperature gradient. The homocharge injection is obvious, particularly for the electrons, due to the high temperature of the bottom electrode.

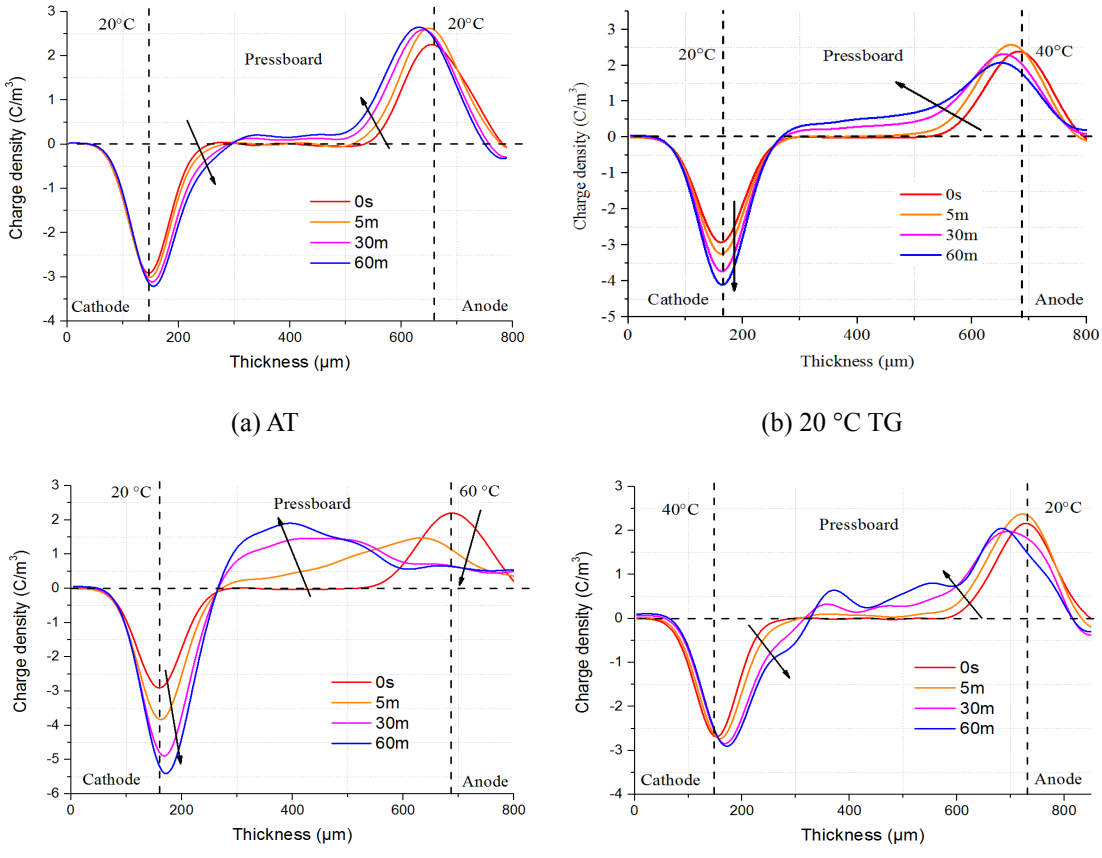

Figure 5-2: Space charge for one layer of oil-impregnated PB under 10 kV/mm.

The decay test measures the relaxation of space charge after the voltage is removed. Figure 5-3 (a) shows the decay result of space charge for one-layer PB at ambient temperature. The injected charge decreases with time. Figure 5-3 (b) and Figure 5-3 (c) show the decay results of space charge for one-layer PB with 20°C and 40°C temperature gradients. It can be seen that the decay is fast during the first five minutes, followed by a slow decay. The charge dissipation rate with a temperature gradient is higher compared to that at ambient temperature. The magnitude of the cathode charge peak decreases from 3 C/m^3 to 1 C/m^3 at a 40°C temperature gradient, compared to 1 C/m^3 to 0.5 C/m^3 at ambient temperature. Figure 5-3 (d) shows the decay results of space charge for one-layer PB with a -20°C temperature gradient. The magnitude of the negative peak with a -20°C temperature is higher compared to that at ambient temperature, which is resulted from the high temperature of the bottom electrode. The charges also dissipate faster at temperature gradient compared to that at ambient temperature.

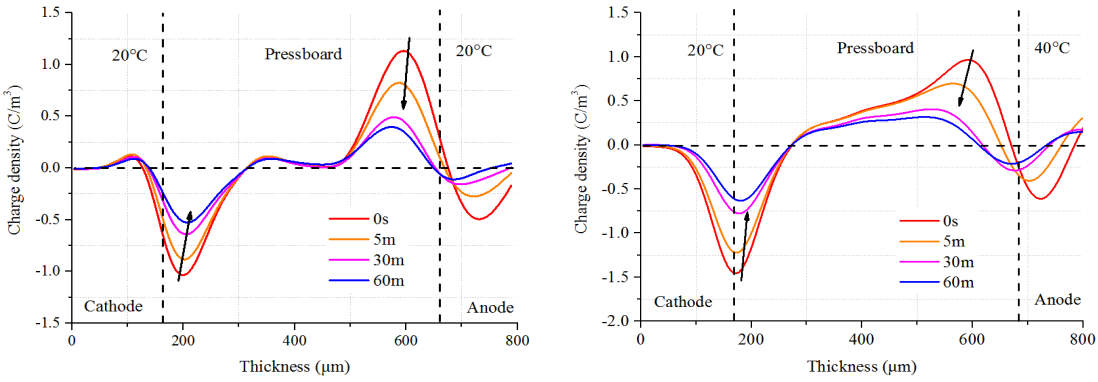

(a) AT

(b) 20 °C TG

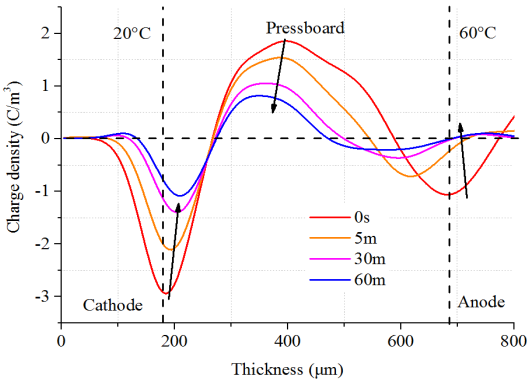

(c) 40 °C TG

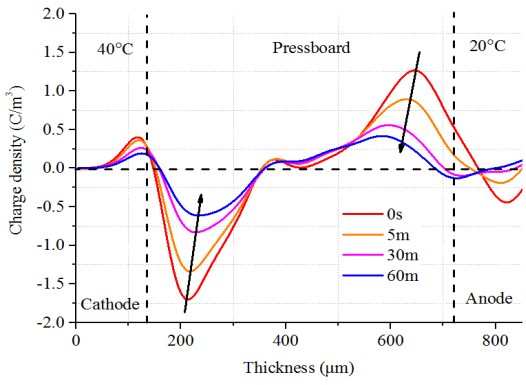

(d) -20 °C TG

Figure 5-3: Decay result of space charge in one layer of oil-impregnated PB.

The charge amount $q(t)$ in the sample can also be calculated from equation (5-1) based on the space charge results:

$$q(t) = \int_0^d |\rho(x,t)|Sdx \tag{5-1}$$

where d is the sample thickness, S is the area of the electrode.

Figure 5-4 shows absolute charge amount in one layer of oil-impregnated PB under 10 kV/mm under a temperature gradient. It shows that the charge amount increases from 40 nC to 60 nC with an increased temperature gradient from 0 °C to 40 °C.

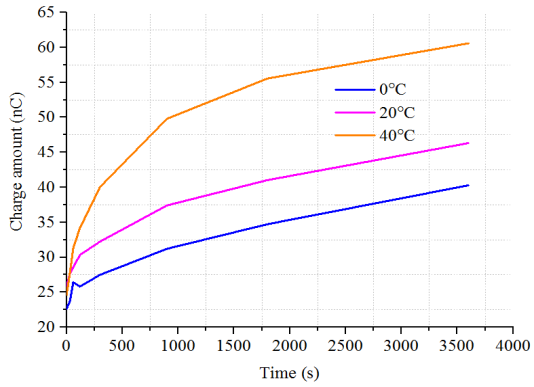

Figure 5-4: Charge amount in one layer of oil-impregnated PB under 10 kV/mm.

5.1.2 Electric field distribution

The existence of the space charge distorts the local electric field distribution in the bulk of insulation materials. The electric field can be calculated from the space charge results, based on equation (5-2) below, where $\rho(x)$ is the charge density, ε_0 is the vacuum permittivity, ε_r is the relative permittivity, and d is sample thickness. Figure 5-5 (a) shows the electric field of one-layer PB at ambient temperature. The homocharge injection leads to electric field enhancement in the bulk of insulation materials. Figure 5-5 (b) and Figure 5-5 (c) show the electric field for one-layer PB with 20°C and 40°C temperature gradient, respectively. The higher magnitude of the positive charge, injected from the high temperature anode, leads to a severe electric field enhancement in the sample. Figure 5-5 (d) shows the electric field of one-layer PB with a -20°C temperature gradient. The maximum electric field occurs at the cathode, with a similar maximum electric field compared to that with a 20°C temperature gradient.

$$\mathrm{E(x)} = \int_0^d \frac{\rho(x)}{\varepsilon_0 \varepsilon_r} dx \;\; (0 \le x \le d) \tag{5-2}$$

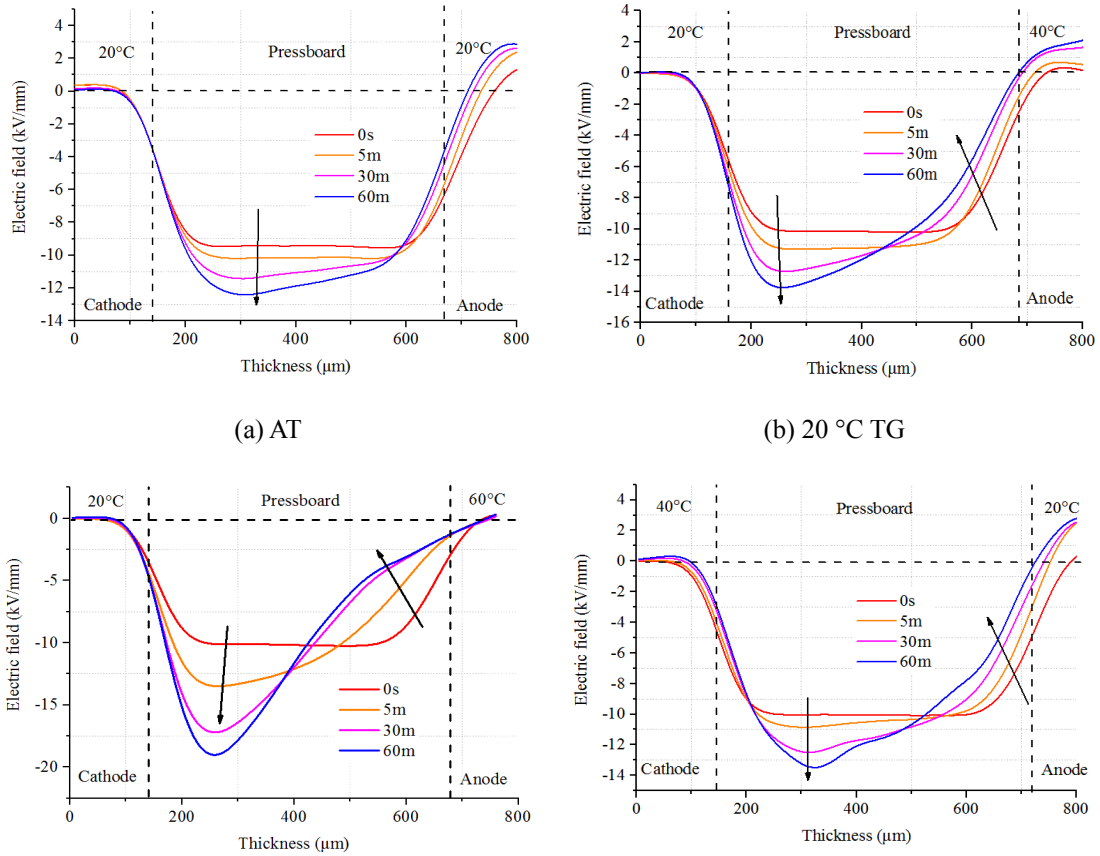

(a) AT

(b) 20 °C TG

(c) 40 °C TG

(d) -20 °C TG

Figure 5-5: The electric field in one layer of oil-impregnated PB under 10 kV/mm.

The electric field distortion factor is calculated by equation (5-3), where $E_{\max}$and E_{av} represent the maximum and average electric field, respectively. The calculation results are shown in Figure 5-6, where it can be seen that the temperature gradient severely affects the maximum electric field, and the increase of temperature gradient leads to an increase in the electric field enhancement. For both the -20°C and 20°C temperature gradients, a similar maximum electric field enhancement is observed.

$$\Delta \mathrm{E} = \frac{E_{\max} - E_{\mathrm{av}}}{E_{\mathrm{av}}} \times 100\% \tag{5-3}$$

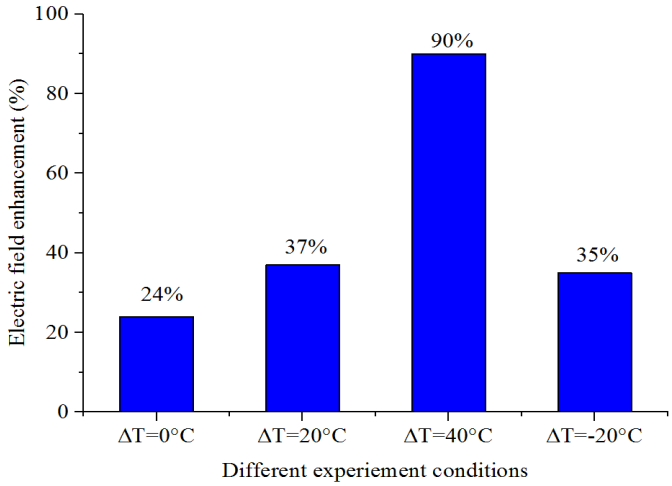

Figure 5-6: Electric field enhancement in one-layer PB for different conditions.

5.1.3 Discussion

Comparing Figure 5-2 (a) and Figure 5-2 (b), it can be seen that a significant amount of positive charge has been injected from the high temperature electrode. Several reasons may account for this phenomenon. The space charge injection is related to the threshold electric field; below the threshold, a lower amount of charge is trapped within the insulation materials (Ohmic behaviour) [54]. The threshold of charge accumulation coincides with the occurrence of the transition from Ohmic behaviour to space charge limited current (SCLC) conduction [54]. The threshold is highly dependent on the electrode temperature; the higher temperature reduces the threshold field and facilitates the charge injection [54][55].

The increased temperature increases the mobility of charge carriers. The electrons have higher mobility compared to positive charge carriers at ambient temperature [82]. However, the high temperature of the anode enhances the positive charge carrier mobility, leading to a more positive charge migration towards the bottom electrode. The space charge formation correlates with the injected and extracted charge. Due to a large amount of positive charge injected from the high temperature anode, and a small amount of charge extracted at the low temperature cathode, a large amount of space charge can be trapped within the bulk of insulation materials.

There is some negative charge near the anode in the decay result shown in Figure 5-3. Three reasons account for this phenomenon. Firstly, it is related to the induced charge due to homocharge injection in the one-layer PB. Secondly, it is related to the homocharge injection within the one-layer PB. The decay result shows the relaxation of the space charge in the PB after the voltage is removed. The decay result at 0s can be calculated through the subtraction of the steady state space charge from the referenced transient charge density. The homocharge injection occurs in the PB

and leads to the positive charge's peak movement towards the bulk of materials, resulting in the negative polarity in the charge density formation near the anode in the decay result. Thirdly, the phenomenon may be generated as a result of the acoustic wave reflection at the interface between the semiconductor materials and the PB. The acoustic impedance mismatch of the two materials may contribute to the acoustic wave reflection at the interface between the semiconductor and the PB, leading to the formation of the negative polarity of the charge density near the anode in decay result. Some negative charge near the anode also affects the relevant electric field distribution, based on the Poisson equation.

5.2 Space charge behaviour of two-layer oil and PB

Figure 5-7 shows a schematic diagram for investigating the space charge of two-layer oil and PB. Using the purposed built PEA system, a groove was created on the surface of the aluminium ground electrode. The circular groove was 5 mm in depth and 15 cm in diameter. The samples comprised two-layer oil and PB. A PTFE spacer was modified with a circular hole at the centre to produce an oil gap. The oil thickness was determined by the thickness of the PTFE spacer. The PB was placed on the top of the PTFE spacer. After placing the electrode on the sample, fixed pressure was applied to the electrode to maintain sufficient contact between the electrode and samples.

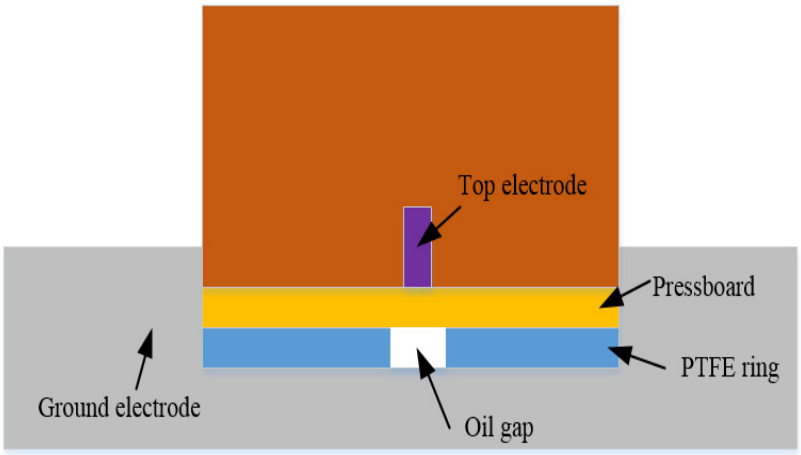

Figure 5-7: A schematic diagram of sample consisting of two-layer oil and PB.

5.2.1 Space charge behaviour

Figure 5-8 (a) shows the space charge of two layered sample consisting of 0.5 mm oil and 0.5 mm oil-impregnated PB under 10 kV/mm. Homocharge injection is obvious from two electrodes. The injected positive charges accumulate adjacent to the anode. Moreover, the negative charge migrates across the oil layer and accumulates at the oil and PB interface, leading to a reduction

of electric field in oil, and an increase electric field in PB.

Figure 5-8 (b) shows the space charge with a 40°C temperature gradient under 10 kV/mm. A significant amount of the positive charge is injected from the high temperature anode. The electric field of the oil increases over time with a temperature gradient, which is the opposite trend compared to the results shown in Figure 5-8 (a).

Figure 5-9 shows the space charge profiles with a -20 °C temperature gradient. Homocharge injection is obvious for one-layer PB, particularly for electrons injected from the cathode due to the higher temperature. Comparing Figure 5-9 (a) and Figure 5-8 (a), it can be seen that the higher magnitude of the negative charge accumulated at the oil and PB interface, meaning the electric field in the PB is enhanced.

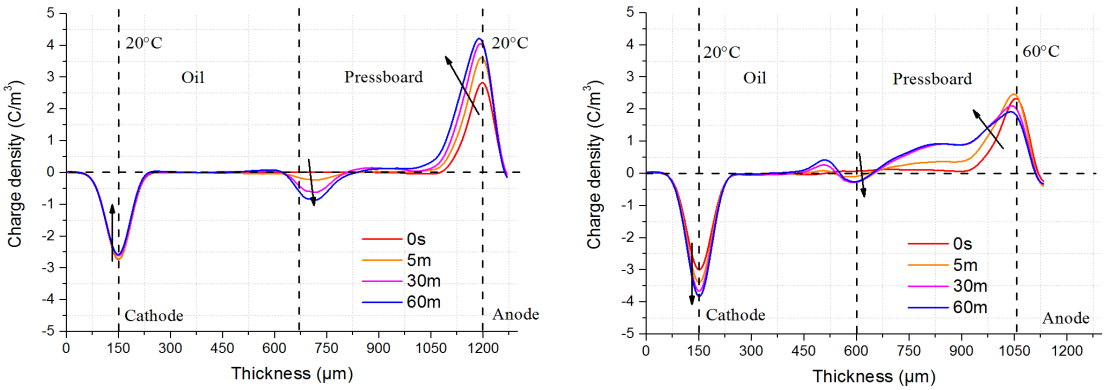

(a) AT (b) 40 °C TG

Figure 5-8: Space charge of two layers of oil and PB under 10 kV/mm.

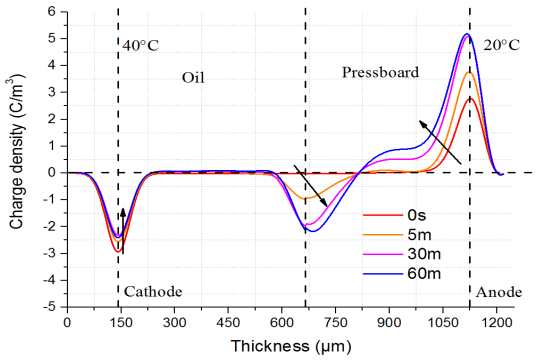

Figure 5-9: Space charge for two layers of oil and PB at a -20 °C temperature gradient under 10 kV/mm.

Figure 5-10 shows the absolute charge amount for two layers of oil and PB under 10 kV/mm. The charge amount increases with an increased temperature gradient from 0 °C to 20 °C. However, the absolute charge amount decreases with an increased temperature gradient from 20 °C to 40 °C

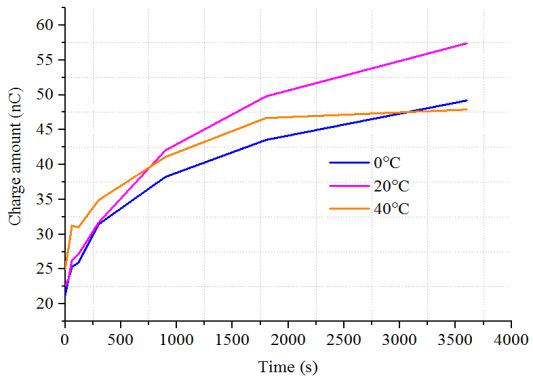

Figure 5-10: Charge amount in two layers oil and PB under 10 kV/mm.

5.2.2 Electric field distribution

Figure 5-11 (a) shows the electric field distribution across oil and PB at ambient temperature. With the longer voltage application time, the electric field in the oil decreases, while the electric field in the PB increases.

Figure 5-11 (b) shows the electric field distribution in oil and PB with a 40°C temperature gradient. A significant amount of positive charge is injected from the high temperature anode, leading to electric field enhancement in the oil. The lower interfacial charge results in a lower electric field enhancement in the PB, while the electric field close to the anode decreases.

Figure 5-12 shows the electric field of two-layer oil and PB at a -20 °C temperature gradient. The homocharge injection is obvious, particularly for electrons, leading to the electric field decreasing in the oil and increasing in the PB.

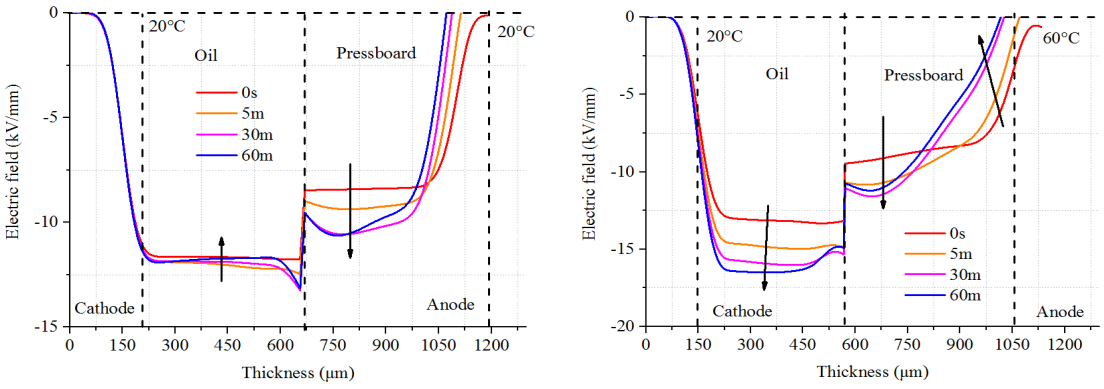

(a) AT (b) 40°C TG

Figure 5-11: Electric field of two layers of oil and PB under 10 kV/mm.

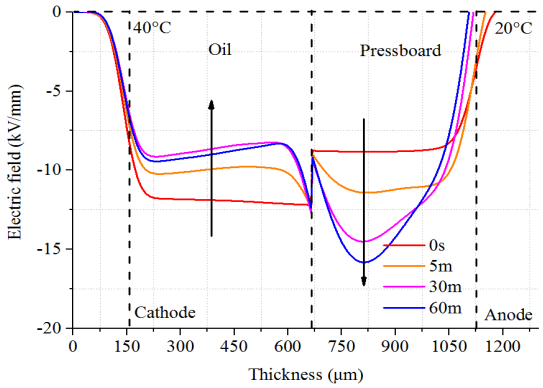

Figure 5-12: Electric field of two layers of oil and PB with a -20°C temperature gradient under 10 kV/mm.

The maximum electric field distortion factor is summarised in Figure 5-13 for two layers of oil and PB. It shows that the rise in temperature gradient increases the maximum electric field enhancement of two-layer oil and PB samples.

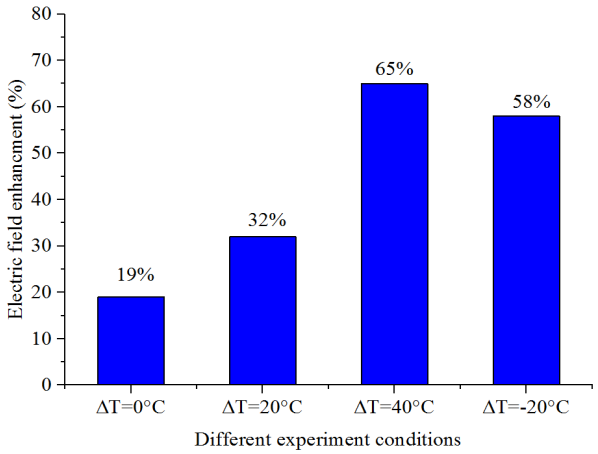

Figure 5-13: Electric field enhancement of two-layer oil and PB for different conditions.

5.2.3 Discussion

When comparing Figure 5-8 (a) and Figure 5-8 (b), it can be seen that the lower negative interface charge at the two-layer oil and PB interface is a significant feature with a temperature gradient. Several reasons may account for this phenomenon.

The interface for the oil and PB can be regarded as a barrier for the charge movement. At ambient temperature, the polarity of the interfacial charge is negative, due to the higher conductivity of the oil compared to the PB [34]. However, with a temperature gradient, the increase in temperature decreases the threshold field and increases charge carrier mobility, which facilitates positive

charge injection from the high temperature anode [83]. A large amount of positive charge injected from the high temperature electrode can neutralise the negative charge at the interface, leading to a decrease in the negative interface charge density. It can also contributes to the decreases of charge amount under an increased temperature gradient to 40 °C shown in Figure 5-10.

When the bottom electrode becomes the high temperature electrode as shown in Figure 5-9, significant amount of the charge was injected from the bottom electrode. The observed phenomenon can be explained for the following reasons.

The temperature decreases the threshold field and increases charge carrier mobility, which facilitates larger negative charge formation at the interface, as shown in Figure 5-9. The mobility of the electrons is higher compared to positive charges at ambient temperature [82]; Moreover, with the temperature gradient while the high temperature at the bottom electrode, the mobility of the electrons is further accelerated, which facilitates the negative charge migration across the oil and accumulation at the interface.

Following the comparison of Figure 5-11 (a) and Figure 5-11 (b), it can be seen that the electric field of the oil layer increases with the temperature gradient, while decreasing at ambient temperature. At ambient temperature, the negative interfacial charge migrates to the interface and decreases the electric field in the oil gap. However, with a temperature gradient, a large positive charge injection leads to electric field enhancement in the oil gap.

5.3 The space charge behaviour of three-layer PB, oil and PB

5.3.1 Space charge behaviour

Figure 5-14 shows a schematic diagram of the sample consisting of PB oil and PB. After placing the 0.5 mm PB on the ground electrode, an oil gap is formed by a PTFE spacer, with a thickness of 0.5 mm; another 0.5 mm PB is placed on the top of the PTFE spacer. Sufficient pressure is applied to maintain contact between the electrode and samples.

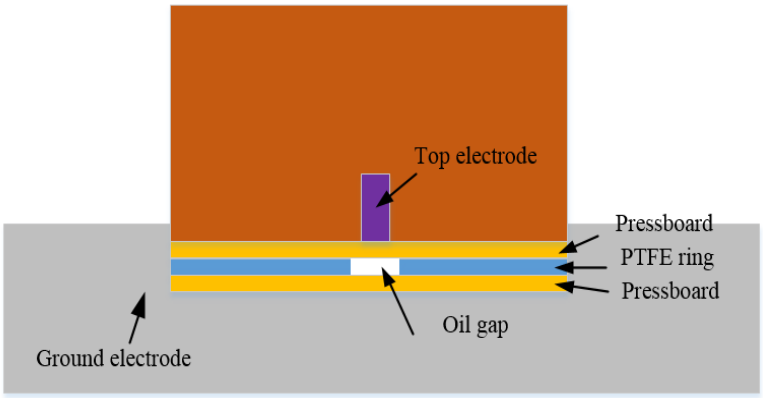

Figure 5-14: A schematic diagram of sample consisting of three-layer PB oil and PB.

Figure 5-15 (a) illustrates the space charge in the sample, with an external electric field of 10 kV/mm at ambient temperature. Homocharge injection is obvious from both electrodes, which leads to an opposite polarity of charge accumulation at both interfaces, and their magnitude increases over time.

With a 20°C temperature gradient as shown in Figure 5-15 (b), rather than a large decrease in the cathode peak at ambient temperature, the space charge with a temperature gradient on the cathode experiences a slight decrease from 2.7 C/m^3 to 2.4 C/m^3, but with an obvious negative charge injection from the cathode. Moreover, there is a small decrease from 1.7 C/m^3 to 1.3 C/m^3 in the charge near the anode over time, as opposed to the significant increase from 1.7 C/m^3 to 2.7 C/m^3 in charge near the anode shown in Figure 5-15 (a). In addition, the larger positive charge accumulates at the first layer interface, the lower the space charge accumulates at the second layer interface, as shown in Figure 5-15 (b), compared to Figure 5-15 (a).

Figure 5-16 shows the space charge density with a -20 °C temperature gradient. A large amount of negative charge is injected from the cathode due to its higher temperature. Moreover, a higher magnitude of negative charge accumulates at the second layer interface. When comparing Figure 5-16 and Figure 5-15 (a), it can be seen that more positive charge is injected from the anode.

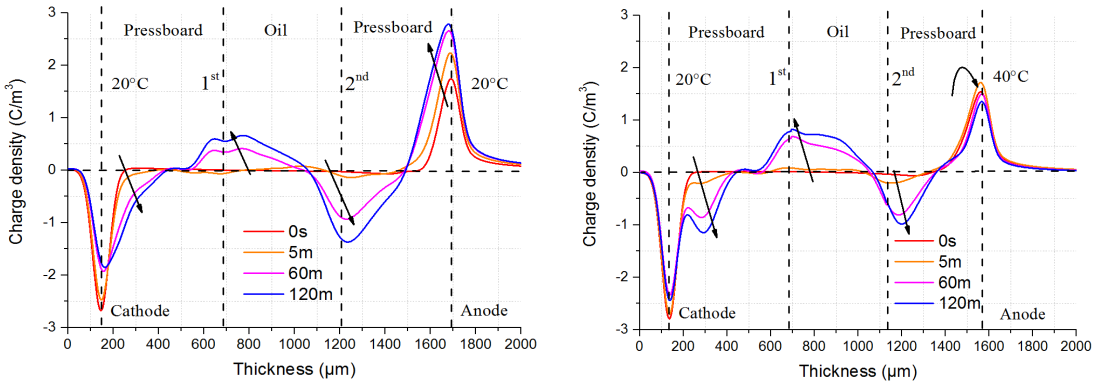

(a) AT (b) 20 TG

Figure 5-15: Space charge of three layers of PB oil and PB (PB+oil+PB) under 10 kV/mm.

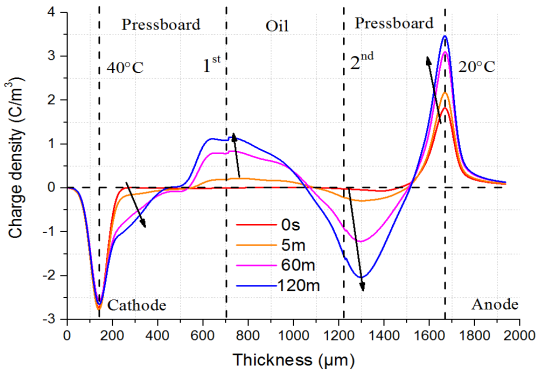

Figure 5-16: Space charge of three layers of PB+oil+PB at a -20°C temperature gradient under 10 kV/mm.

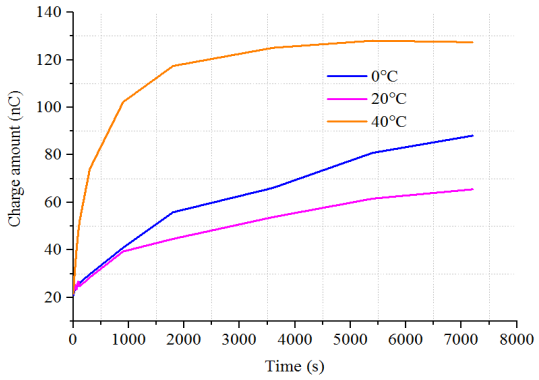

Figure 5-17: Charge amount in three layers of PB+oil+PB under 10 kV/mm.

Figure 5-17 shows the absolute charge amount of three layers PB+oil+PB under 10 kV/mm. With an increased temperature gradient, the charge amount decreases with an increased temperature gradient from 0 °C to 20 °C. However, there is a significant increase of charge amount to 128 nC with an increased temperature gradient from 20 °C to 40 °C.

Figure 5-18 (a) and Figure 5-18 (b) show the decaying process of the space charge at ambient temperature and with a 20°C temperature gradient. At the ambient temperature in Figure 5-18 (a), the space charge decays slowly over time. The magnitude of charge density in second layer interface is higher compared to the first layer. Moreover, the decrease rate of charge at the first interface layer is quite slow. The magnitude of the first interface charge stays around 0.75 C/m^3.

With a 20 °C temperature gradient in Figure 5-18 (b), rather than a slight decrease in the first layer's interface charge, as in Figure 5-18 (a), there is a slight increase in the first interface charge density. Moreover, the rapid decrease of the magnitude of the anode occurs with a 20°C temperature gradient.

Figure 5-19 shows the space charge decay process with a -20°C temperature gradient. The second layer magnitude of the interface charge density 2 C/m^3 is higher than in the first layer 1.15 C/m^3. The dissipation rate of the interfacial charge is faster compared to Figure 5-18 (a), which dissipates from 2 C/m^3 to 1.56 C/m^3 of the 2nd interface for one hour decay time.

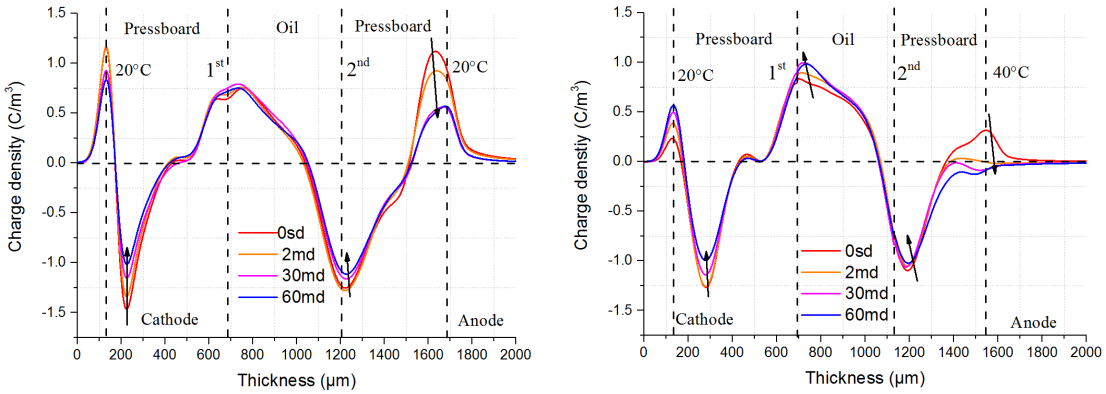

(a) AT (b) 20 °C TG

Figure 5-18: Charge decay process of three layers: PB+oil+PB.

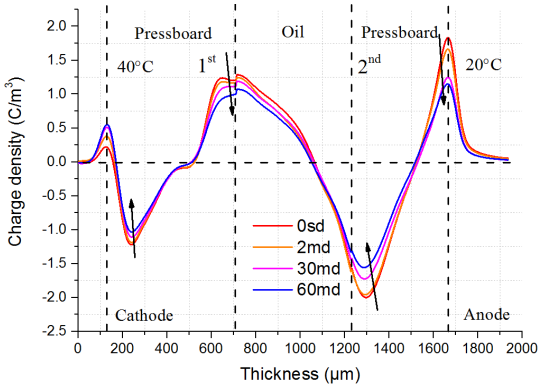

Figure 5-19: Charge decay process of three layers: PB+oil+PB, at a -20 °C TG.

5.3.2 Electric field distribution

Figure 5-20 (a) shows the electric field of multilayers PB+oil+PB at ambient temperature. The maximum electric field occurs in the PB near the anode. This is due to the higher mobility of electrons compared to positive charge carriers at ambient temperature [82]. A larger negative interfacial charge1.36 C/m^3 at the 2nd interface compared to 0.64 C/m^3 at the 1st interface is shown in Figure 5-15 (a).

Figure 5-20 (b) is the electric field of multilayers PB+oil+PB at a 20°C temperature gradient. Compared to Figure 5-20 (a), the maximum electric field occurs at the 1st interface layer between oil and PB near the cathode. This effect can be described as field migration at the temperature gradient [10], which means the maximum electric field shifts from the pressboard near the anode under ambient temperature to the 1st interface between oil and PB near cathode under the temperature gradient.

Figure 5-21 shows the electric field distribution with a -20°C temperature gradient. The high

temperature is able to decrease the threshold and facilitate the negative charge injection. Moreover, the high temperature of the bottom electrode is able to enhance charge mobility in the layer close to it and facilitates negative charge accumulation at the second interface, leading to the increased electric field near the anode.

The maximum electric field is summarised in Figure 5-22. It shows the maximum electric field increases alongside the increase in temperature gradient in the three-layer samples. The maximum electric field enhancement of three layers at a 20°C and -20°C temperature gradient is similar.

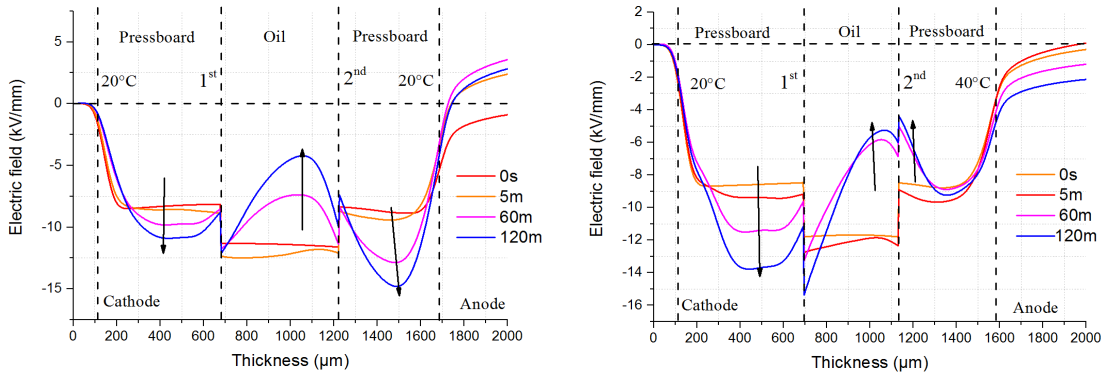

(a) AT (b) 20 °C TG

Figure 5-20: The electric field distribution of three layers PB+oil+PB under 10 kV/mm.

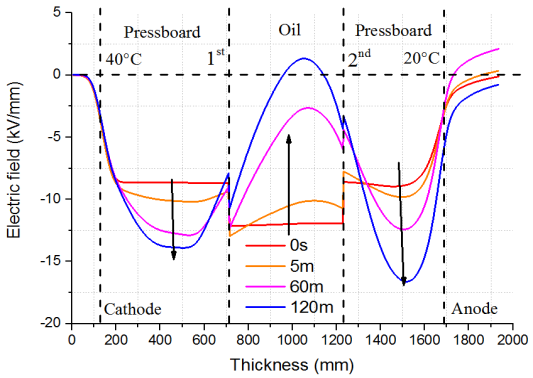

Figure 5-21: The electric field distribution of three layers PB+oil+PB with a -20 °C temperature gradient under 10 kV/mm.

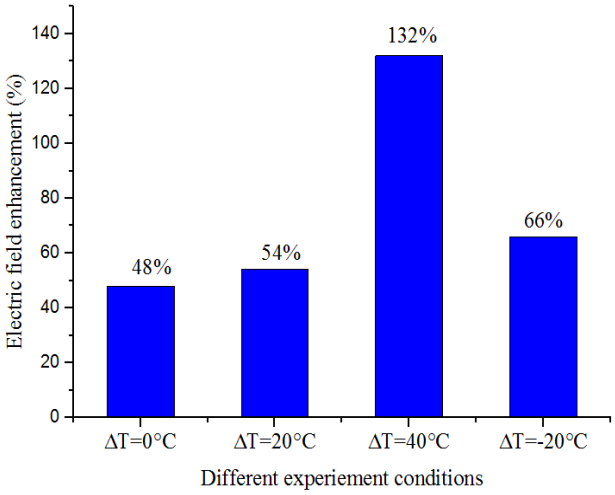

Figure 5-22: Electric field enhancement of three layers PB+oil+PB sample under different conditions.

5.3.3 Discussion

In Figure 5-15 (a), the polarities at oil and pressboard interfaces are different. Several reasons can contribute to the observed phenomenon. Firstly, the polarity of interfacial charge density satisfies the Maxwell-Wagner theory, which leads to an increase in the electric field within the PB, and a decrease in the electric field of the oil. Secondly, the opposite polarity of the interfacial charge is related to conductivity. The charge is able to easily migrate from the PB to the oil due to the higher conductivity of the oil. Thirdly, the opposite polarity of the interfacial charge density is correlated with the ionisation of the oil [84].

Figure 5-15 (a) shows the different interfacial charge densities at ambient temperature, where the magnitude of the second layer negative interfacial charge 1.5 C/m^3 is higher compared to the first positive interface charge density 0.5 C/m^3. This occurs because of the higher mobility of electrons compared to positive charge carriers, giving rise to a higher negative charge accumulation at the second layer interface.

Figure 5-15 (b) shows the space charge density of multilayers PB+oil+PB with a 20 °C temperature gradient. The increase in the first positive interfacial charge density, the decrease in the second negative interfacial charge in Figure 5-15 (b) compared to Figure 5-15 (a), and the negative charge packet near the cathode can be explained based on the following reasons.

The increase in the first interfacial positive charge is related to the decreased threshold field of charge injection. The threshold field of charge injection is dependent on the temperature of the electrode; the high temperature of the electrode can promote the charge injection [55].

The increase in the first layer positive interfacial charge density is also correlated with the injected

and extracted charge [66]. With the temperature gradient, the high temperature of the anode can enhance the mobility of positive charge carriers, leading to the increase in the first layer positive interfacial charge density. Moreover, considering the low extraction rate of charge carriers due to the low temperature near the cathode [85], a large amount of positive charge accumulates at the first layer interface.

The decrease in the second layer negative interface charge in Figure 5-15 (b) compared to Figure 5-15 (a), is mainly the result of a large positive charge injection. The high temperature of the anode can decrease the threshold field and increase charge mobility; thus, more positive charge can neutralise the second layer negative interface charge.

With an increased temperature gradient, the amount of the charge increases in three layer PB+oil+PB is shown in Figure 5-17. It is the opposite trend compared to the charge amount versus temperature gradient shown in Figure 5-10. This is mainly attributed to the different charge behaviour in oil and pressboard, separately. The charge can easily migrate across the oil while it slowly injects into the pressboard under the external electric field. For two layers oil and PB, the negative interfacial charge can be neutralized due to the significant positive charge injection from the high temperature anode, leading to the decrease of charge amount in two layers samples. However, for three layers PB+oil+PB, the high temperature promotes the charge injection and leads to the electric field enhance near the cathode, which could further facilities the negative charge injection. The negative charge slowly injected into the pressboard compared to the rapid migration across the oil in two layers samples. Large amount of the charge trapped in the pressboard leads to the increased charge amount with an increased temperature gradient for three layers PB+oil+PB.

Figure 5-16 shows the space charge profiles of multilayers PB+oil+PB under a -20°C temperature gradient. The increase of the magnitude of the second layer negative interface charge density is obvious. Considering the decrease in the threshold and the increase of negative charge carriers' mobility, these contribute to the formation of space charge density at the second layer oil PB interface under a -20 °C temperature gradient.

Figure 5-20 (a) illustrates the electric field of multilayers PB+oil+PB at ambient temperature. The maximum electric field occurs at the PB near the anode. This is due to the higher mobility of electrons compared to positive charge carriers at ambient temperature [82]. The higher negative interfacial charge is able to accumulate at the second layer interface.

Figure 5-20 (b) exhibits the electric field of multilayers PB+oil+PB at a 20°C temperature gradient. Compared to Figure 5-20 (a), the maximum electric field occurs at the first layer interface near the cathode in Figure 5-20 (b). This effect can be described as field migration with the specific

temperature gradient [10]. Several reasons can account for the presence of the electric field gradient at the temperature gradient.

The electric field is determined by the charge distribution, based on the Poisson equation, given in equation (5-2). At a 20 °C temperature gradient, the increase in the first layer positive interface charge leads to a slight decrease in the electric field near the cathode, as shown in Figure 5-20 (b). Moreover, a large amount of positive charge from the high temperature electrode neutralises the negative charge at the second layer. Therefore, the electric field gradient existed across the insulation materials, with the maximum electric field occurring near the cathode. Moreover, based on the Richardson-Schottky law [86], the higher electric field near the cathode can further enhance the negative charge injection, which facilitates negative charge packet formation near the cathode shown in Figure 5-15 (b).

5.4 Summary

The space charge behaviour of oil and PB under a DC electric field is investigated based on a purpose-built new PEA system. The influence of temperature gradient and multilayers on the behaviour of space charge in oil and PB is investigated. The experiment results show that charge behaviour with the temperature gradient differs compared to that at ambient temperature. For one-layer PB, a large amount of positive charge is injected, due to the high temperature of the anode. For two-layer sample consisting of oil and PB, with 20°C at the bottom electrode, the electric field in the oil increases with temperature gradient, and decreases at ambient temperature. For three layers, with 20°C at the bottom electrode, the maximum electric field occurs near the cathode with a temperature gradient, while it occurs near the anode at ambient temperature. The maximum electric enhancement is also summarised for different sample configurations, which reveals that higher temperature gradients leads to higher electric field enhancement. The slow dissipation rate of the charge, particularly for three layer samples, may lead to severe electric field enhancement following the polarity reversal operation. This will be further investigated in the next chapter.

Chapter 6 The polarity reversal effect on space charge behaviour under a temperature gradient

A Polarity reversal (PR) operation can affect the stability of converter transformers due to sudden electric field enhancement within the oil. With the purpose of studying the transient electric field of oil after PR operation, the pulsed electroacoustic (PEA) method will be utilized to measure the space charge in two layered sample consisting of oil and PB during PR operation. This chapter firstly reviews previous PR research and introduces the motivations for this research. The influential factors that affect the electric field after PR, such as temperature gradient, multilayers samples, different PR time, and voltage polarity are investigated. The dynamics of space charge in the oil and PB under these influential factors are presented and explained.

6.1 Motivations

A converter transformer is one of the most important devices in the HVDC power transmission system. The valve side winding will withstand not only combined DC and AC voltage but also the different polarities of voltage in case of power reversal based on the current source converter (CSC) technology [2]. During PR operation, the space charges cannot rapidly dissipate but create their own electric field superposed with a newly generated transient capacitive electric field after PR. Consequently, the electric field in the oil gap is severely enhanced after PR operation, which could eventually affect the safe and reliable operation of converter transformers [2] [12]. PR operation is regarded as a routine test to verify the insulation property of converter transformers. Based on the PR standard [57], key factors affecting the electric field after PR operation includes voltage magnitude, polarity, voltage application time, PR duration, and PR counts. The PR standard declares [59] that 90 minutes of voltage application time is capable of achieving the steady state of the electric field distribution of oil and PB insulation. Moreover, PR operation is defined as a double PR test with both PR operation time taking place within two minutes [57] .

Several researchers have investigated influential factors that affect the electric field after PR operation. Qi [2] investigated different PR duration on the transient electric field of oil and PB based on the Kerr effect method. It was found that the impact of PR operation time upon the transient electric field of oil depends on the ratio of PR duration (Tr) and the time constant for charge accumulation and dissipation [2]. When the PR time, Tr, is longer or close to the time constant for charge accumulation and dissipation, PR time has a significant influence on the electric field in oil after PR operation. Otherwise, the PR time, Tr, has less impact on the electric field in oil after PR operation. Hao [87] investigated the ageing effect on the electric field of oil and PB after the PR operation. The results indicate that the longer PR duration time could

significantly decrease the transient electric field of aged samples compared to fresh ones. This is due to the smaller time constant of the aged samples compared to PR operation time. Zhou [61] investigated the voltage polarity effect on the charge behaviours in two layers of oil-paper insulation. It was found that different electrode materials have a significant effect on the space charge behaviour under different polarities of applied voltages. This is due to the change in work functions of different materials [61]. Okubo investigated the transient electric field in oil and PB after PR, based on the simulation. The electric field in oil is enhanced due to the residual charge distribution superposed by the transient capacitive electric field after PR operation [12]. Wu and Chen [88] [56] investigated the temperature gradient effect on the transient electric field of LDPE materials after PR. The longer PR operation time could increase the electric field of LDPE after PR under the temperature gradient, which is an opposite trend compared to the electric field under the ambient temperature.

Based on the above literature review, most researchers investigated influential factors on the transient electric field after PR under ambient temperature. The temperature gradient effect on the transient electric field of oil and PB after PR is rarely investigated and results will be presented in this chapter. As the conductivity depends on the temperature and the electric field, temperature can change the conductivity ratios between the oil and the PB. To consider effect of the temperature, some researchers conducted the calculations of field studies after PR operation with various conductivity ratios of oil and PB so that the worst situations can be identified [10] [11]. When the temperature gradient is present, it can change the charge mobility and affect the space charge dynamics, which cannot be simply represented by various bulk conductivity ratios. Therefore, the temperature gradient effect on the electric field of oil and PB after PR should be carefully investigated.

The study in this chapter applied the PEA (pulsed electroacoustic method) to measure space charge dynamics in multilayers of oil and oil-impregnated PB after PR operation. Four factors will be emphasized, including temperature gradient, different voltage polarities, multilayers of oil and PB and different PR duration. The experiment methodology will be briefly described. Four different influential factors on the space charge dynamics under the PR process will be presented and explained. The maximum transient electric field in oil after PR operation will be summarised and compared.

6.2 Experiment methodology

6.2.1 The PR voltage profile

The pulsed electroacoustic (PEA) method is utilized for the space charge measurement to

investigate the temperature gradient effect on the transient electric field after PR operation. The PR voltage profile is illustrated in Figure 6-1. The voltage was acquired by an Agilent Arbitrary Function generator, which was then increased to 10 kV/mm via a high-voltage power amplifier. The voltage was applied on the upper electrode of the PEA system. The voltage application time lasted 120 minutes, longer than the standard 90 minutes [57].

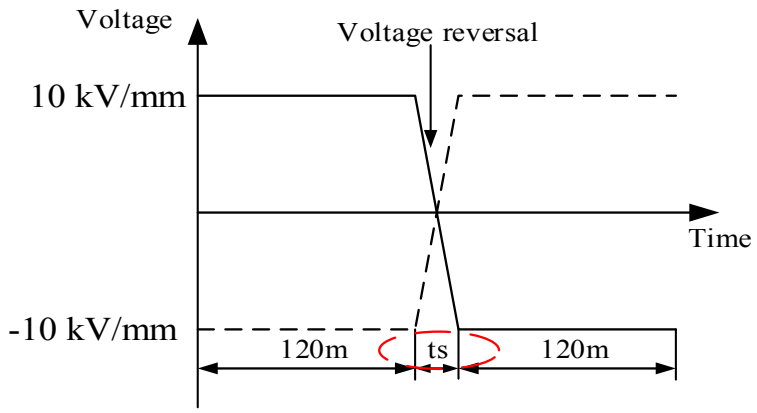

Figure 6-1: Profile of the PR voltage.

6.2.2 Experiment plan

The samples contained multilayers of oil and PB, including two layers of oil and PB (PB+oil) and three layers of PB oil and PB (PB+oil+PB). The polarity effect is considered, not only from negative (-) to positive (+) but also from positive (+) to negative (-). The different PR duration on the space charge behaviour has been investigated under at ambient temperature with different PR time of 60 s and 90 s respectively. The detailed experiment plan is exhibited in Table 6-1.

Table 6-1: Experiment plan for space charge measurement under PR operation

	Sample	Thickness (μm)	Electric field (kV/mm)	Temperature gradient (°C)	Voltage polarity	PR duration (s)
Two layers	PB+Oil	2×500	10	0, 40	(+) to (-)	60, 90
					(-) to (+)	
Three layers	PB+Oil+PB	3×500	10	0, 40	(+) to (-)	120
					(-) to (+)	

6.3 Experiment results

6.3.1 Temperature gradient effect

Figure 6-2 (a) illustrates the space charge results of 0.5 mm oil and 0.5 mm oil-impregnated PB with the PR voltage from positive (+) to negative (-) at ambient temperature. Under the positive voltage, homocharge injection leads to the positive charge accumulation near the anode, while some negative charge migrate across the oil layer, leading to the negative charge accumulation at the interface. The ionization in the oil gap also contribute to the negative charge formation at the interface [89]. The negative interfacial charge could induce positive charge on both electrode, leading to the decrease of the charge on the cathode due to the charge neutralization.

Figure 6-2 (b) shows the space charge behaviour after PR. Under the negative voltage, the previously injected positive charges near the cathode are gradually neutralized by the injected negative charges from the cathode. It is also noticed that the previous accumulated negative interfacial charges change their polarities to positive and this takes around 60 minutes. This is considered as a result of homocharge injection from the new anode. Homocharges migrate across the oil layer and neutralise the previous interfacial charge. Moreover, the positive charge at the interface will induce the negative charge on the anode, leading to the decrease of the anode peak due to charge cancellation.

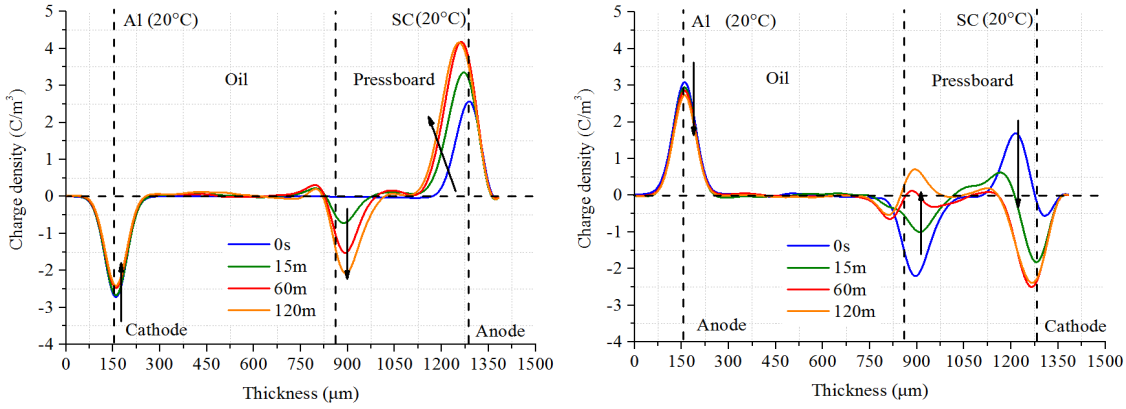

(a) Under positive (+) (b) Under negative (-)

Figure 6-2: Space charge of two layers of oil and oil-impregnated PB under the ambient temperature with the voltage reversal from positive (+) to negative (-).

Figure 6-3 (a) shows the space charge results of 0.5 mm oil and 0.5 mm oil-impregnated PB with the PR voltage from negative (+) to positive (-) with 40°C temperature gradient. A significant amount of positive charges are injected from the anode, leading to an increase in the cathode peak. The electric field in the oil increases, which is the opposite trend compared to Figure 6-2 (a). Due

to a large amount of positive charge injection, less negative interfacial charge accumulates at the oil and PB interface, which is a result of the charge neutralization at the oil and PB interface.

Figure 6-3 (b) shows the space charge after PR operation. Under negative voltage, the previous injected positive charges near the cathode are gradually neutralised by the injected negative charges from the cathode. The interfacial charge changes its polarity from negative to positive and this takes around 10 minutes. Moreover, the large amount of negative charge injection leads to the increase of the anode peak.

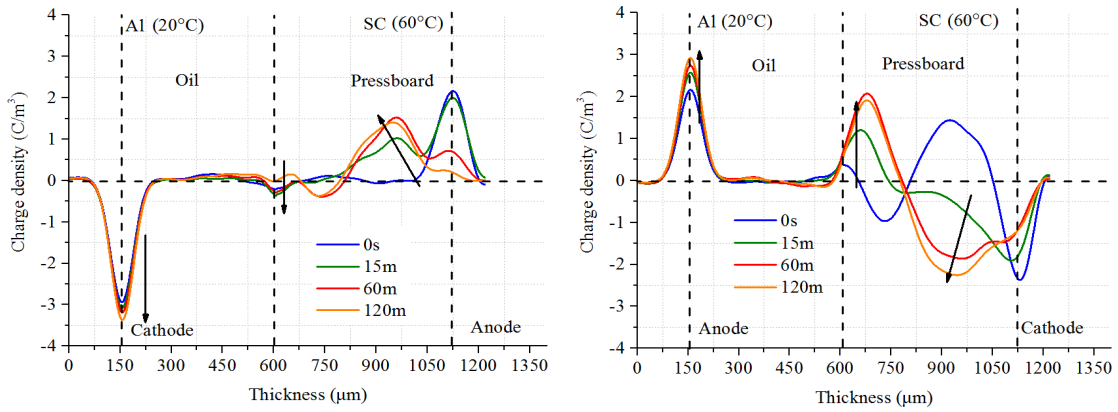

(a) Under positive (+)

(b) Under negative (-)

Figure 6-3: Space charge of two layers oil and oil-impregnated PB under the temperature gradient with voltage reversed from positive (+) to negative (-).

6.3.2 Polarity effect

Figure 6-4 (a) shows space charge results including the transient and steady state with voltage polarity reversed from negative (-) to positive (+) at ambient temperature. The 'mirror image charge' described in the literature [82] is witnessed by comparison of the steady-state space charge under the voltage with different polarities. Figure 6-4 (b) illustrates the space charge containing the transient and steady state at ambient temperature with voltage polarity reversed from positive (+) to negative (-).

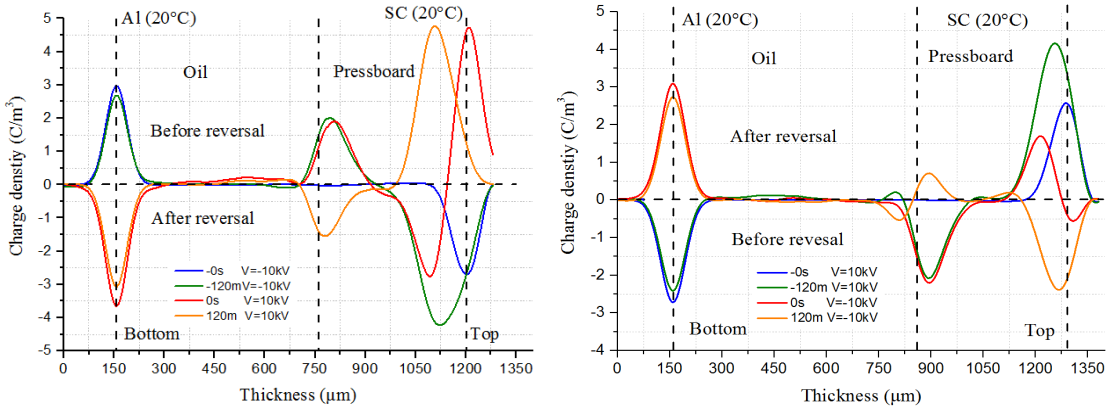

(a) From (-) to (+) (b) From (+) to (-)

Figure 6-4: Space charge of two layers of oil and oil-impregnated PB at ambient temperature with voltage of different polarities.

Figure 6-5 (a) shows the transient and steady-state space charge characteristics with the voltage PR from negative (-) to positive (+) under a 40°C temperature gradient. Compared to the results in Figure 6-4 (a), under negative voltage (-), quantities of negative charges are injected from the top electrode, leading to a significant electric field increase within the oil with a temperature gradient.

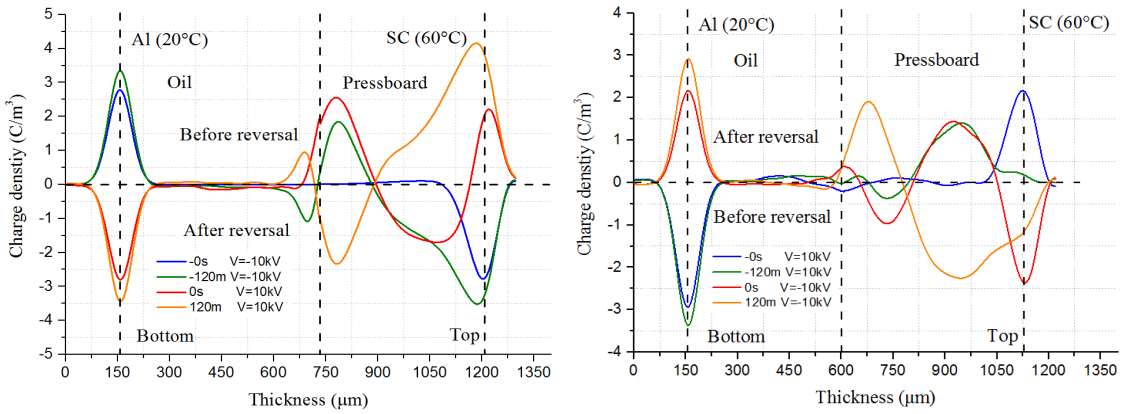

(a) From (-) to (+) (b) From (+) to (-)

Figure 6-5: Space charge of two layers of oil and oil-impregnated PB with a 40°C temperature gradient under different PR operations.

Figure 6-5 (b) represents space charge dynamics with voltage polarity reversed from positive (+) to negative (-) under a 40°C temperature gradient. It is noted that under positive (+) voltage, there are less interfacial charges at 120 minutes compared to that under positive (+) voltage at 120 minutes as shown in Figure 6-4 (b). Moreover, in Figure 6-5 (b) under negative voltage, more

negative charges are injected from the top electrode at 120 minutes, leading to a significant electric field enhancement in the oil under the temperature gradient. A 'mirror image charge' is not seen by the comparison of the steady-state space charges under a temperature gradient with the voltage polarity reversed from positive (+) to negative (-).

6.3.3 Different PR time

Figure 6-6 (a) shows the transition of the electric field of oil at different PR time of 60 s and 90 s separately with the voltage reversed from (-) to (+) under: (a) ambient temperature; and (b) a 40°C temperature gradient. Before each PR operation, the steady electric field of oil is similar, indicating the good consistency of the two tests. The different PR time effects on the electric field of oil could then be correctly reflected.

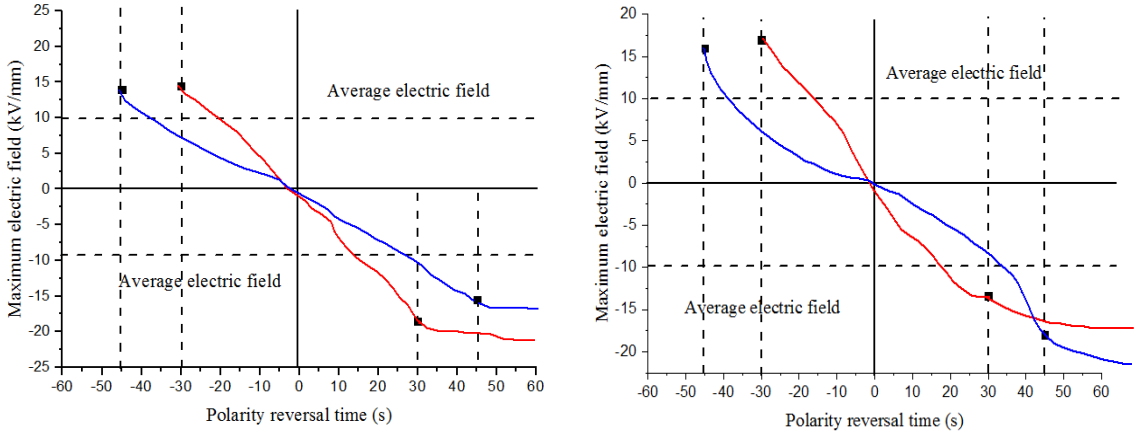

(a) At ambient temperature

(b) Under 40°C temperature gradient

Figure 6-6: The maximum electric field of oil with different PR time of 60 s and 90 s under: (a) ambient temperature; and (b) 40°C temperature gradient with the voltage reversed from negative (-) to positive (+).

Figure 6-7 shows the maximum electric field of oil after different PR time of 60 s and 90 s with the voltage reversed both from (-) to (+) and (+) to (-) at ambient temperature and with temperature gradient. At ambient temperature with the voltage reversed from (-) to (+), the maximum electric field in oil decreases from 18.5 kV/mm to 15.5 kV/mm with a longer PR time. Under the temperature gradient, the maximum electric field increases from 9 kV/mm to 9.4 kV/mm with the voltage polarity from (+) to (-) and from 13.4 kV/mm to 18 kV/mm from (-) to (+) under the temperature gradient with a longer PR time.

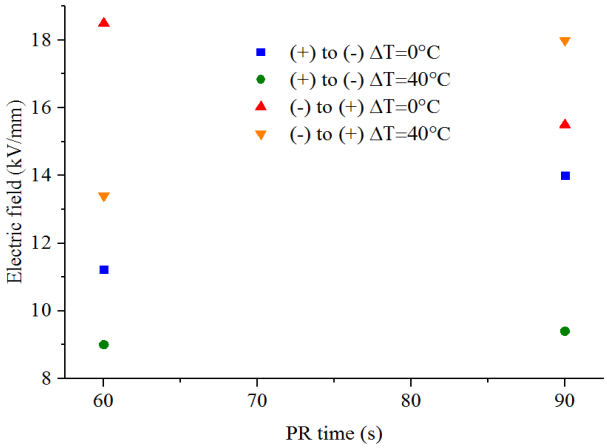

Figure 6-7: Maximum electric field of oil after different PR time of 60 s and 90 s under different experimental conditions.

6.3.4 Multilayers effect

Figure 6-8 (a) illustrates the space charge profiles of multilayers of PB oil and PB at ambient temperature with the voltage reversed from (-) to (+). At ambient temperature, homocharge injection occurs from both electrodes. The interfacial charges accumulated at the interface and their magnitudes increase with time.

Figure 6-8 (b) shows the space charge after PR operation. Due to the interfacial barrier effect, the interfacial charge has a low-charge-dissipation rate, leading to a slow decrease in the interfacial charge density.

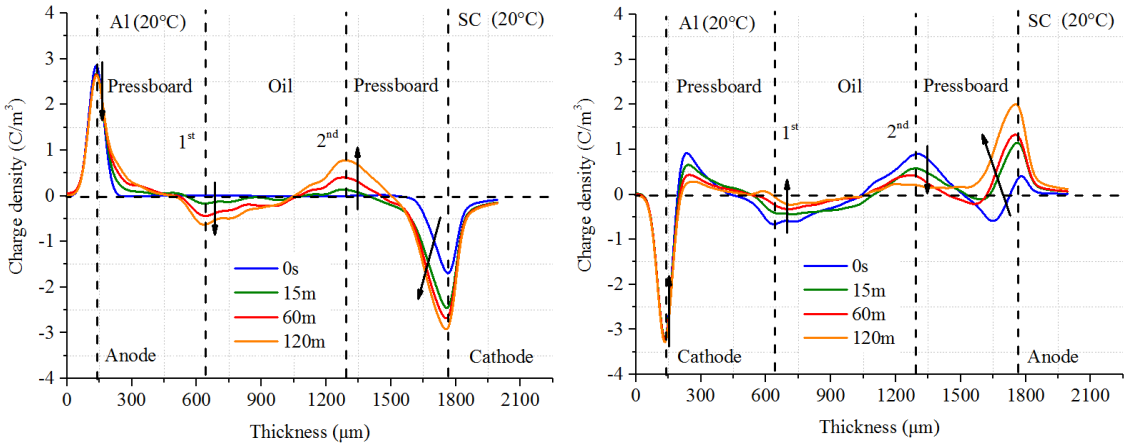

(a) Under negative (-) (b) Under positive (+)

Figure 6-8: Space charge of three layers of oil and oil-impregnated PB with ambient temperature under the voltage reversed from negative (-) to positive (+).

Figure 6-9 (a) and Figure 6-9 (b) illustrate the transient and steady-state space charge results of multilayers PB oil and PB with voltage reversed from negative (-) to positive (+) and from (+) to (-) at ambient temperature. A 'mirror image charge' is not seen in the comparison of the steady-state space charge with the voltage of different polarities under the ambient temperature.

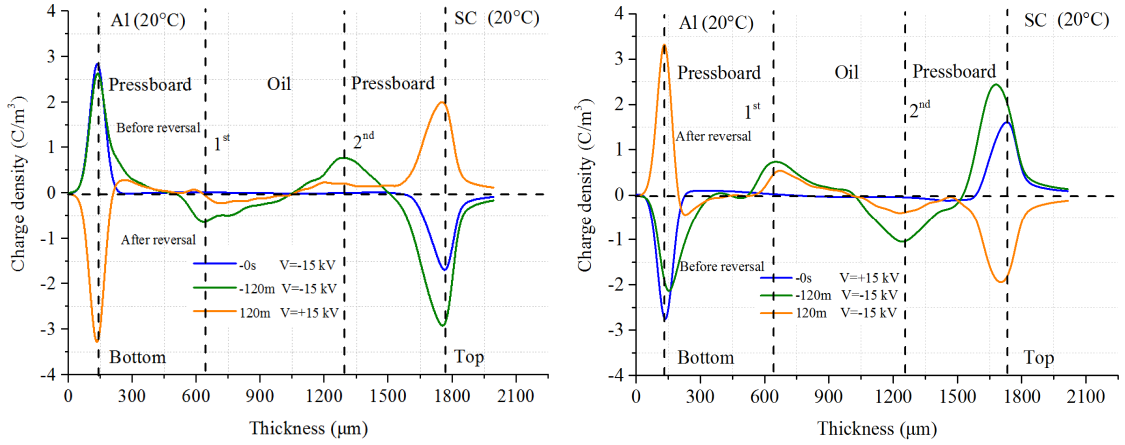

(a) From (-) to (+) (b) From (+) to (-)

Figure 6-9: Space charge of three layers of oil and oil-impregnated PB under ambient temperature during different PR operations.

Figure 6-10 shows the transient and steady-state space charge results with the voltage reversed from positive (+) to (-) under a 40°C temperature gradient. Under the 40°C temperature gradient in Figure 6-10, larger amount of positive charge accumulates at the 1st interface but lower amount of negative charge at the 2nd interface as shown in Figure 6-10. A large amount of positive charge injection leads to an increase of the cathode peak. A 'mirror image charge' can be seen with the comparison of the steady-state space charge under the voltage with different polarities as shown in Figure 6-10.

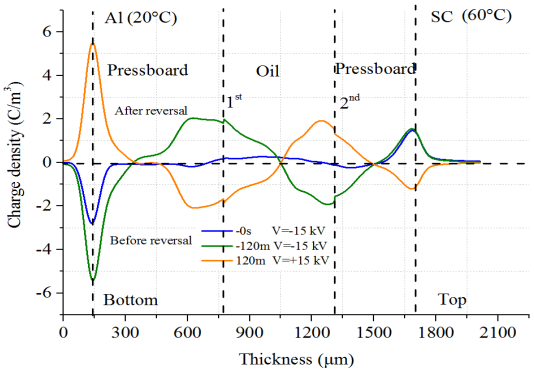

Figure 6-10: Space charge of three layers of oil and oil-impregnated PB under a 40°C temperature gradient under different PR operations from (+) to (-).

6.4 Discussion

6.4.1 Temperature gradient effect

After PR, it takes less time (around 10 minutes) for the interfacial charge to change its polarity under the temperature gradient, compared to that at ambient temperature, which takes around 60 minutes. Several reasons could account for this.

The increase in temperature enhances the mobility of space-charge carriers. After PR, the interfacial charge due to high temperature will quickly dissipate and change the polarity of the interfacial charge density.

The faster change of the interfacial charge polarity under the temperature gradient compared to at ambient temperature is correlated with a time constant based on equation (6-1).

$$\tau = \frac{d_{oil}\varepsilon_{op} + d_{op}\varepsilon_{oil}}{d_{oil}\gamma_{op} + d_{op}\gamma_{oil}} \tag{6-1}$$

The time constant is correlated of two layers of oil and PB and is dependent on the sample thickness, relative permittivity and conductivity. The high temperature increases the conductivity and reduces the time constant. It can lead to rapid accumulation and dissipation rate of the charge carrier under the temperature gradient.

There is a small amount of opposite polarity charge near the interfacial charge in the oil shown in Figure 6-5 (a) and (b). The opposite polarity in the charge near the interface is caused by the charge neutralisation at the oil and PB interface. Under a temperature gradient, the high temperature can facilitate the space charge injection, leading to a large amount of positive charge in the bulk of the PB. The oil and PB interface does not abruptly change from bulk PB to oil. The interface is a composite region, which consists of the oil and PB. The PB surface is characterised by an array of dimples; moreover, the edge of the PB is quite irregular, with protruding fibres, and is characterised by a transition region of 350 μm above the PB surface [90]. Under a positive voltage in Figure 6-5 (a), a large amount of positive charge is injected into the bulk of the PB, while the negative charge accumulates at the interface between the oil and the PB. The PEA system only detects the net charge. The neutralisation of the positive injected charge and the negative interfacial charge leads to a positive charge in the oil, which is the opposite polarity of the negative interfacial charge.

Figure 6-11 (a) shows the electric field distribution of two layers of oil and PB after PR at ambient temperature. Charge carriers with the same polarity compared to nearby electrodes are called homocharge while those with the opposite polarity with the adjacent electrodes are referred to heterocharge [36]. The homocharge injection within the oil-impregnated PB can be viewed as

heterocharge, which enhances the electric field in the vicinity of the electrode and the interface between the oil and PB. Moreover, for the oil part, the enhancement of the electric field in the oil is also correlated with the presence of the charge. The space charge injection from the cathode previously could be converted into homocharge after PR operation, leading to electric field enhancement within the oil. The electric field in the oil decreases while the electric field in the PB increases with time.

Figure 6-11 (b) illustrates the transient electric field distribution of two layers of oil and PB after PR under the 40°C temperature gradient. For the oil part, the electric field is enhanced due to the residual charge creating its own electric field superposed by a newly capacitive electric field after PR operation. For the PB, the previous homocharge injection can be viewed as heterocharge after PR operation, which enhances the electric field in the vicinity of the anode and the oil PB interface. After PR, the electric field in the oil increases due to a large amount of positive charge injection from the high temperature anode. The local electric field in the PB is enhanced and the electric field near the anode is significantly reduced under the temperature gradient.

With the comparison of Figure 6-11 (a) and Figure 6-11 (b), the electric field in the oil decreases at ambient temperature, while the electric field in the oil increases under the temperature gradient over time. Based on this, the transient electric field in the oil reaches its maximum value at ambient temperature after PR. However, the steady-state electric field in the oil reaches its maximum value under the temperature gradient after PR. Therefore, more attention should be placed on the steady-state electric field of oil after PR under the temperature gradient.

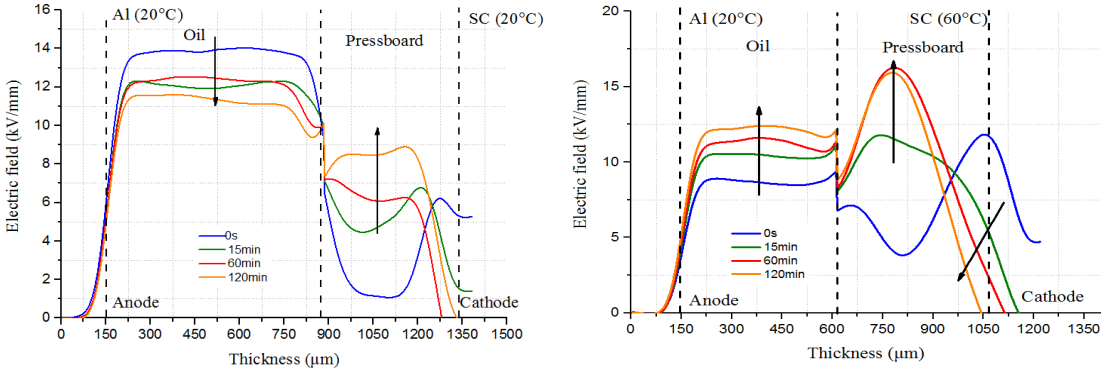

(a) Under ambient temperature (b) Under 40°C temperature gradient

Figure 6-11: Electric field of two layers of oil and oil-impregnated PB under: (a) ambient temperature; and (b) the 40°C temperature gradient after PR of 90 s under negative (-) voltage.

The local electric field enhancement in the PB is attributed to the higher magnitude of the interfacial charge density under the temperature gradient. In Figure 6-11(b), due to a large amount of negative charge injection from the high temperature cathode, the electric field increases in the oil gap, which further facilities the charge injection from the electrode into the oil. The charge

migrating across the oil layer accumulates at the interface and enhances the electric field in the PB. The local electric field enhancement in the PB cannot simply be calculated by the various conductivity ratios between the oil and PB based on the Maxwell-Wagner theory.

6.4.2 Polarity effect

The polarity of applied voltage affects the magnitude of the interfacial charge density at the interface between the oil and PB, especially under the temperature gradient. The comparison of Figure 6-3 (a) and Figure 6-3 (b) indicates that more interfacial charge accumulates at the oil and PB interface under the negative voltage compared to the positive voltage in the presence of temperature gradient. The previous experiment result indicates that holes are injected more easily compared to electrons from Al electrode [60] [91] [92], which may explain the experiment phenomena here.

However, in theory, the magnitude of the interfacial charge density should depend on the work function of electrode materials. The work function of the Al is (4.08± 0.05 eV), while the SC has a lower potential barrier compared to Al [60]. Therefore, for the bulk space charge or the polarity of the two identical materials, the interfacial charge density is determined by the voltage polarity of SC materials due to its low potential barrier. This has been verified by one or two layers of space charge results under the SC/Al electrode system [56] [61]. However, under a temperature gradient of two different dielectric layers of dielectric materials, more factors need to be considered to explain the different magnitude of the interfacial charge density with different polarities of applied voltage under a temperature gradient.

Under a temperature gradient, the magnitude of the interfacial charge density is different with different polarities of applied voltage. It is explained by the different electrons movement behaviour at the interface of oil and PB under different polarities of applied voltage. Under a positive voltage, the negative charge can hardly migrate into the PB due to the higher resistivity compared to the oil. Moreover, a large amount of space charge is injected from the anode due to the high temperature, resulting in the neutralisation of the negative interfacial charge density. However, under the negative voltage, the negative interfacial charge can easily migrate across the oil gap due to lower resistivity of the oil under the external electric field. This could result in a higher positive charge accumulation at the interface due to the electron movement from the interface. Therefore, the higher magnitude of positive charge could accumulate at the interface under the negative (-) polarity of the voltage with a temperature gradient [3].

Figure 6-12 summarises (a) the maximum electric field and (b) the electric field enhancement in the oil after PR for different experiment conditions. With the comparison of the transient electric field of oil under the temperature gradient, it shows that the electric field in the oil is more severe

with the voltage PR reversed from negative (-) to positive (+). This is because the higher magnitude of the interfacial charge density with the voltage reversed from negative (-) to (+) leads to a severe electric field enhancement within the oil after PR operation.

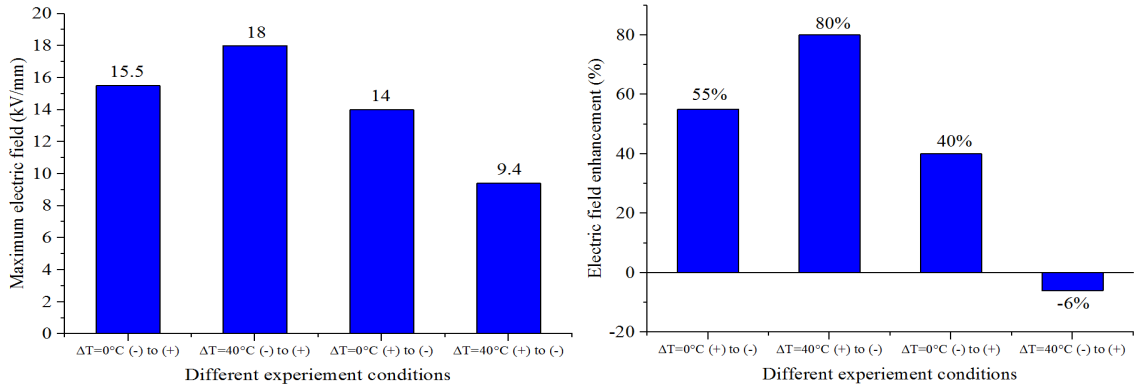

(a) (b)

Figure 6-12: The (a) maximum transient electric field and (b) electric field enhancement of oil after the PR operation in two layers oil and PB.

6.4.3 Different PR time

At ambient temperature with the voltage reversed from (-) to (+), the maximum electric field in oil decreases with the increasing length of PR time. Several reasons could account for this phenomenon.

The decrease of the maximum electric field in the oil after PR is correlated with the interfacial charge dissipation during the PR process. Figure 6-13 shows the space charge of two layers oil and oil-impregnated PB during PR from (-) to (+). The longer PR time leads to the lower interface charge that accumulates at the oil and PB interface. It results from interfacial charge dissipation or recombination between holes and electrons in insulation materials, which leads to less electric field enhancement in the oil after PR.

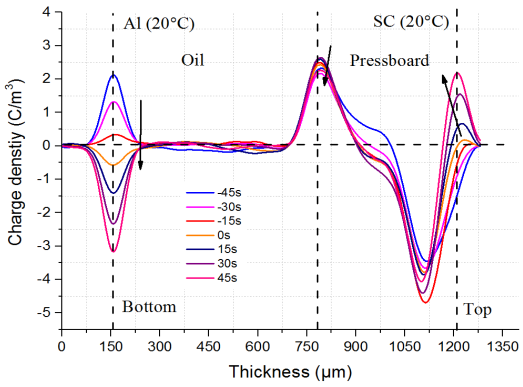

Figure 6-13: Space charge of two layers of oil and oil-impregnated PB during the polarity reversal operation from (-) to (+).

Under a temperature gradient with the voltage reversed from (-) to (+), after PR, the maximum electric field of the oil increases with the length of PR time. Several reasons could account for this phenomenon.

The maximum electric field in the oil after PR increases with the length of PR time because the interfacial charge increases during PR under a temperature gradient. Figure 6-14 shows the space charge of two layers of oil and PB during PR with the voltage reversed from (-) to (+). The magnitude of the interfacial charge that increasing under a temperature gradient can be explained by following reasons. The electric field is enhanced in the vicinity of the top electrode due to residual charge superposed by the newly applied electric field after PR operation, which could facilitate the charge injection from the top electrode. Moreover, the polarity of the interfacial charge is different compared to the polarity of the top electrode before the PR operation. After the PR operation, the interfacial charge has the same polarity compared to the top electrode. The high temperature of the top electrode could increase charge carrier mobility, leading to an increase in interfacial charge density.

The increase in interfacial charge density under the temperature gradient during PR can enhance the electric field in the oil after PR. Moreover, the high temperature of the top electrode can facilitate the space-charge injection, resulting in an enhanced electric field of oil after PR under the temperature gradient.

The electric field after PR is determined by the residual charge and external transient capacitive electric field. The residual charge is a sum of the previous injected space charge and the change in charge density during the PR process. The opposite trend of interfacial charge behaviour at ambient temperature and with temperature gradient results in different electric field enhancement trends in the oil after various PR time.

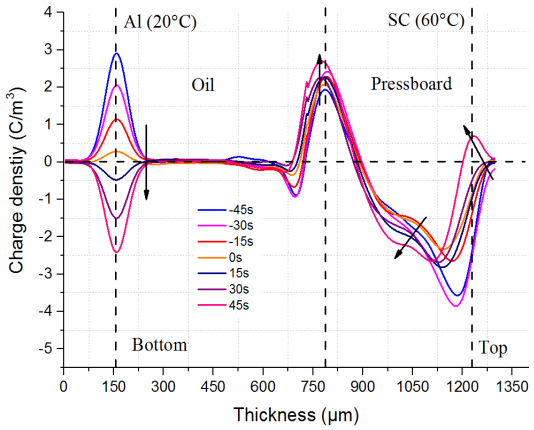

Figure 6-14: Space charge of two layers of oil and oil-impregnated PB during the polarity reversal operation from (-) to (+).

6.4.4 Multilayers effect

The ‘mirror image’ cannot be seen in the three layers of PB and oil with the comparison of the steady-state space charge under the voltage with different polarities at ambient temperature and the comparison of Figure 6-9 (a) and Figure 6-9 (b). This is because the interfacial barrier effect leads to a low dissipation rate of the interfacial charge density between the oil and PB. However, under the 40 °C temperature gradient, the ‘mirror image’ can be seen for three layers PB and oil shown in Figure 6-10. This is because the temperature can increase the charge carrier mobility, leading to rapid change of polarity for the interfacial charge between the oil and PB.

Figure 6-15 (a) shows the electric field of the multilayers PB+oil+PB at ambient temperature under negative voltage. The electric field in the PB increases while the electric field in the oil decreases. After the PR shown in Figure 6-15 (b), the electric field in the oil is enhanced due to the charge injections previously superposed by the transient capacitive electric field, leading to an electric field enhancement within the oil. For the PB, the homocharge injection previously could be considered as heterocharge after PR operation, leading to electric field enhancement in the vicinity of the electrode and interface between the oil and PB. The electric field in the oil decreases while the electric field of the PB increases with time after PR.

The interfacial charge at the multilayers PB+oil+PB interface has a slow dissipation rate at ambient temperature after PR as shown in Figure 6-8 (b). The slow dissipation rate of the interfacial charge reflects the fact that the electric field has a slow decrease after PR at ambient temperature as shown in Figure 6-15 (b).

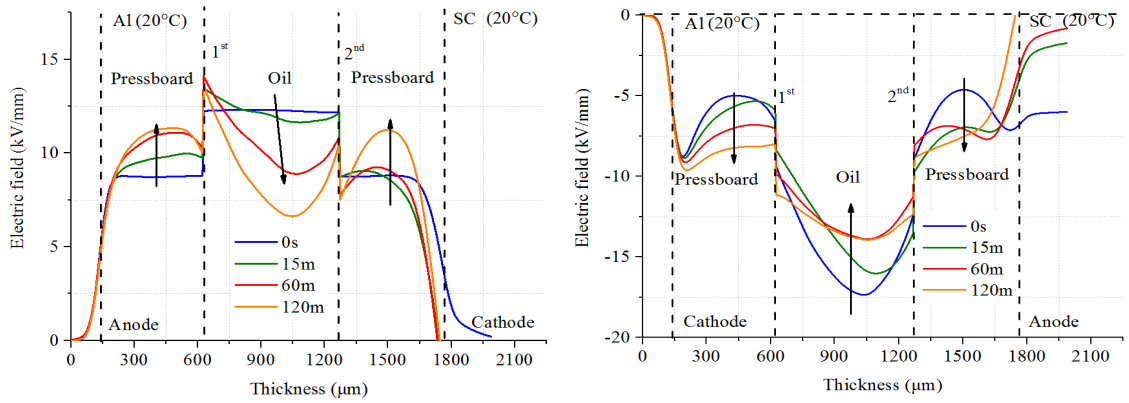

(a) Under negative (-) voltage (b) Under positive (+) voltage

Figure 6-15: Electric field of three layers of oil and oil-impregnated PB under ambient temperature with the voltage reversed from negative (-) to positive (+).

Figure 6-16 shows (a) the maximum electric field and (b) the electric field enhancement of oil

after PR under different experiment conductions. With the comparison of Figure 6-12 (b) and Figure 6-16 (b), the maximum electric field enhancement in the oil after PR is higher in three layers PB+oil+PB compared to two layers oil+PB under the same experiment conditions. From the design of the insulation material structure of the converter transformer, it is suggested that even numbers of insulation layers of oil and PB should be used to facilitate the charge dissipation and reduce the electric field enhancement of the oil gap after PR operation.

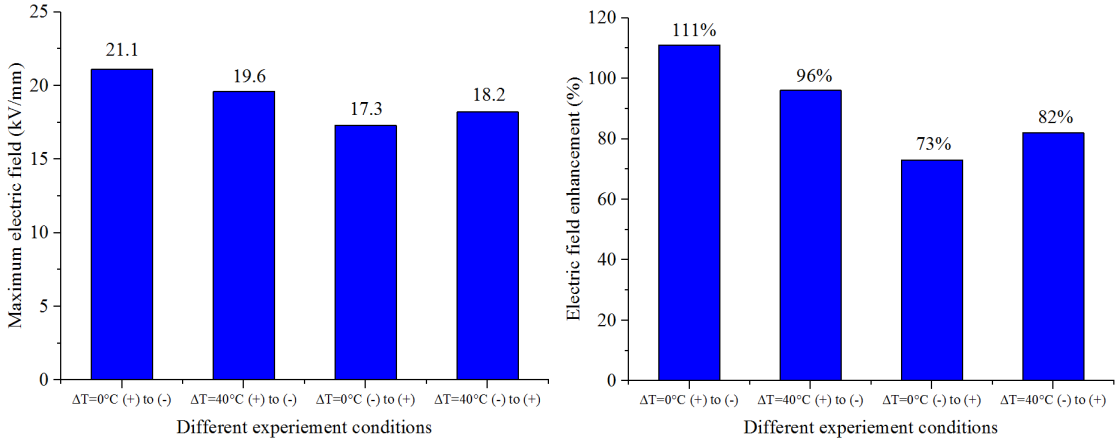

(a) (b)

Figure 6-16: The (a) maximum electric field and (b) electric field enhancement of oil in three layers PB+oil+PB after PR under different experiment conditions.

6.5 Summary

The PR effect on the space-charge behaviour of multilayers of oil and PB is investigated via a PEA system. The influential factors: temperature gradient, voltage polarity, different PR duration and multilayers samples are investigated. The findings are presented as follows.

For the two layers of oil and PB, after PR, the transient electric field in the oil reaches its maximum value at ambient temperature, while the steady-state electric field in the oil reaches its maximum value under the temperature gradient.

After PR for the two layers of oil and PB, it takes less time for the interfacial charge density to change its polarity, under the temperature gradient, compared to the ambient temperature.

In terms of the two layers of oil and PB, more interfacial charge accumulates at the oil and PB interface under negative (-) voltage, leading to the higher electric field enhancement in the oil with the voltage reversed from (-) to (+), especially under the temperature gradient.

For two layers of oil and PB, with longer PR time, the maximum electric field of fresh oil decreases at ambient temperature, while it increases under the temperature gradient.

In terms of the multilayers of oil and PB samples, a ‘mirror image charge’ is not seen in the comparison of the steady-state space charge with the voltage of different polarities under the ambient temperature. After PR, the maximum electric field occurs in the oil and decreases slowly with time at ambient temperature. Under the temperature gradient, a ‘mirror image charge’ can be seen with the comparison of the steady-state space charge under the voltage of different polarities. The electric field enhancement factor of the multilayers of oil and PB samples is higher compared to the two-layer samples under the same experiment conditions.

Chapter 7 The electric field distribution of the multilayers oil and PB considering the space charge effect

The wide application of the insulation materials under dc voltage raises a concern of space charge effect on the electrical performance of insulation materials. This chapter firstly introduces the transient and steady state electric field based on the Maxwell-Wagner theory. Then the experimental investigation of the space charge of two layers consisting of oil and PB is presented. The ageing and different electric fields on the dynamics of the space charge are reported and discussed. In addition, the measured space charge is further interpolated into the COMSOL software to evaluate the transient and steady state electric field of two layers oil and PB. To further investigate the multilayers and thick oil and PB electric field performance, the thickness effect on the two layers of oil and PB space charge results are presented. The space charge dynamics of thick and multilayers of oil and PB are estimated and the space charge addition method for thick and multilayers samples to COMSOL software is proposed. The transient and steady state of thick and multilayers oil and PB electric field results caused by space charge are discussed.

7.1 The transient and steady state electric field distribution based on the Maxwell-Wagner theory

Based on equations (2-11), (2-12) and (2-13) from the Maxwell-Wagner theory, the electric field of oil and PB are deduced as:

$$E_{PB}(t) = \frac{\gamma_{oil}}{\gamma_{PB}d_{oil} + \gamma_{oil}d_{PB}} V(1 - e^{-\frac{t}{\tau}}) + \frac{\varepsilon_{oil}}{\varepsilon_{PB}d_{oil} + \varepsilon_{oil}d_{PB}} V e^{-\frac{t}{\tau}} \quad (7\text{-}1)$$

$$E_{oil}(t) = \frac{\gamma_{PB}}{\gamma_{PB}d_{oil} + \gamma_{oil}d_{PB}} V(1 - e^{-\frac{t}{\tau}}) + \frac{\varepsilon_{PB}}{\varepsilon_{PB}d_{oil} + \varepsilon_{oil}d_{PB}} V e^{-\frac{t}{\tau}} \quad (7\text{-}2)$$

$$\tau = \frac{d_{oil}\varepsilon_{PB} + d_{PB}\varepsilon_{oil}}{d_{oil}\gamma_{PB} + d_{PB}\gamma_{oil}} \quad (7\text{-}3)$$

where $E_{PB}(t)$ and $E_{oil}(t)$ are the electric fields of PB and oil. γ_{oil} (S/m) and γ_{PB} (S/m) are the conductivities of oil and PB, ε_{oil} and ε_{PB} are the dielectric permittivities of oil and PB, d_{oil} (m) and d_{PB} (m) are the thickness of the oil and PB. τ (s) is a time constant. The thickness of the PB and oil are 1 mm and 0.5 mm separately. The V is an external voltage and equals to 18 kV in this case. The thickness and voltage selection is based on the following space charge experiments for the comparisons.

The conductivities, dielectric permittivity of fresh oil and PB are summarised in Table 7-1.

Table 7-1: The dielectric properties of fresh oil and PB [93]

Sample	Relative Permittivity	Resistivity TΩm
Fresh oil-PB	3.2	140
Fresh oil	2.2	7

Based on the dielectric properties of fresh oil and PB and equations from (7-1) to (7-3), the transient and steady state electric field of the oil and PB calculation results are shown in Table 7-2.

Table 7-2: The transient and steady electric field of the oil and PB

Time (s)	E_{op} (kV/mm)	E_{oil} (kV/mm)
t=0	10.42	15.16
t=100	12.26	11.47
t=10799 (∞)	17.38	1.24

The transient and steady state electric field of two layers oil and PB are also simulated using COMSOL software. The simulation results are compared to the calculation results shown in Table 7-2 to verify the correctness of the model. Moreover, the transient electric field of two layers oil and PB after PR is further investigated via the model.

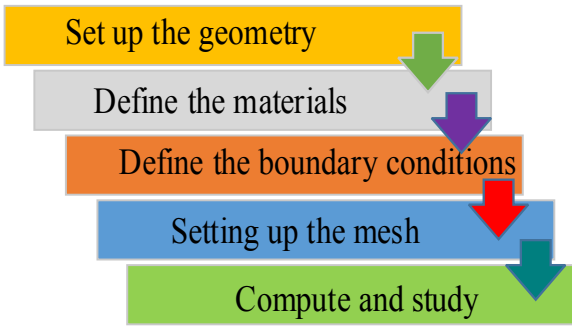

Figure 7-1:The different steps of the modelling.

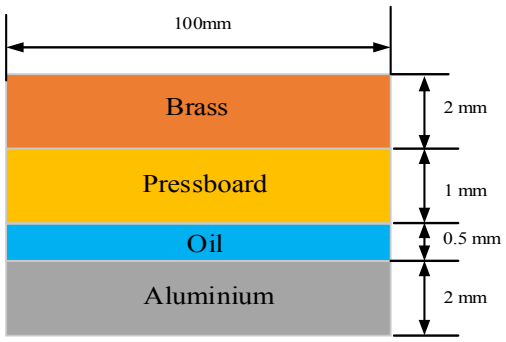

Figure: 7-2 The geometry of the oil and PB.

The different steps of building the model are shown in Figure 7-1. The electric current model is selected to calculate the time dependent electric field distribution of two layers of oil and PB. The geometry of two layers oil and PB are presented in Figure: 7-2. The geometry of two layers oil and PB are the same compared to the following experiment results. The ageing effect on the

electric field of two layers of the oil and PB is also simulated and the samples dielectric properties are shown in Table 7-3. The boundary condition is set up as follows: the voltage of the brass electrode is set up with the PR voltage shown in Figure 7-3. Two different electric fields including 12 kV/mm and 20 kV/mm are investigated. The red circles shows that the different PR time effect on the transient electric field of two layers oil and PB are investigated later. The voltage of the aluminium electrode is set to zero. In mesh level selection, the "extremely fine" level of mesh is elected to calculate the electric field distribution of two layers oil and PB.

Table 7-3: Sample properties of the fresh and aged insulation materials

Sample	Thickness mm	Relative Permittivity	Resistivity TΩm
Fresh PB	1	3.2	140
Fresh oil	0.5	2.2	7
Aged PB	1	4.2	0.3
Aged oil	0.5	2.6	0.1

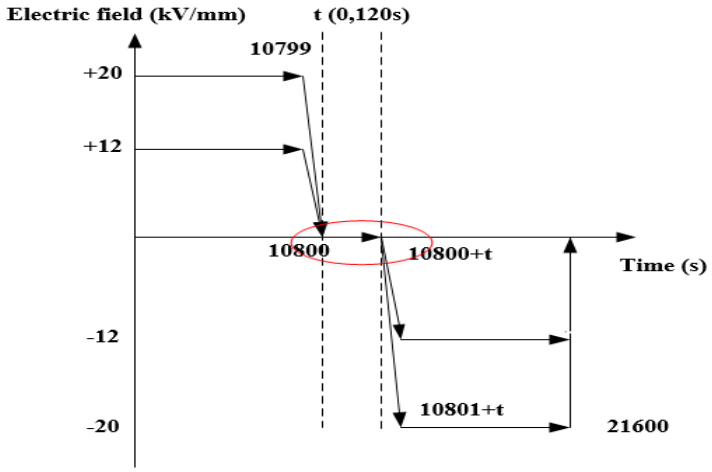

Figure 7-3: The PR operation voltage waveform.

Figure 7-4 (a) and (d) shows the electric field simulation result for the fresh oil and oil-impregnated PB under 12 kV/mm at 0 s and under -12 kV/mm at 60 s after the PR operation. At the transient state, the electric field follows the capacitive distribution. From the electric field calculating equations for the transient state, the electric field in the PB is proportional to capacitance of the oil. Therefore, the electric field in the PB is much lower than that in the oil because of the lower permittivity of the oil compared to the PB.

Figure 7-4 (c) shows the field under 12 kV/mm at 10799 s. At steady state, the electric field of the PB is higher than that of the oil because the steady state electric field satisfies the resistive electric field distribution. Therefore, the electric field of the PB is higher compared to that of the oil due to the higher resistivity of the PB.

The electric field of the fresh oil and oil-impregnated PB under 12 kV/mm at 0 s, 100 s and 10799 s is the same compared to the electric field calculation results in Table 7-2. It validates that the model built in COMSOL is capable of simulating the electric field of two layers oil and PB based on the Maxwell-Wagner theory, and of further investigating the electric field after the PR operation.

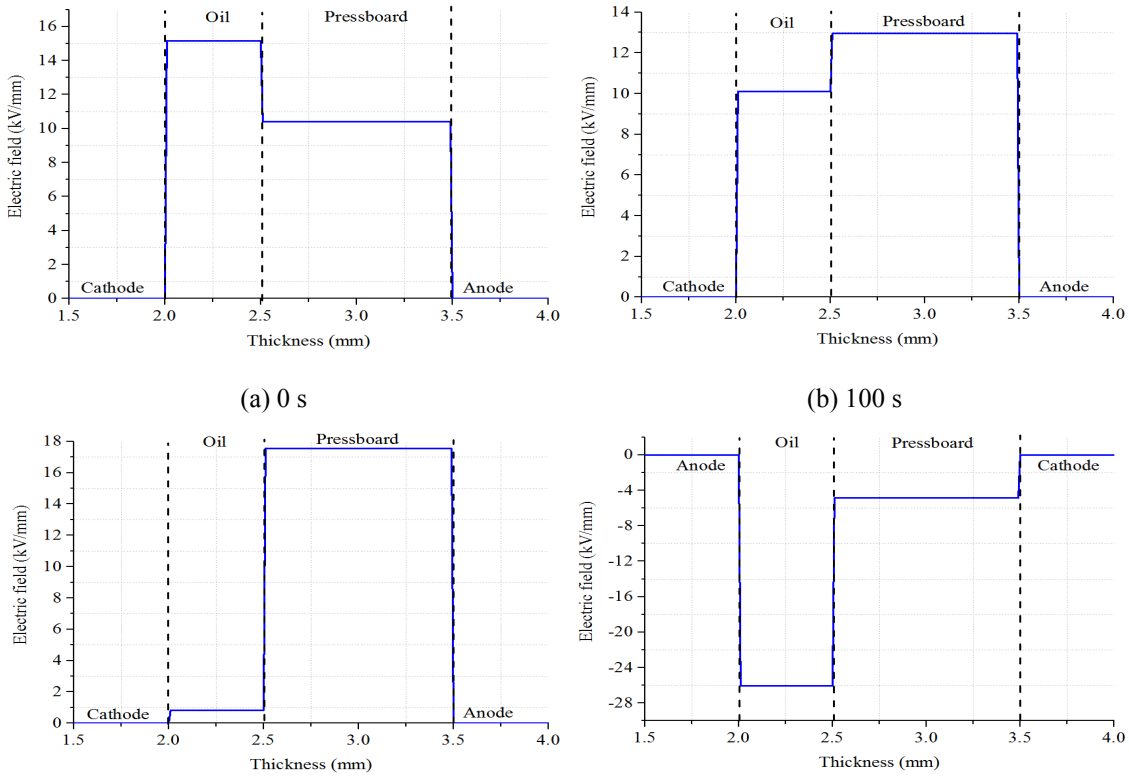

Figure 7-4: Electric field distribution at (a) t=0 s, (b) t=100 s, (c) t=10799 s and (d) t= 60 s after PR.

7.2 The ageing and different electric field effects on the space charge behaviour

The Maxwell-Wagner theory has been found to only work for linear materials without consideration of charge traps and recombination. In reality, there is a significant deviation from the theory as the influence of charge traps and surface states of the materials are not considered in the theory. The surface of the oil-impregnated PB contain lots of traps considering broken bonds and chain folds, leading to extra space charge accumulation at the interface [34]. The charge traps

and surface states make the electric field in the system unpredictable. Therefore, it is important to understand the charge dynamics of these trapped charges.

Several factors such as the sample thickness, moisture, temperature, applied field and ageing status of materials can affect the characteristics of the space charge [94] [95] [96]. In this section, the effect of the ageing status of oil and different applied electric stress on space charge results are presented and discussed.

Figure 7-5 shows a schematic diagram of investigating the space charge of two-layer oil and PB. A PTFE ring was served as the spacer and container for the oil. The PB was placed on a PTFE spacer. The PB has a thickness of 1 mm and oil has a thickness of 0.5 mm. After placing the electrode on the sample, the fixed pressure was applied to the sample to maintain the sufficient contact between the electrode and sample.

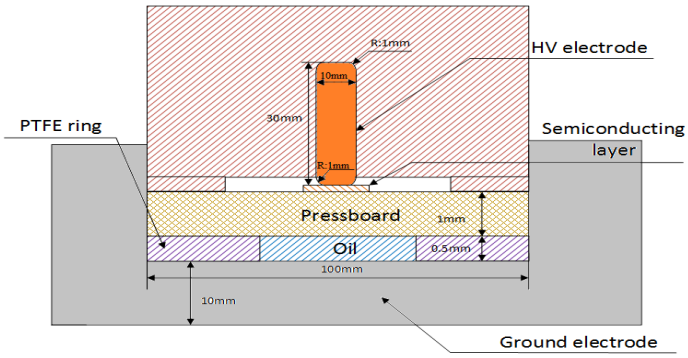

Figure 7-5: The configuration of the PEA system.

To investigate the ageing and different applied electric fields on space charge behaviour of the two layers oil and PB, the test conditions are designed as follows: i) Fresh samples under the electric field of both 12 kV/mm and 20 kV/mm; ii) Aged samples under the electric field of both 12 kV/mm and 20 kV/mm. The details are shown in Table 7-4.

Table 7-4: Experiment plan of the space charge measurement

	Properties	Voltage	Sample	Thickness (mm)	Electric field (kV/mm)
Two layers	Fresh	DC (+)	PB+oil	1 PB+ 0.5 oil	12, 20
	Aged				

7.2.1 Space charge results

Figure 7-6 (a) shows the space charge of two layers of fresh oil and PB under an electric field of 12 kV/mm. The two solid vertical lines represent the position of the two electrodes while the dotted line is the interface between the oil and the PB.

A homocharge injection from the two electrodes is observed, resulting in a positive charge in the vicinity of the anode and a negative charge accumulation at the interface (see Figure 7-6 (a)). The negative charge migrates across the oil layer and accumulates at the oil PB interface, leading to the decrease of the negative cathode peak. Moreover, the positive charge is injected from the anode and increases with the time.

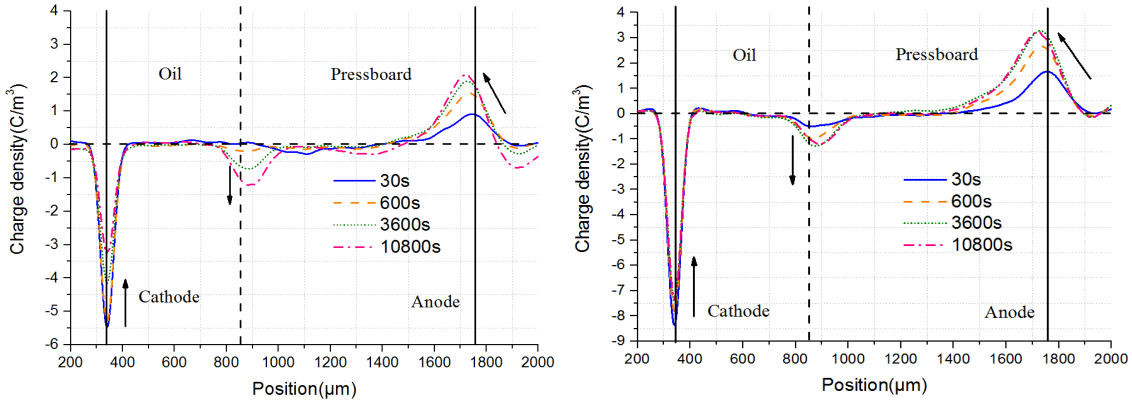

(a) 12 kV/mm (b) 20 kV/mm

Figure 7-6: Space charge density of the fresh oil and oil-impregnated PB under an applied electric field of (a) 12 kV/mm and (b) 20 kV/mm.

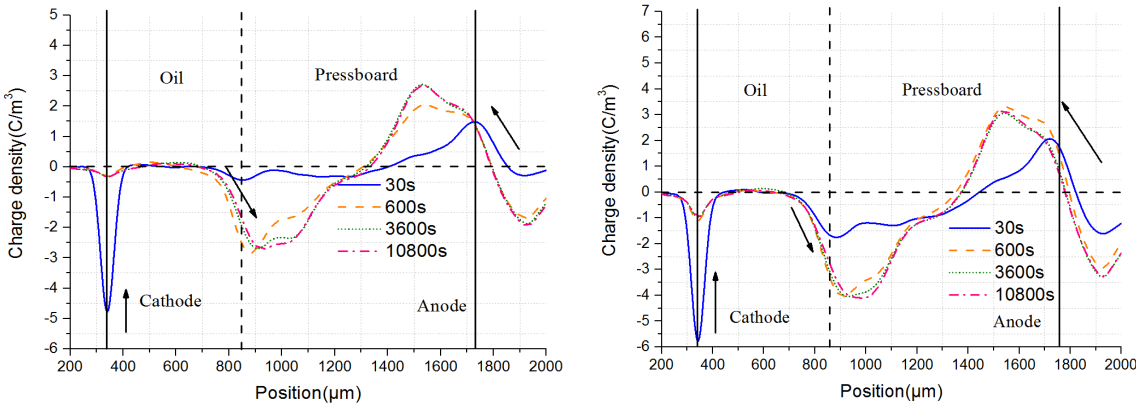

(a) 12 kV/ mm (b) 20 kV/ mm

Figure 7-7: Space charge density of the aged oil and oil-impregnated PB under an applied electric field of (a) 12 kV/mm and (b) 20 kV/mm.

Figure 7-6 (b) shows space charge evolution in the fresh oil and oil-impregnated PB sample under the applied electric field of 20 kV/m. Compared to Figure 7-6 (a), the charge density for both electrodes under 20 kV/mm is higher than that under 12 kV/mm, especially on the cathode where the charge density is -8 C/m^3 under 20 kV/mm compared with -5.5 C/m^3 under 12 kV/mm.

Figure 7-7 (a) shows space charge distribution of the aged oil and oil-impregnated PB stressed

under 12 kV/mm. Compared to Figure 7-6 (a), the faster increase of the charge density, the larger amount of charge injection from the electrode and the deeper of the positive peak migration distance are the three main features of space charge in the aged oil-impregnated PB.

Figure 7-7 (b) shows the space charge density of the aged oil and oil-impregnated PB stressed under 20 kV/mm. Compared to Figure 7-7 (a), the steady state interfacial charge density is 4 C/m^3 under an electric field 20 kV/mm, which is higher than 3 C/m^3 under an electric field 12 kV/mm.

Figure 7-8 (a) shows the decay of space charge in fresh two layers oil and PB after three hours of stressing under an electric field of 12 kV/mm. It shows that the polarity of the space charge on both electrodes is positive, which is the result of the superposition of the induced charge from the negative interfacial charge and the injected charge from the electrodes. The induced positive charges on both electrodes decrease gradually due to the charge dissipation and neutralisation within the dielectric materials.

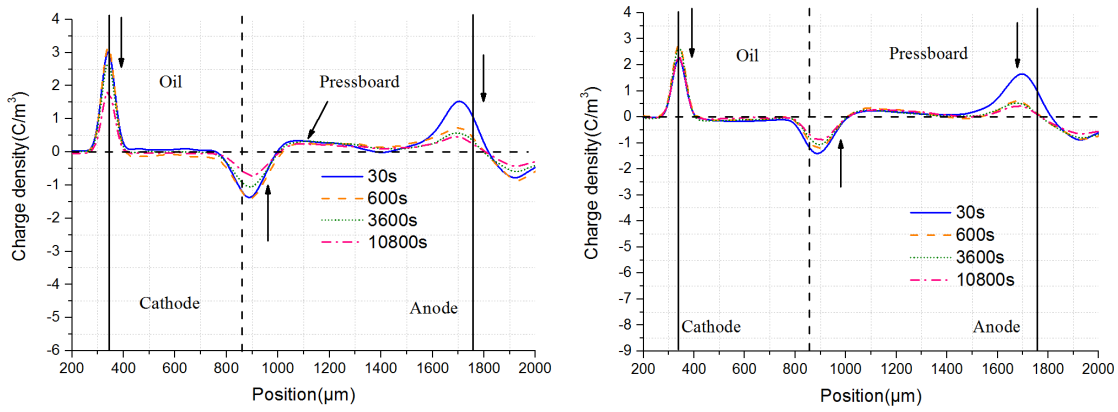

(a) 12 kV/mm (b) 20 kV/mm

Figure 7-8: Space charge decay of the fresh oil and oil-impregnated PB after 3 hours of stressing under an electric field of (a) 12 kV/mm and (b) 20 kV/mm.

Figure 7-8 (b) shows the decay of space charge in fresh two layers oil and PB after three hours of stressing under an electric field of 20 kV/mm. The fresh oil and PB do not have the significant reduction of the interfacial charge density after three hours and it decreases from 1.5 C/m^3 to 1 C/m^3.

Figure 7-9 (a) shows the decay process of the space charge distribution of the aged oil and oil-impregnated PB after three hours of stressing under 12 kV/mm. It shows that the charge density decreases rapidly and there is little space charge left after five minutes. This phenomenon shows that the electric field for the aged oil-PB will decrease much faster compared to the fresh oil-PB.

Figure 7-9 (b) shows the decay process of the space charge distribution of the aged oil and oil-

impregnated PB after three hours of stressing under 20 kV/mm. The higher external electric field leads to the higher magnitude of the interfacial charge density of 3.5 C/m^3 compared to 2.5 C/m^3 under the 12 kV/mm.

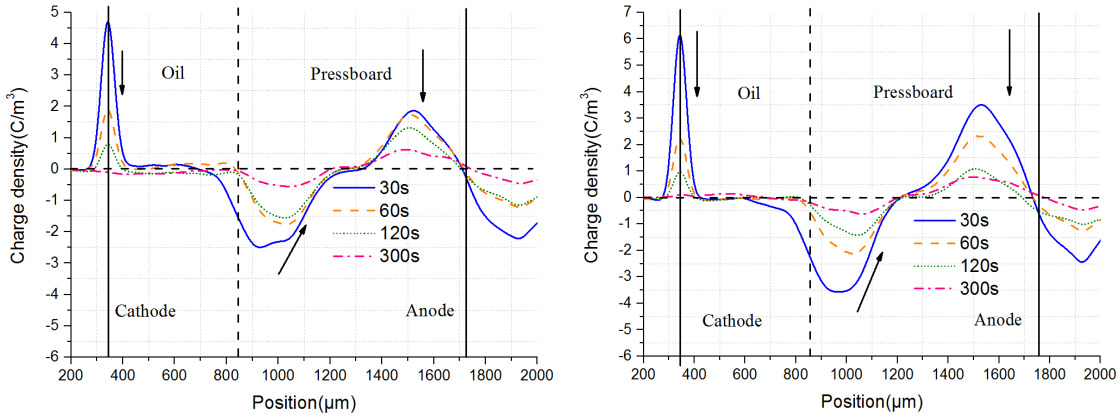

(a) 12 kV/mm (b) 20 kV/mm

Figure 7-9: Space charge decay of the aged oil and oil-impregnated PB after 3 hours of stressing under an electric field of (a) 12 kV/mm and (b) 20 kV/mm.

7.2.2 Discussion

The interfacial charge has the same polarity as the electrode in contact with the oil. There are two main reasons leading to this phenomenon. Firstly, based on the equation (2-20), the surface charge σ (C/m^2) is calculated based on the dielectric permittivity of the oil ε_{oil} and PB ε_{op}, and the conductivity of the oil γ_{oil} and PB γ_{op}, shown in equation (7-4). Due to the lower conductivity of PB compared to the oil, the polarity of the interfacial charge is negative. Secondly, the larger conductivity of the oil will make the injected negative charge in the oil and move to the interface easier under the influence of the electric field. On the other hand, the injected positive charge from the anode may be trapped in the region adjacent to the electrode, hindering further charge injection. Therefore, the polarity of the interface charge should be the same as that of the electrode in contact with the oil [34].

$$\sigma = \frac{\varepsilon_{oil}\gamma_{op} - \varepsilon_{op}\gamma_{oil}}{\gamma_{op}d_{oil} + \gamma_{oil}d_{op}} V \tag{7-4}$$

Comparing with the space charge behaviour in fresh and aged samples, the faster increase of the charge density, the larger amount of charge injection from the electrode and the deeper of the positive peak migration distance are three main features of the space charge in aged oil and oil-impregnated PB. Several reasons could account for this phenomenon.

The faster increase of the charge density of aged samples compared to fresh ones are correlated

with the time constant based on equation (7-3) above. Based on the dielectric properties of samples shown in Table 7-3, the time constant of fresh and aged samples are $\tau_{\mathrm{fresh}} = 325$ s and $\tau_{\mathrm{aged}} = 3.6$ s respectively, which reflects that the charge of aged samples can increase and decrease faster compared to fresh ones.

The larger magnitude of the charge on the electrode of aged samples compared to fresh ones are attributed to the following equation:

$$Q = CV \tag{7-5}$$

where Q is the charge density (C), V is external voltage (V) and C is the capacitance with the unit of (F). Due to the increase of the dielectric constant of the aged samples, the magnitude of charge on the electrode increase in aged samples compared to fresh ones.

7.3 The methodology of the space charge interpolation into the COMOSL software of two layers oil and PB

7.3.1 The interpolation method of the space charge into the COMSOL software

There are two advantages to interpolate the space charge into the COMSOL software. Firstly, the electric field caused by the space charge can be quantitatively simulated with the emphasis on the electric field after the PR operation. The difference between the electric field calculated using the measured space charge and Maxwell-Wagner can be evaluated. Secondly, for the thicker PB (such as 3mm) or multilayers of oil and PB space charge behaviour, it is difficult to measure the space charge directly using the PEA equipment due to the severe attenuation and dispersion phenomenon [97]. Therefore, if there is a methodology that allows one to extend the space charge from thinner samples to thicker ones, the electric field in a converter transformer can be simulated using space charge via COMSOL software.

The electric field based on the Maxwell-Wagner theory depends on the dielectric properties such as the dielectric permittivity and conductivity of the different insulation materials. The electric field calculated by the space charge is determined by the space charge density and its distribution. Once the measured space charge density is interpolated, the electric field can be calculated without the consideration of the difference in the conductivity of different dielectric materials.

The details of the space charge interpolation methodology into two layers oil and PB contain different procedures including subtraction, division, average, curve fitting and interpolation, as shown in Figure 7-10. Firstly, the subtraction means the subtraction of the space charge and the capacitive charge to remove the capacitor charge on the electrodes. Figure 7-11 indicates the reference calibration space charge density and charge density at 180 minutes of the fresh oil and

oil-impregnated PB under an electric field of 12 kV/mm. Figure 7-12 shows the configuration of net space charge results after subtracting the reference calibration charge density of fresh oil and oil-impregnated PB at three hours.

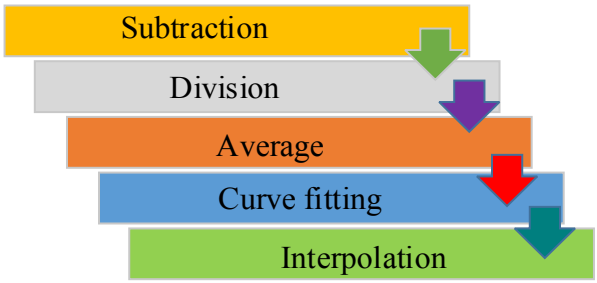

Figure 7-10: The space charge interpolation method in COMSOL.

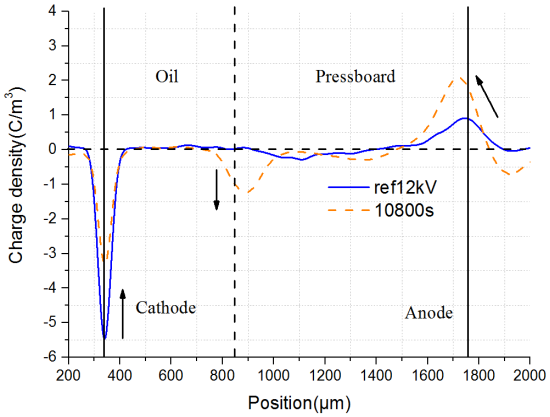

Figure 7-11: Space charge for fresh oil and oil-impregnated PB under an applied electric field of 12 kV/mm.

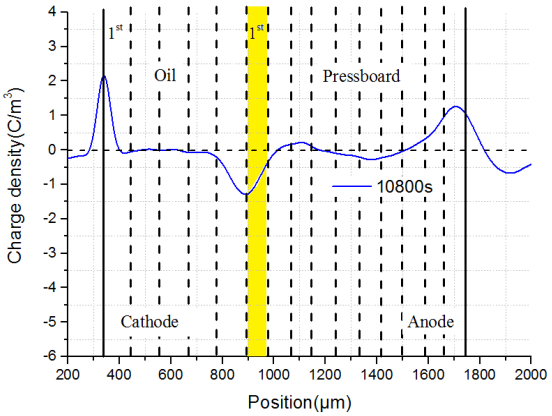

Figure 7-12: Configuration of the space charge density after subtracting the calibration charge density at 180 minutes.

Secondly, the oil and PB have been divided into fifteen layers for adding the related space charge density, which is shown in Figure 7-12. The 0.5 mm thickness oil is divided into 5 layers and the 1 mm thickness PB is divided into 10 layers.

Thirdly, for each layer of the space charge density, the space charge density is averaged using the following equation (7-6) to get the average charge density. After the calculation, there are fifteen average points of fifteen layers after calculation.

$$\frac{\sum Charge\ Density}{point} = Average\ charge\ density \tag{7-6}$$

Fourthly, the average charge density of each layer versus the time varies from 0 s to 10800 s can be simulated by the curve fitting functions in MATLAB. An example of the first layer of the PB is selected shown in Figure 7-12. The relationship between the charge density and time is

presented based on the curve fitting function in the MATLAB, shown in Figure 7-13 (a).

After the observation of the relationship between the space charge versus the time, two exponential functions are used for the voltage application process, which could be attributed to the deep and shallow traps resulted from the physical and chemical defects within the insulation materials. However, for the decay process, only one exponential is used, which represents that only shallow trap space charge could release due to the short PR time [98]. The typical equation of the space charge density versus time of the first layer of the PB and oil is represented in equations (7-7) to (7-10).

The space charge q(t) versus time of stressing and decay process of the first layer of PB are described as follows:

$$q(t) = -0.611 \times e^{6.165\times10^{-5}t} + 0.5658 \times e^{-6.576\times10^{-4}t} \quad (0<t<10800) \quad (7\text{-}7)$$

$$q(t) = -0.7516 \times e^{4.441\times10^{-5}t} \quad (10800<t<10920) \quad (7\text{-}8)$$

The stressing and decay of space charge versus time of the first layers of oil are described as follows:

$$q(t) = 0.9865 \times e^{2.391\times10^{-5}t} - 1.203 \times e^{-4.139\times10^{-4}t} \quad (0<t<10800) \quad (7\text{-}9)$$

$$q(t) = 4026 \times e^{7.687\times10^{-4}t} \quad (10800<t<10920) \quad (7\text{-}10)$$

Finally, the space charge can be interpolated into the COMSOL after the interpolation of equations above in it. For example, after the interpolation of the equations (7-7) to COMSOL, Figure 7-13 (b) shows that two exponential functions approximately reflect the space charge density versus time, which is the same compared to Figure 7-13 (a). Using a similar approach, the space charge density versus time has been successfully imported into fifteen layers of oil and PB.

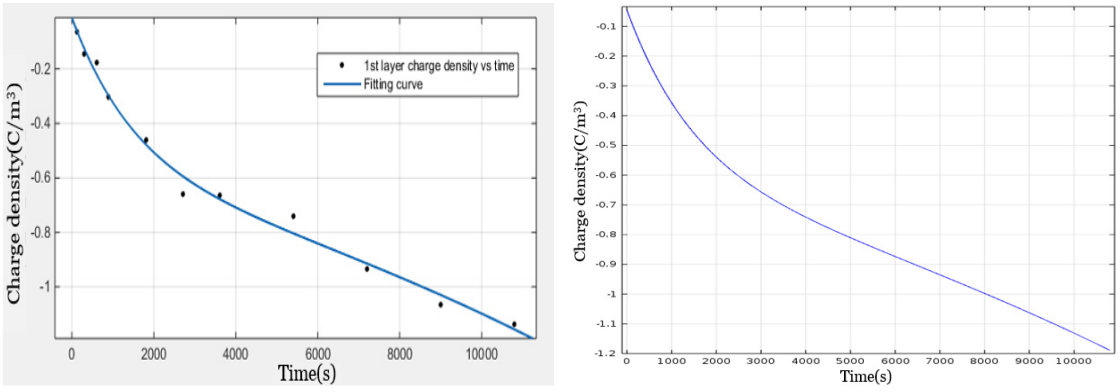

(a) From MATLAB (b) From COMSOL

Figure 7-13: Simulation of space charge density versus the time for the 1st layer of PB.

The electrostatic model is selected to calculate the time dependent electric field distribution of two layers oil and PB. The geometry of two layers oil and PB are shown in Figure: 7-2. The boundary condition is the same as the previous setting shown in Figure 7-3. In mesh level setting, the "extremely fine" level of mesh is selected. Different PR time effect on the electric field based on the space charge will be simulated later.

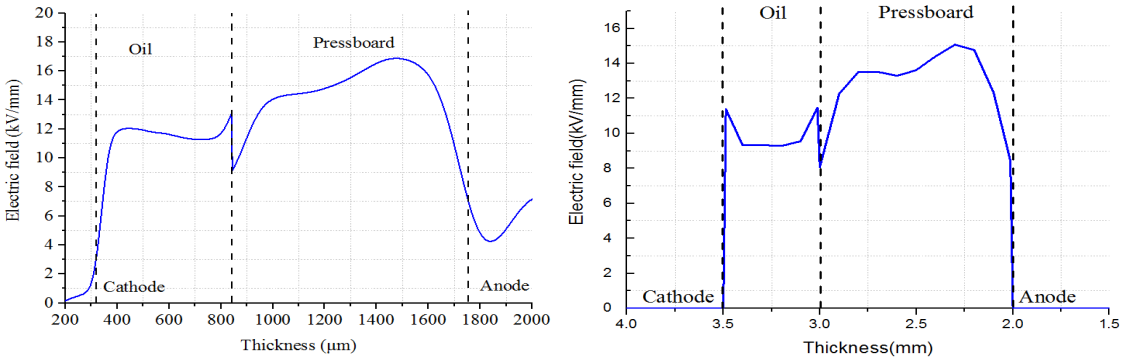

(a) (b)

Figure 7-14: The electric field calculated by (a) space charge and (b) COMSOL of two layers 0.5 mm oil and 1 mm PB at 10799 s under 12 kV/mm.

Figure 7-14 illustrates the electric field calculated by (a) space charge directly and by (b) COMSOL software. It shows that the maximum electric field is similar, and deviation of the maximum electric field is around 10 %, which indicates that the proposed method can correctly simulate the electric field based on the space charge density.

The charge can also be interpolated into the COMSOL software directly, using the interpolation function in COMSOL software. Compared to this method, the proposed space charge interpolation method has several advantages. Firstly, it is difficult to measure the space charge of multilayers, thick oil and PB directly, due to the acoustic wave attenuation, dispersion and reflection of the acoustic wave propagation in the samples. However, the proposed space charge interpolation method can be used to simulate the electric field produced by the estimated charge density in multi-layers of thick oil and PB (the methodology is described in section 7.4). Secondly, the equations representing the charge density versus the time are interpolated into COMSOL. The transient time-dependent electric field calculated by the space charge can be simulated, with the emphasis on the electric field after the PR operation. Thirdly, the thickness of the oil and PB sample may have a slight change due to the application of unstable external pressure to the upper electrode in each of the space charge measurement. This may lead to inaccuracy in the electric field calculation, which is based on the direct space charge interpolation method.

Due to complicated physical processes involved in charge formation and decay, there are no equations to describe the precise relationship between space charge density versus the time. To

simplify the simulation in COMSOL, it is necessary to use the approximated functions to simulate the variation trend of space charge density versus time from the experimental results. Consequently, the effect of charge dynamics on the electric field during PR can be fully assessed, which could be beneficial to analyse more complex oil and oil-impregnated PB structure in the future.

7.3.2 The transient and steady state electric field distribution

Figure 7-15 (a) is the steady state electric field at 10799 s in the oil and oil-impregnated PB after adding the space charge. It can be clearly observed that there is an enhancement in the electric field of the PB compared to the average applied electric field 12 kV/mm. The homocharge injection and migration into the PB from two electrodes are shown in Figure 7-6 (a), which enhances the electric field within the PB. However, charges injected from the cathode move towards the interface under the influence of the applied electric field and accumulate at the interface, which leads to the decrease in the electric field within the oil.

Figure 7-16 shows a schematic diagram after applying the HVDC voltage for PB. The electric field in the middle caused by the homocharge has the same direction as the applied electric field. Therefore, the electric field in the middle is enhanced. Meanwhile, the change in the electric field in the vicinity of the anode and interface can be explained in two ways. From Figure 7-16, the electric field caused by the homocharge in the vicinity of the anode and interface can resist the increase of the applied electric field. Moreover, the homocharge in the vicinity of the two electrodes can induce the opposite polarity charge on the electrode, which could weaken the electric field in the vicinity of the anode and interface. In comparison with Figure 7-15 (a) and Figure 7-4 (c), the maximum electric field of PB after adding the space charge at a steady state of 10799 s is 15.1 kV/mm while the maximum electric field calculated from the Maxwell-Wagner theory is 17.6 kV/mm, i.e. the maximum electric field of PB after adding the space charge is about 86% of the maximum electric field calculated from the Maxwell-Wagner theory.

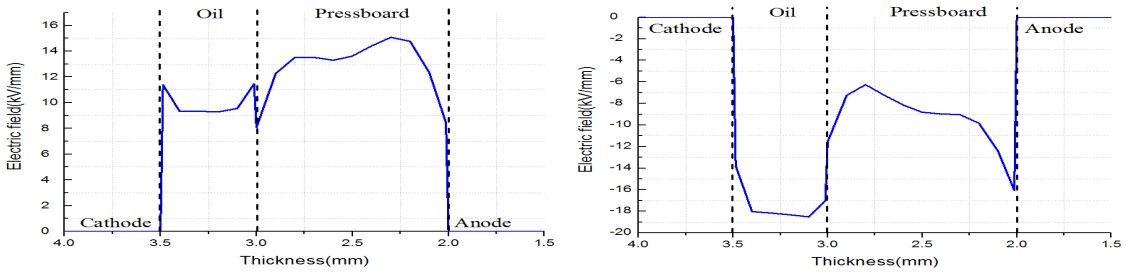

(a) t=10799 s (b) t=60 s

Figure 7-15: Electric field of fresh oil and oil impregnated PB under 12 kV/mm adding space charge (a) at 10799 s and (b) at 10861 s after PR time of 60 s.

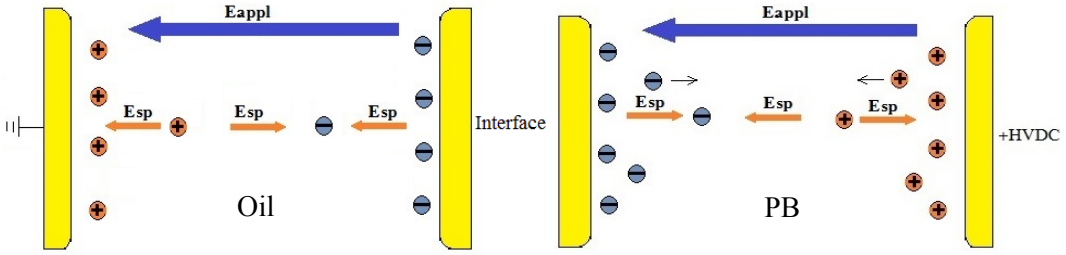

Figure 7-16: Space charge distribution under the HVDC voltage.

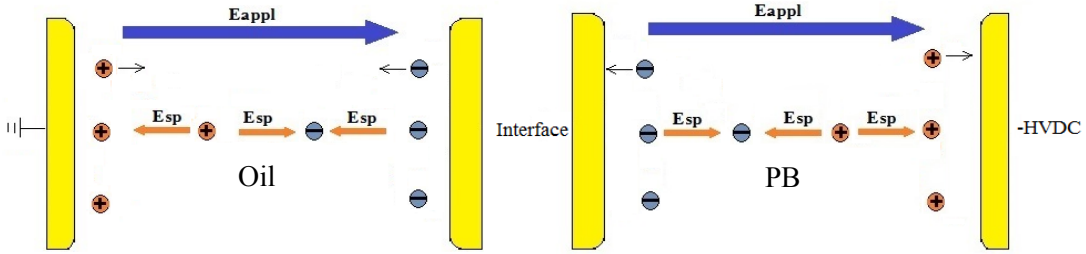

Figure 7-17: Space charge distribution after the PR operation.

Figure 7-15 (b) shows the electric field in the oil and oil-impregnated PB after adding the space charge under -12 kV/mm after 60 s PR time. It is noticed that there is a concave region for the electric field in the PB. The electric field in the vicinity of the anode and interface is increased.

This phenomenon could also be explained in two ways. The homocharge injection in the previous period of voltage application now can be viewed as heterocharge after the PR operation. The electric field in the vicinity of the anode and interface is caused by the heterocharge adding the applied electric field, leading to the electric field enhancement shown in Figure 7-17. Moreover, the heterocharge can induce the same polarity charge compared to the electrodes, which strengthens the electric field at the cathode and interface between the oil and PB. For the oil part, the enhancement of the electric field within the oil is also attributed to the existence of space charge. The charge injection for the cathode previously could be converted into homocharge after the PR operation, leading to the electric field enhancement within the oil. After the PR operation, the maximum electric field occurs in the oil gap.

7.3.3 The discussion

7.3.3.1 Fresh oil and oil-impregnated PB under 12 kV/mm

Table 7-5 indicates the maximum electric field in the fresh oil-impregnated PB adding the space charge E_{max1} and using the Maxwell-Wagner theory E_{max2} under various PR time. It is noticed that the E_{max2} increases gradually while E_{max1} decreases with time. The amount of the charge density decreases slowly from 1.5 C/m^3 to 1 C/m^3 in 2 minutes, as shown in Figure 7-8 (a). Therefore, this small amount of charge density cannot produce a significant electric field distortion within

the PB. The electric field enhancement can be calculated as follows:

$$f=(E_{max1}-E_{max2})/\ E_{max2} \quad (7\text{-}11)$$

Table 7-5: Electric field of the fresh PB under 12 kV/mm for different PR time

PR time (s)	E_{max1} (kV/mm)	E_{max2} (kV/mm)	Field enhancement f
10	-18.3	-3.6	408.30%
20	-17.8	-3.8	368.40%
30	-17.4	-4.2	314.30%
40	-16.9	-4.4	284.10%
50	-16.5	-4.7	251.10%
60	-16.1	-4.9	228.60%
70	-15.7	-5.2	201.90%
80	-15.3	-5.4	183.30%
90	-14.9	-5.6	166.10%
100	-14.6	-5.8	151.70%
110	-14.2	-6	136.70%
120	-13.9	-6.2	124.20%

Table 7-6: Electric field of the aged PB under 12 kV/mm for different PR time

PR time (s)	E_{max1} (kV/mm)	E_{max2} (kV/mm)	Field enhancement f
10	-19.4	-10.3	88.60%
20	-17.8	-10.5	69.80%
30	-16.7	-10.5	58.70%
40	-15.7	-10.5	49.40%
50	-15.1	-10.5	42.80%
60	-14.4	-10.5	36.50%
70	-13.8	-10.5	31.10%
80	-13.5	-10.5	28.20%
90	-13.1	-10.5	24.60%
100	-12.8	-10.5	21.70%
110	-12.6	-10.6	18.20%
120	-12.4	-10.6	16.50%

It has been found that the electric field enhancement f decreases from 408.3% to 124.2%, as illustrated in Table 7-5.

Since the electric field caused by space charge does not have obvious change, the steady electric field E_{max2} in the PB is 17.6 kV/mm, as shown in Figure 7-4 (c), which is higher than E_{max1}=-13.9 kV/mm after 120 s decay (see Table 7-5). Therefore, it is possible to shorten the PR time for the fresh oil and oil-impregnated PB under 12 kV/mm.

7.3.3.2 Aged oil and oil-impregnated PB under 12 kV/mm

Table 7-6 summarises the electric field using the Maxwell-Wagner theory when considering space charge for the aged oil-impregnated PB under various PR time. Compared to Table 7-5, it is noticed that the electric field E_{max1} shown in Table 7-6 decreases rapidly. The reason is that the amount of charge density decreases rapidly from 2 C/m^3 to 1 C/m^3 within 2 minutes, as shown in Figure 7-9 (a). The electric field enhancement range in the aged oil-impregnated PB varies from 88.6% to 16.5%, which is smaller than the electric field enhancement range in the fresh oil-impregnated PB, shown in Table 7-5. However, the electric field in the aged oil-impregnated PB considering space charge is higher than that of the fresh oil-impregnated PB. The steady state Maxwell-Wagner electric field for aged oil-impregnated PB is 15.4 kV/mm, which is higher than the E_{max1}=-13.1 kV/mm after the PR time of 90 s. Therefore, it is possible to shorten the PR time

for the aged oil and oil-impregnated PB under 12 kV/mm.

7.3.3.3 Fresh oil and oil-impregnated PB under 20 kV/mm

Table 7-7 is the electric field distribution of the fresh oil-impregnated PB when adding the space charge and using the Maxwell-Wagner theory under 20 kV/mm for various PR time. The electric field enhancement when adding space charge compared to the average electric field is around 5.3 kV/mm under 20 kV/mm, which is slightly lower than that around 6.3 kV/mm under 12 kV/mm. However, with the higher electric field 20 kV/mm applied on fresh oil and oil-impregnated PB, the positive charge injection is similar, around 1.5 C/m^3, for both fresh samples under different electric fields (see Figure 7-8 (a) and Figure 7-8 (b) form a comparison). This may result from the charge injection being saturated under the lower electric field for fresh oil and oil-impregnated PB. The maximum electric field E_{max2} of fresh oil-impregnated PB using the Maxwell-Wagner theory at steady state 10799 s under 20 kV/mm is 29.2 kV/mm. Therefore, the PR operation time could be reduced, as the maximum electric field E_{max1} is -25.3 kV/mm (shown in Table 7-7).

Table 7-7: Electric field of the fresh PB under 20 kV/mm for different PR time

PR time (s)	E_{max1} (kV/mm)	E_{max2} (kV/mm)	Field enhancement f
10	-25.3	-5.5	357.90%
20	-24.5	-6.4	284.10%
30	-23.9	-6.9	243.80%
40	-23.2	-7.4	213.60%
50	-22.7	-7.6	197.60%
60	-22.1	-8.2	168.50%
70	-21.6	-8.5	153.80%
80	-21.2	-9	135.10%
90	-20.7	-9.2	125.20%
100	-20.3	-9.7	109.60%
110	-19.9	-9.9	100.70%
120	-19.6	-10.3	89.50%

Table 7-8: Electric field of the aged PB under 20 kV/mm for different PR time

PR time (s)	E_{max1} (kV/mm)	E_{max2} (kV/mm)	Field enhancement f
10	-30.4	-17.1	77.60%
20	-29.2	-17.5	67.20%
30	-28	-17.7	57.80%
40	-26.8	-17.6	52.40%
50	-25.6	-17.6	45.80%
60	-24.6	-17.6	40.20%
70	-23.7	-17.6	35.00%
80	-22.9	-17.6	30.30%
90	-22.2	-17.6	26.20%
100	-21.6	-17.6	22.70%
110	-21	-17.7	18.70%
120	-20.6	-17.7	16.20%

7.3.3.4 Aged oil and oil-impregnated PB under 20 kV/mm

Table 7-8 summarises the electric field for the aged oil-impregnated PB using the Maxwell-Wagner theory and adding the space charge under 20 kV/mm for different PR time. The maximum electric field enhancement adding space charge compared to the average electric field is around 10.4 kV/mm, which is higher compared to that at 7.4 kV/mm under 12 kV/mm. The higher applied electric field will lead to more charge injection, resulting in severe electric field distortion. This

is attributed to less effect on charge trapping capability of aged oil and oil-impregnated PB under the higher electric field.

From Table 7-7 and Table 7-8, it can be seen that the reduction rate in the electric field E_{max1} is more obvious for the aged oil-impregnated PB compared to the fresh one. Due to the higher conductivity of the aged oil-impregnated PB, charges in oil and oil impregnated PB system have a higher migration rate, resulting in rapid charge reduction from 4 C/m^3 to 1 C/m^3 in 2 minutes, as shown in Figure 7-9 (b). This will lead to the rapid decrease in the electric field. The steady state Maxwell-Wagner electric field E_{max2} under 20 kV/mm is 25.7 kV/mm for aged oil-impregnated PB. Therefore, it is suggested that the PR time should be no less than 60 s according to Table 7-8 for the aged oil-impregnated PB under 20 kV/mm.

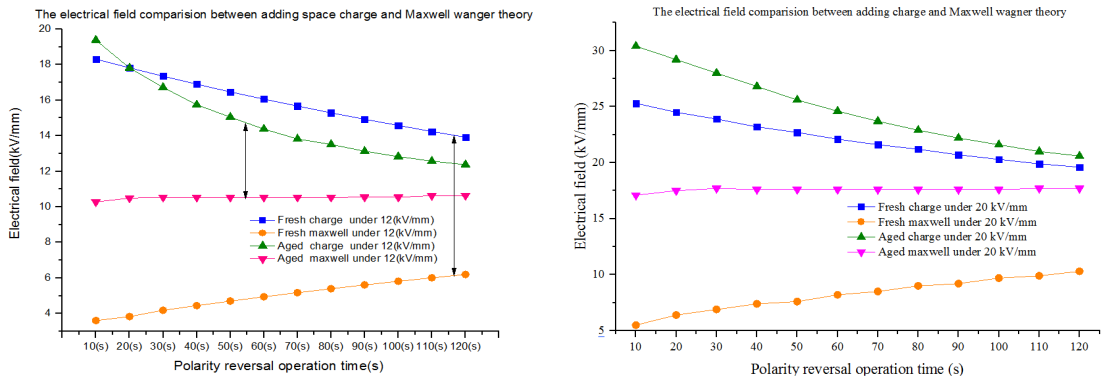

(a) 12 kV/mm (b) 20 kV/mm

Figure 7-18: Electric field distribution of both fresh and aged samples based on space charge and Maxwell-Wagner theory for different PR time under (a) 12 kV/mm and (b) 20 kV/mm.

The electric field caused by space charge or the Maxwell-Wagner theory after PR time under 12 kV/mm and 20 kV/mm is summarised in Figure 7-18 (a) and Figure 7-18 (b), respectively. From both figures for both fresh and aged samples, the electric field based on space charge is higher compared to the electric field calculated by the Maxwell-Wagner theory. Moreover, the electric field of the aged samples is higher compared to the fresh samples. The electric field based on the Maxwell-Wagner theory increases while the electric field caused by the space charge decreases after different PR operation time. It can be seen that the electric field of the aged sample caused by the space charge decreases faster compared to the fresh sample, which results from different dissipation rate of the space charge regarding the ageing status of the sample. Moreover, the difference between the electric field caused by the space charge and the Maxwell-Wagner theory is higher for the fresh sample and lower for the aged samples.

7.4 The multilayers effect on the electric field distribution of oil and PB when considering the space charge effect

Under the HVDC system, space charge build-up has been one of the significant issues that need to be addressed. The presence of space charge can enhance the local electric field, which leads to part of the insulation materials being overstressed. In the worst situation, it may result in material degradation and possibly permanent breakdown [98]. Therefore, the influential factors on space charge formation and dissipation need to be carefully investigated such as temperature, moisture, ageing, electric field and multilayers [48][64][66][80][81]. In section 7.2, the effects of the ageing status of oil and different applied electric stress on space charge behaviour have been investigated. In section 7.4, the multilayers and thickness of oil and PB effect on the space charge dynamics will be discussed.

Multi-layered dielectric materials contain the interfaces which are the weak points of the HV equipment [67] [99]. The interfaces are common in HV equipment for the reason that different dielectric materials are inevitably used for the insulation system [65]. There are two types of interfaces: the chemical interface (the crossed-linked interface) and the physical interface (EPR and XLPE attaching using external mechanical stress). The physical interface could be regarded as the potential barrier preventing charge movement and leading to charge accumulation at the interface. Two reasons could account for this phenomenon. According to the Maxwell-Wagner theory [100], the interfacial charge forms where a discontinuity of the ratio between conductivity and permittivity occurs. Moreover, the charge accumulation at the interface is influenced by the specific characteristics of the interface itself. e.g. considering the presence of broken bonds and fold chains at the interface, the traps originated from surface states can lead to the formation of space charge at the interface [67].

Traditionally, the electric field in multilayers samples is calculated based on the Maxwell-Wagner theory. Maxwell-Wagner only works for the linear materials, which means the conductivity of insulation materials is proportional to external electric field. In reality, the insulation materials are non-linear, especially subject to high electric fields. Therefore, the space charge measurement results defy part of the Maxwell-Wagner theory [67] [68] [101]. The main difference between the electric field caused by space charge density and the Maxwell-Wagner theory can be attributed to the surface states. The effect of surface states on the interface charge formation is clearly demonstrated in [67] where space charge was observed in two layers of LDPE films. Considering imperfectly bonded different dielectric materials caused by either finite surface roughness or insufficient interfacial pressure [102], the space charge measurement results should be added to evaluate the electric field of the multilayers dielectric materials.

It is difficult to measure the space charge of multilayers and thick oil and PB directly due to the

acoustic wave attenuation, dispersion and reflection of the acoustic wave propagation in the samples. Therefore, the different thickness combination of the oil and PB are measured to investigate the thickness influence on the space charge behaviour. A methodology that allows one to extend the space charge from the thinner oil and PB to thicker ones is proposed so that the multilayers thick samples space charge results can be estimated.

In this section, the multilayers and thickness of oil and PB effect on the space charge dynamics will be presented. A methodology that allows one to extend the space charge from thinner samples to thicker samples is proposed. With the further interpolation of the estimated space charge results in COMSOL software, the multilayers electric field based on space charge measurement is compared to the Maxwell-Wagner theory, with the emphasis on the electric field after the PR operation.

7.4.1 The different thickness of the space charge behaviour under ambient temperature

To investigate the thickness effect on the space charge behaviour, the different combination thickness of oil and PB space charge was measured using the PEA system and the thickness details are shown in Table 7-9. The samples preparation procedures are the same as detailed in Chapter 5. Two layers oil and PB space charge are measured under the electric field of 10 kV/mm. The voltage application time is two hours. After turning off the external DC voltage supply, the decay process starts and lasts for around one hour.

Table 7-9: The different thickness of oil and PB

Number	Thickness of PB	Thickness of oil
1	0.5 mm	0.25, 0.3, 0.4, 0.5, 0.6 mm
2	0.3 mm	0.3, 0.4, 0.5, 0.6, 0.7 mm

Figure 7-19 (a) indicates the space charge of 0.3 mm oil and 0.3 mm PB under the electric field of 10 kV/mm. Homocharge injection is obvious for two layers oil and PB. The injected positive charge accumulates adjacent to the anode. The negative charge migrates across the oil and accumulates at the oil and PB interface, leading to a decreased electric field in oil.

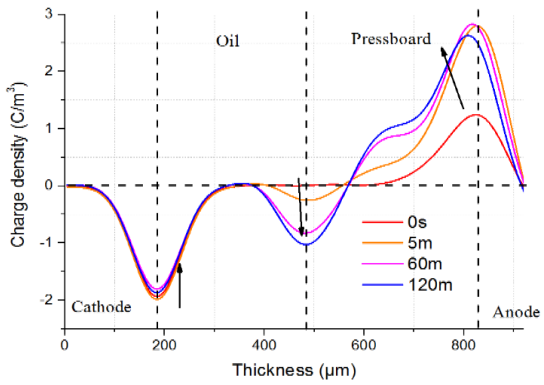

(a) Fresh 0.3 mm PB and 0.3 mm oil

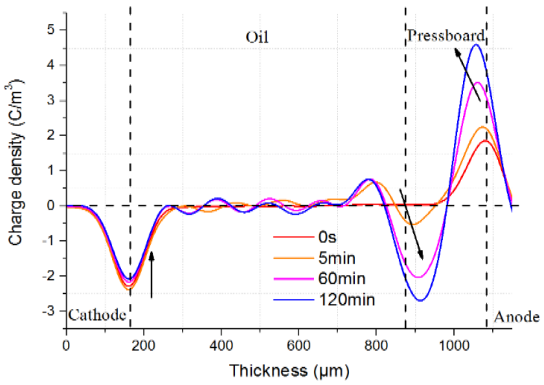

(b) Fresh 0.3 mm PB and 0.6 mm oil

Figure 7-19: Space charge distribution of (a) fresh 0.3 mm PB 0.3 mm oil and (b) fresh 0.3 mm PB and 0.6 mm oil under 10 kV/mm.

Figure 7-19 (b) indicates the space charge of 0.6 mm oil and 0.3 mm PB under an electric field of 10 kV/mm. Compared to Figure 7-19 (a), the increase of the oil thickness could increase the negative interfacial charge density, which is -2.6 C/m^3 under 10 kV/mm compared to around 1.03 C/m^3 in Figure 7-19 (a).

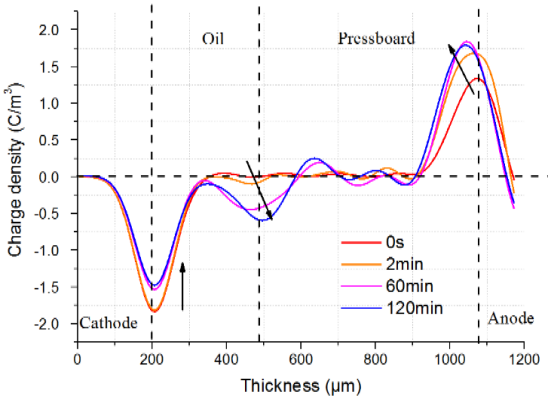

(a) Fresh 0.5 mm PB and 0.3 mm oil

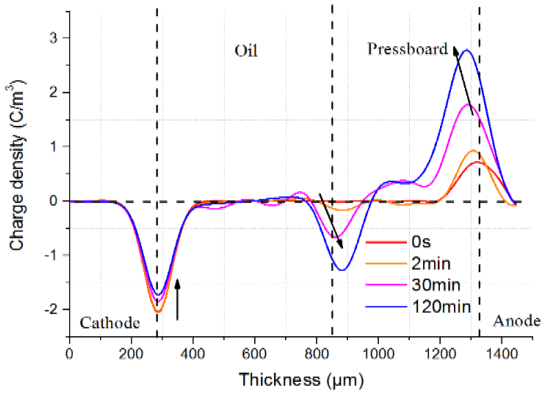

(b) Fresh 0.5 mm PB and 0.5 mm oil

Figure 7-20: Space charge distribution of (a) fresh 0.5 mm PB and 0.3 mm oil and (b) fresh 0.5 mm PB and 0.5 mm oil under 10 kV/mm.

Figure 7-20 (a) shows the space charge of 0.3 mm oil and 0.5 mm PB under an electric field of 10 kV/mm. Compared to Figure 7-19 (a), the increase of the PB thickness seems to facilitate the positive charge injection and lead to less negative charge accumulation at the interface. The negative interfacial charge density is around 0.6 C/m^3, which is less than 1.03 C/m^3, shown in Figure 7-19 (a).

Figure 7-20 (b) shows the space charge of 0.5 mm oil and 0.5 mm PB under the electric field of 10 kV/mm. The space charge magnitude in Figure 7-20 (b) is similar to Figure 7-19 (a). The

interfacial charge density is around 1.27 C/m^3 in Figure 7-20 (b).

The comparison of Figure 7-19 (a) to Figure 7-20 (b) shows that the increase of the oil thickness increases the negative interfacial charge density while the increase of the PB thickness can decrease the negative interfacial charge density. Several reasons may account for the above observations.

Based on equation (2-16), the steady-state electric field of PB in two layers oil and PB samples can be deduced, as shown in Equation (7-12):

$$E_{\mathrm{op}} = \frac{R_{\mathrm{op}} V}{(R_{\mathrm{op}} + R_{\mathrm{oil}}) d_{\mathrm{op}}} = \frac{V}{d_{\mathrm{op}} + \frac{\rho_{\mathrm{oil}}}{\rho_{\mathrm{op}}} d_{\mathrm{oil}}} \approx E_{\mathrm{av}} (\frac{d_{\mathrm{oil}}}{d_{\mathrm{op}}} + 1) \tag{7-12}$$

where ρ_{oil} and ρ_{op} are resistivities of oil and PB respectively, and E_{av} is the average electric field. Based on Table 7-3 as the second item $\frac{\rho_{\mathrm{oil}}}{\rho_{\mathrm{op}}} d_{\mathrm{oil}}$ is smaller compared to d_{op}, the simplified equation is shown in equation (7-12). Equation (7-12) shows that with the fixed thickness of oil d_{oil} and external electric field E_{av}, the electric field of the PB E_{op} decreases with the increase of the thickness of PB d_{op}. It reflects that the magnitude of the interfacial charge density decreases with the increase of the PB thickness on the condition that there is an unchanged thickness of the oil and external average electric field. Based on equation (7-4), the interfacial charge density can be deduced, as shown in equation (7-13):

$$\sigma = \left(\frac{\varepsilon_{\mathrm{oil}} \gamma_{\mathrm{op}} - \varepsilon_{\mathrm{op}} \gamma_{\mathrm{oil}}}{d_{\mathrm{oil}} \gamma_{\mathrm{op}} + d_{\mathrm{op}} \gamma_{\mathrm{oil}}} \right) V = (\varepsilon_{\mathrm{oil}} - \varepsilon_{\mathrm{op}} \frac{\rho_{\mathrm{op}}}{\rho_{\mathrm{oil}}}) E_{\mathrm{av}} \left(\frac{1 + \frac{d_{\mathrm{oil}}}{d_{\mathrm{op}}}}{\frac{\rho_{\mathrm{op}}}{\rho_{\mathrm{oil}}} + \frac{d_{\mathrm{oil}}}{d_{\mathrm{op}}}} \right) \tag{7-13}$$

It also shows that the increased thickness of PB leads to the decrease of the interfacial charge density.

The space charge trapping and de-trapping rate are correlated with the sample thickness. It is known that the DC dielectric strength of the solid insulation materials decreases with the increased sample thickness [103]. It shows that the trapping rate of the space charge is higher compared to the de-trapping rate of space charge with the increased sample thickness. Therefore, the increased thickness of PB enhances the trapping rate of positive charge and neutralises the negative interfacial charge density at the oil PB interface [67].

Based on the above discussion, it shows that the increased thickness of oil increases the negative interfacial charge density while the increased thickness of PB decreases the negative interfacial charge density. These two opposite trends allow us to hypothesise that the same thickness ratio of the oil and PB leads to the similar space charge distribution under the same electric field.

To verify this hypothesis, the interfacial charge and maximum electric field are further investigated based on both the Maxwell-Wagner theory and space charge results. The interfacial charge of oil and PB can be calculated based on the equation below:

$$Q(t) = \left(\frac{\varepsilon_{\text{oil}}\gamma_{\text{op}} - \varepsilon_{\text{op}}\gamma_{\text{oil}}}{d_{\text{oil}}\gamma_{\text{op}} + d_{\text{op}}\gamma_{\text{oil}}}\right) VS\left(1 - e^{-\frac{t}{\tau}}\right) \tag{7-14}$$

where $Q(t)$ (C) is surface charge and S is the surface area of the electrode. Figure 7-21 shows the absolute value of the interfacial charge density and the maximum electric field within the PB based on the Maxwell-Wagner theory.

Figure 7-21 (a) shows the absolute value of the interfacial charge density $Q(t)$ versus the different thickness of the oil layer. Figure 7-21 (a) shows that the surface charge at the oil PB interface increases with the increased oil thickness and decreases with the increased PB thickness. Moreover, the interfacial charge is the same with the same thickness ratio between the oil and PB.

Figure 7-21 (b) shows the maximum electric field of the PB with different thickness combination between the oil and PB. If the PB thickness is fixed, it shows that the maximum electric field of the PB increases with the increased oil thickness. With the unchanged thickness of oil, the maximum electric field of the PB decreases with the increased PB thickness. The comparison of Figure 7-21 (a) and Figure 7-21 (b) illustrates that the increased interfacial charge leads to the increased maximum electric field in the PB.

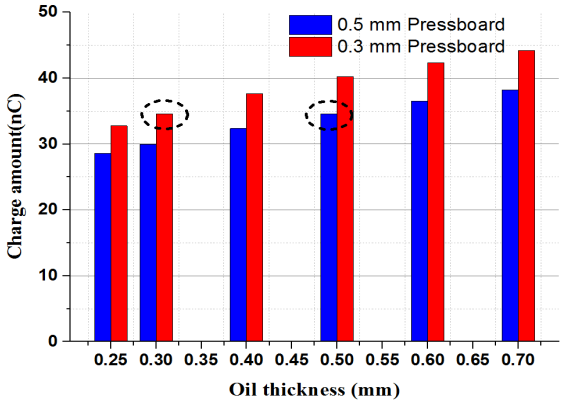

(a) Interfacial charge

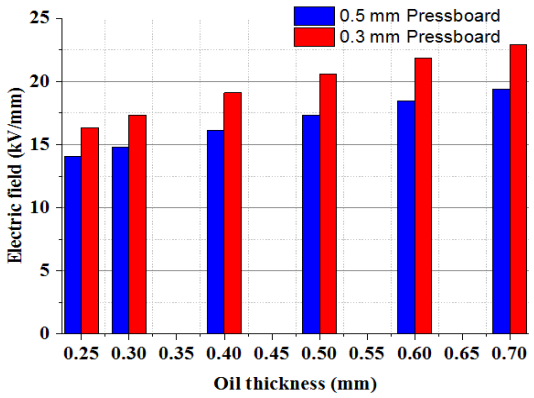

(b) Electric field of OP

Figure 7-21: (a) The interfacial charge and (b) the electric field for two layers oil and PB with the different thickness of the oil based on the Maxwell-Wagner theory.

The interfacial charge amount $q(t)$ can also be calculated from equation (7-15) based on the space charge results:

$$q(t) = \int_{d_2}^{d_1} |\rho(x,t)|Sdx \tag{7-15}$$

where d_1 and d_2 is the start and end point of the interfacial charge area.

Figure 7-22 (a) and Figure 7-22 (b) shows the absolute value of the interfacial charge density and the maximum electric field within the PB based on the space charge results. When comparing Figure 7-21 to Figure 7-22, the same trend has been observed, namely that the interfacial charge and maximum electric field increase with the increased oil thickness. Moreover, the interface charge and the electric field is lower compared to that from the Maxwell-Wagner theory. This may relate to the fresh oil and PB, which could lead to less space charge injection and relative lower electric field enhancement. In Figure 7-22 (a), it also reflects that the interfacial charge is approximately the same with the same thickness ratio between the oil and PB.

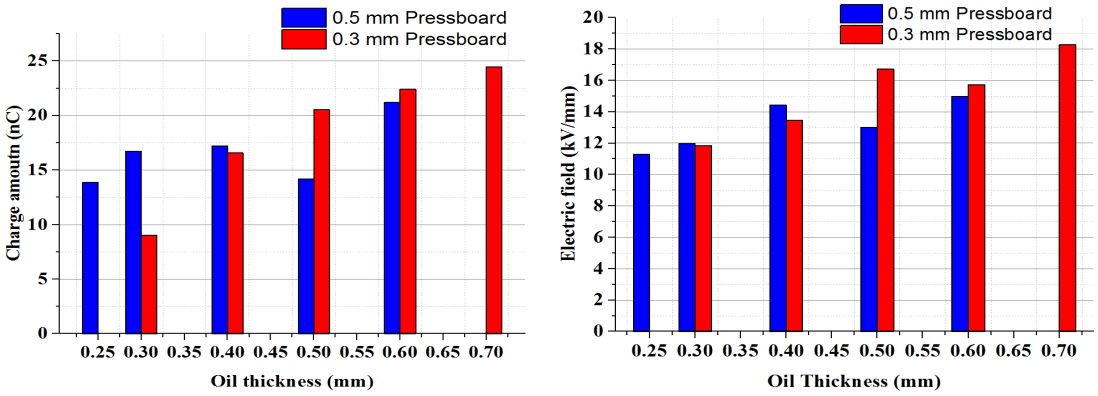

(a) Interfacial charge (b) Electric field of OP

Figure 7-22: (a) The interfacial charge and (b) the electric field for two layers oil and PB with different thickness of oil based on space charge measurement.

The interfacial negative charge is also summarised to evaluate the different thickness of the space charge results. Figure 7-23 (a) shows the transient 0 s and steady state 120 min space charge results of two layers 0.3 mm oil and 0.3 mm PB under 10 kV/mm. Figure 7-23 (b) shows the subtraction of the steady and transient state space charge to remove the capacitive charge on the electrodes. In Figure 7-23 (b), to evaluate the space charge behaviour, a C/m^3, b C/m^3 and c C/m^3 is the maximum charge density on the cathode, interface and anode. The d C/m^3, e C/m^3 and f C/m^3 is the sum of the charge density on the cathode, interface and anode. The g μm is the distance of the anode peak movement due to charge injection.

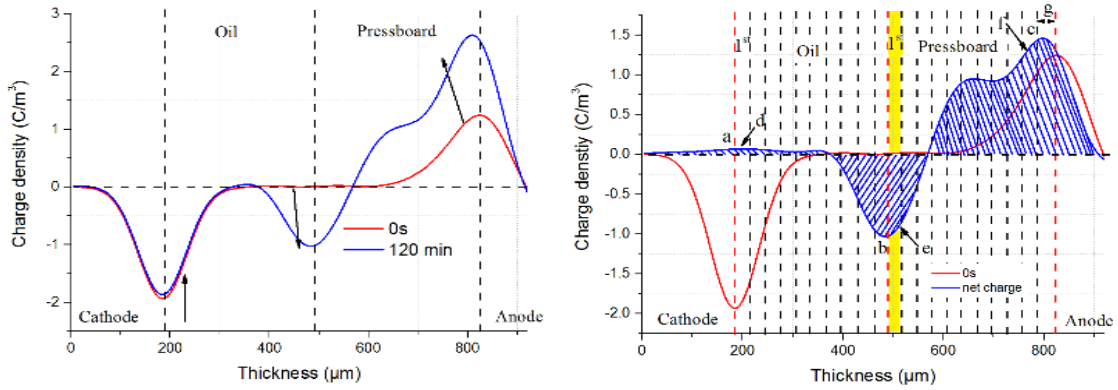

(a) 0 s and 120 min (b) After subtraction

Figure 7-23: Space charge of two layers 0.3 mm oil and 0.3 mm PB under an electric field of 10 kV/mm; (b) after the subtraction under 10 kV/mm.

The summary results of different thickness combination of oil and PB are shown in Table 7-10. In Table 7-10, with the comparison of a^1, b^1, c^1 and a^4, b^4, c^4, the space charge density is quite similar when the ratios of oil and PB is the same, as compared to other groups. Furthermore, the sum of d^1 and e^1, d^2 and e^2, d^3 and e^3, d^4 and e^4 is -19.995 C/m^3, -64.919 C/m^3, -6.917 C/m^3 and -26.256 C/m^3, respectively. Among them, the sum of d^1 and e^1 -19.995 C/m^3 and d^4 and e^4 -26.256 C/m^3 are approximately similar, showing that the maximum electric field in PB is approximately the same.

Table 7-10: Space charge behaviour for various oil and paper thickness ratios

	Oil 0.3 (mm)				**Oil 0.5 (mm)**			
Paper 0.3 (mm)	a^1	0.068	d^1	3.054	a^2	0.201	d^2	6.329
	b^1	-1.033	e^1	-23.049	b^2	-2.556	e^2	-71.248
	c^1	1.459	f^1	59.552	c^2	4.027	f^2	112.1
			g^1	24.934			g^2	55.781
Paper 0.5 (mm)	a^3	0.359	d^3	8.765	a^4	0.321	d^4	7.229
	b^3	-0.600	e^3	-15.682	b^4	-1.268	e^4	-33.485
	c^3	0.793	f^3	16.150	c^4	2.206	f^4	89.365
			g^3	66.964			g^4	44.703

Based on the above discussion, it verifies the hypothesis that the interfacial charge is approximately the same with the same thickness ratio between the oil and PB. It will allow one to interpolate the space charge from the thinner samples to multilayer thicker samples for the electric field estimation.

7.4.2 The methodology of the space charge interpolation into multilayers of oil and PB in the COMSOL software

The interpolation of space charge methodology, shown in Figure 7-24, will contain the following parts: (i) Divide the model based on different thickness ratios sections; (ii) Summarise the interfacial charge based on different thickness ratios; (iii) Estimate the interfacial charge with different thickness ratios; (iv) Interpolate the space charge into the model; and (v) Compute the electric field distribution.

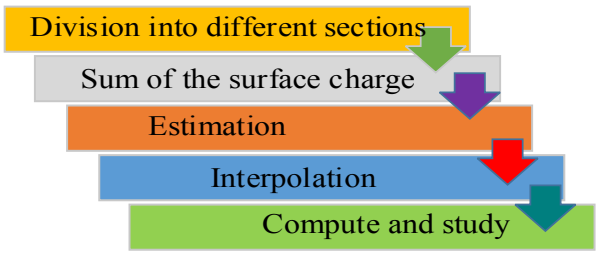

Figure 7-24: The space charge interpolation method into multilayers oil and PB.

The multilayers consisting of four and six layers structure model of oil and PB, which are proposed by the CIGRE working group A2/D1.41, is shown in Figure 7-25. The aim of the simple four and six layers model is to mimic the part of the electric field in the converter transformer. Considering the thick and multilayers structure of the oil and PB, it is difficult to measure the space charge directly. Therefore, the new methodology of interpolating the space charge into the model will be described in detail here.

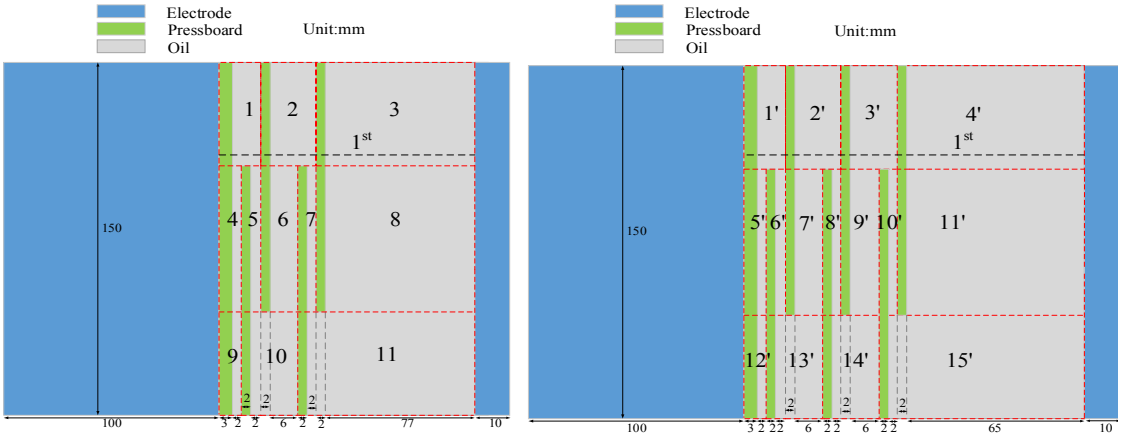

(a) Four layers (b) Six layers

Figure 7-25: Configuration of four and six layers oil and PB.

Firstly, the thickness of each oil and PB layers are shown in Figure 7-25. The four and six layers oil and PB are divided into different thickness ratio sections based on the equation (7-16):

$$Ratio = \frac{d_{op}}{d_{oil}} \tag{7-16}$$

Table 7-11 shows that the four and six layers model are divided into eleven and fifteen thickness ratios sections, separately.

Table 7-11: The different thickness ratio sections of four and six layers

Number	Ratio	Number	Ratio
1	1:2	1'	1:2
2,10	1:5	2',3',13',14'	1:5
3,8	1:38.5	4',11'	1:32.5
4,9	3:2	5'12'	3:2
5,7	1:1	6'8'10'	1:1
6	1:3	7'9'	1:3
11	1:40.5	15'	1:34.5

Secondly, the interfacial charge density is summarised for the interfacial area for different thickness ratios of the samples. The interfacial charge density versus the different thickness ratios is presented in Table 7-12. Figure 7-26 indicates the relationship between the interfacial charge density versus different thickness ratios varied from 1:0.5 to 1:2.333.

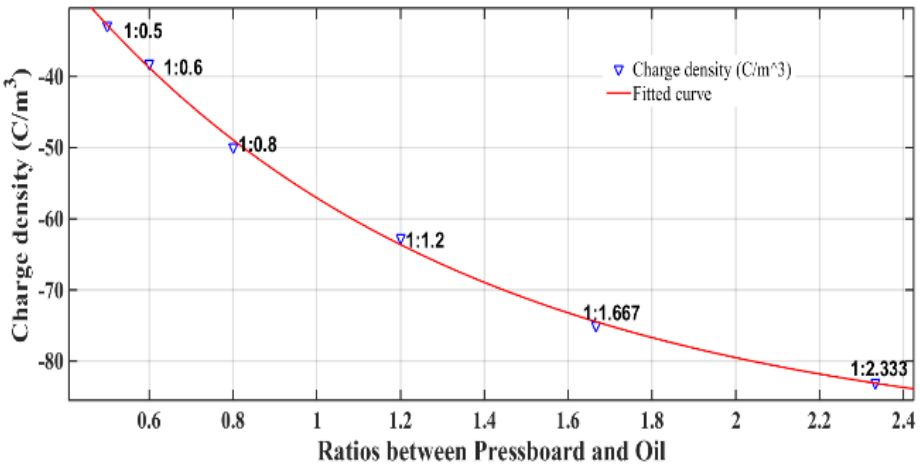

Figure 7-26: The interfacial charge density versus different thickness ratios between the PB and oil.

Thirdly, the interfacial charge density versus sample thickness can be represented using the curve

fitting function in the MATLAB. The space charge density versus the sample thickness ratios is represented using two exponential functions. Based on equation (7-17), the different interfacial charge density could be calculated, and the results are shown in Table 7-12. Moreover, the estimated interfacial charge densities are shown in Figure 7-27.

$$f(x) = -87.91\exp(0.0116x) + 97.1\exp(-1.114x) \quad (7\text{-}17)$$

Table 7-12: The interfacial charge density versus the different thickness ratios

Ratios	1:0.667	1:1	1:2	1:3	1:5	1:32.5	1:34.5	1:38.5	1:40.5
Charge density (C/m^3)	-42.41	-57.06	-79.51	-83.07	-87.59	-92.79	-131.17	-137.4	-140.6

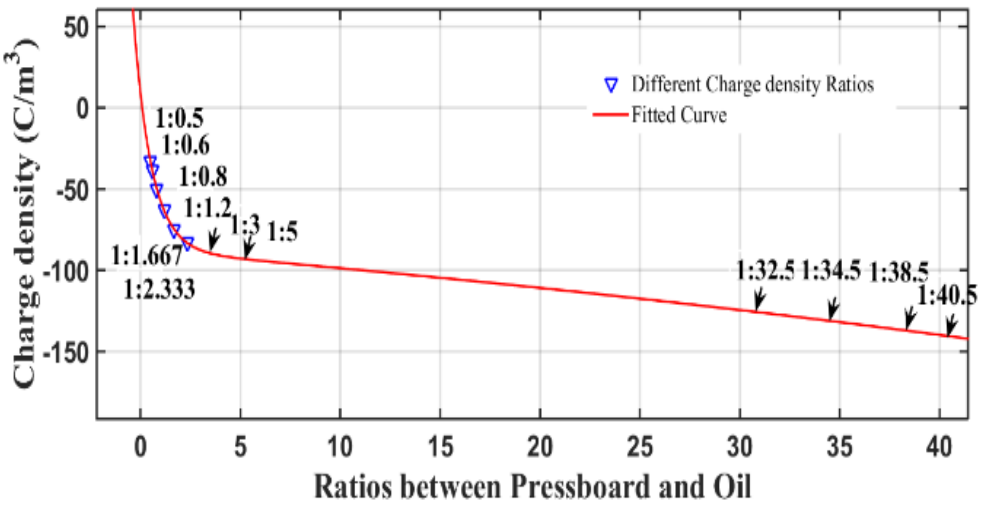

Figure 7-27: The estimated interfacial charge density versus different thickness ratios between the PB and oil.

Fourthly, to interpolate the space charge into thick multilayers oil and oil-impregnated PB, the ratio between different interfacial charge density can be calculated using equation (7-18):

$$\text{Ratio} = \frac{q_1}{q_2} \quad (7\text{-}18)$$

where q_1 represents the estimated interfacial charge and q_2 indicates the measured interfacial charge. Then, the ratio should multiply the existing equations representing space charge versus time of each layer, and the space charge is interpolated into the multilayers oil and PB model in COMSOL based on the methodology described in section 7.3.1.

Take the space charge extended from the thickness ratio of 1:2 to 1:5 as an example, based on space charge result of 0.3 mm oil and 0.6 mm PB, the relative interfacial charge is -79.51 C/m^3 (shown in Table 7-12) with the thickness ratio of 1:2. Based on equation (7-18), the ratio of 1.1 can be acquired after dividing -87.59 C/m^3 and -79.51 C/m^3. Then, this ratio should be used to multiply the equations representing space charge versus time with a ratio of 1:2, and the space charge can therefore be extended from the thickness ratio of 1:2 to 1:5.

The 4 layers section number 9, 10, 11 shown in Figure 7-25 (a) is selected as an example. After the interpolation of space charge into the model, the space charge distribution is shown in Figure 7-28 (a) below; the thinness below 20000 μm of the space charge result in Figure 7-28 (a) is enlarged shown in Figure 7-28 (b).

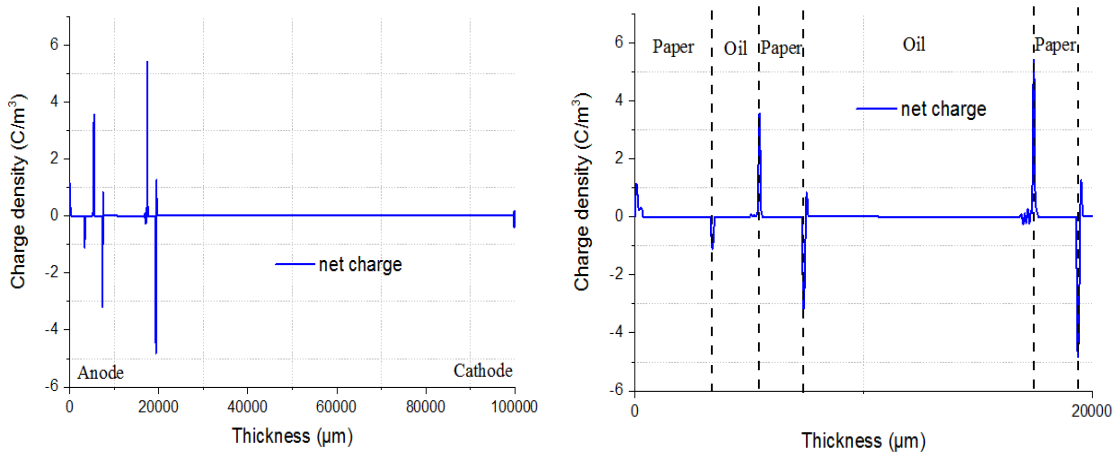

(a) Whole space charge (b) Part of space charge

Figure 7-28: (a) The whole and (b) part of space charge in multilayers oil and PB.

Finally, the electrostatic model is selected to calculate the time dependent electric field distribution of four layers oil and PB. The geometry of four layers oil and PB geometry is shown in Figure 7-25. The applied electric field is shown in Figure 7-29. As the samples have the thickness of 100 mm, 1000 kV of the PR voltage is applied on the insulation samples. In mesh level setting, the "extremely fine" level of mesh is selected to calculate the electric field and different PR time effect on the electric field will be simulated later.

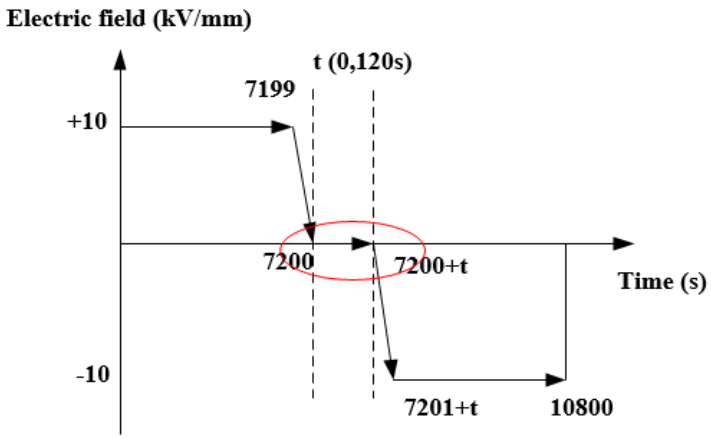

Figure 7-29: The PR operation voltage waveform.

The electric field distribution of four layers oil and PB are shown in Figure 7-30. The electric field of the PB increases from the anode to the cathode while the electric field of the oil decreases from the anode to the cathode.

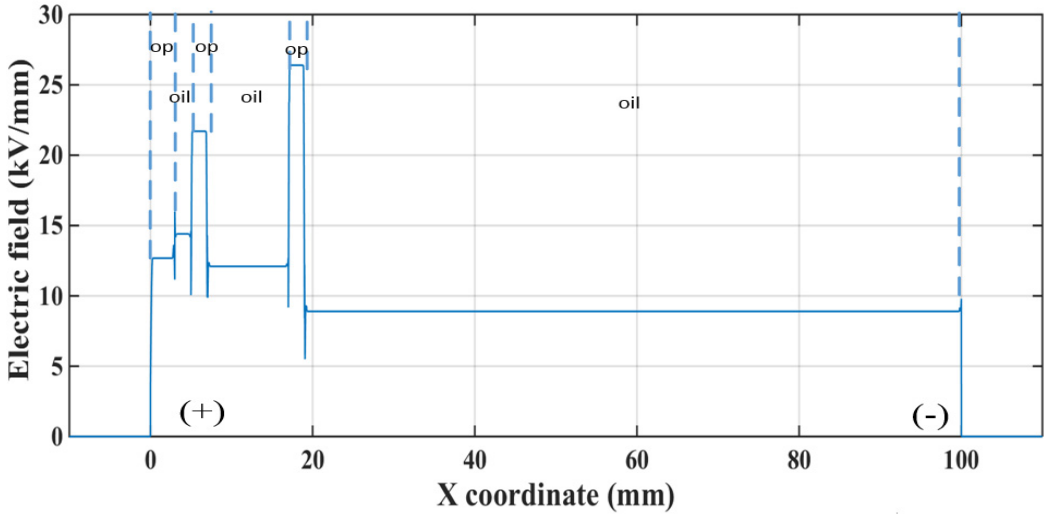

Figure 7-30: The electric field simulation of multilayers oil and PB caused by the space charge density.

Based on the above discussion, the following electric field simulation is based on the section number 1, 2 and 3 shown in Figure 7-25 (a) and 1', 2', 3' and 4' shown in Figure 7-25 (b). This is due to the increased thickness of the oil gap, which leads to the higher interfacial charge density and higher electric field enhancement of the oil after the PR operation. It could be verified by the following electric field simulation.

7.4.3 The transient and steady state electric field caused by the space charge of multilayers oil and PB

After the space charge interpolation into the four and six layers model, the electric field based on the space charge can be simulated with the emphasis on the electric field after the PR operation. Moreover, four and six layers electric field based on space charge is compared to the electric field based on the Maxwell-Wagner theory.

Figure 7-31 (a) and Figure 7-31 (b) shows four and six layers of steady state electric field based on the Maxwell-Wagner theory. The electric field of the PB is higher compared to that of the oil due to the higher resistivity of PB. Moreover, comparing Figure 7-31 (a) to Figure 7-31 (b), it indicates that the increased layers can decrease the electric field of the PB from 26.5 kV/mm to 25.9 kV/mm in PB and from 9.1 kV/mm to 8.9 kV/mm in the oil.

In order to explain this phenomenon, the steady state electric field of oil and PB could be calculated using the following equation (7-19) and (7-20), where M represents the finite layer (M≥ 4).

$$\begin{cases} \gamma_1 E_1 = \gamma_2 E_2 = \gamma_3 E_3 = \gamma_4 E_4 = \gamma_{\mathrm{M}} E_{\mathrm{M}} \\ E_1 d_1 + E_2 d_2 + E_3 d_3 + E_4 d_4 + E_{\mathrm{M}} d_{\mathrm{M}} = V \end{cases} \tag{7-19}$$

$$E_{\mathrm{M}} = \frac{V}{\gamma_{\mathrm{M}}\left(\frac{d_1}{\gamma_1} + \frac{d_2}{\gamma_2} + \frac{d_3}{\gamma_3} + \frac{d_4}{\gamma_4} + \frac{d_{\mathrm{M}}}{\gamma_{\mathrm{M}}}\right)} \tag{7-20}$$

In equations (7-19) and (7-20), if it is assumed that there are only two different samples with conductivities γ_1 and γ_2 and samples thickness a and b respectively, the above equation (7-20) can be simplified into equations (7-21) or (7-22):

$$E_{\mathrm{M}} = \frac{E_{\mathrm{av}} d}{\frac{\gamma_{\mathrm{M}}}{\gamma_1 \gamma_2}(\gamma_1 d + (\gamma_2 - \gamma_1) a)} \tag{7-21}$$

$$E_{\mathrm{M}} = \frac{E_{\mathrm{av}} d}{\frac{\gamma_{\mathrm{M}}}{\gamma_1 \gamma_2}(\gamma_2 d + (\gamma_1 - \gamma_2) b)} \tag{7-22}$$

where the γ_1 and γ_2 are conductivity of oil and PB, and γ_1 is higher than γ_2. The a and b represents the thickness of oil and PB. Moreover, d is the fixed sample thickness and E_{av} is the external electric field.

Equations (7-21) and (7-22) indicate that with the increased thickness of the oil a, the electric field of each layer can increase based on equation (7-21) while with the increase of the PB thickness b, each layer of either the oil or PB electric field can decrease based on equation (7-22).

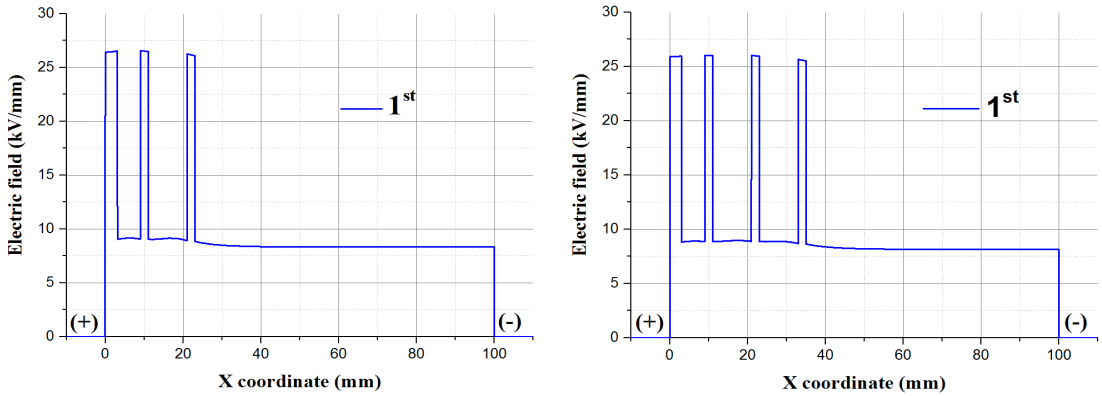

(a) Four layers (b) Six layers

Figure 7-31: Electric field of four and six layers oil and PB caused by the Maxwell-Wagner theory for 1st position line.

Figure 7-32 (a) and Figure 7-32 (b) show the four and six layers oil and PB electric field after the PR at the operation time of 10 s based on the Maxwell-Wagner theory. The transient electric field of the oil is correlated with the permittivity. The lower permittivity of the oil leads to the higher transient electric field compared to that of the PB. Comparing Figure 7-31 (a) and (b) to Figure 7-32 (a) and (b). It is clear that the transient electric field of oil is higher than that under the steady state electric field.

Comparing Figure 7-32 (a) and Figure 7-32 (b), it can be seen that the transient electric field of the oil decreases with the increased thickness of the oil. It could be explained by the equations (7-23) and (7-24) below, where ε_1 represents permittivity of oil and ε_2 is the PB with ε_2 higher than ε_1. It shows that the transient electric field of each layer decreases with increased oil thickness based on equation (7-23). Moreover, the transient electric field of each layer increases with the increased thickness of PB based on equation (7-24).

$$E_{\mathrm{M}} = \frac{E_{\mathrm{av}} d}{\frac{\varepsilon_{\mathrm{M}}}{\varepsilon_1 \varepsilon_2}(\varepsilon_1 d + (\varepsilon_2 - \varepsilon_1) a)} \tag{7-23}$$

$$E_{\mathrm{M}} = \frac{E_{\mathrm{av}} d}{\frac{\varepsilon_{\mathrm{M}}}{\varepsilon_1 \varepsilon_2}(\varepsilon_2 d + (\varepsilon_1 - \varepsilon_2) b)} \tag{7-24}$$

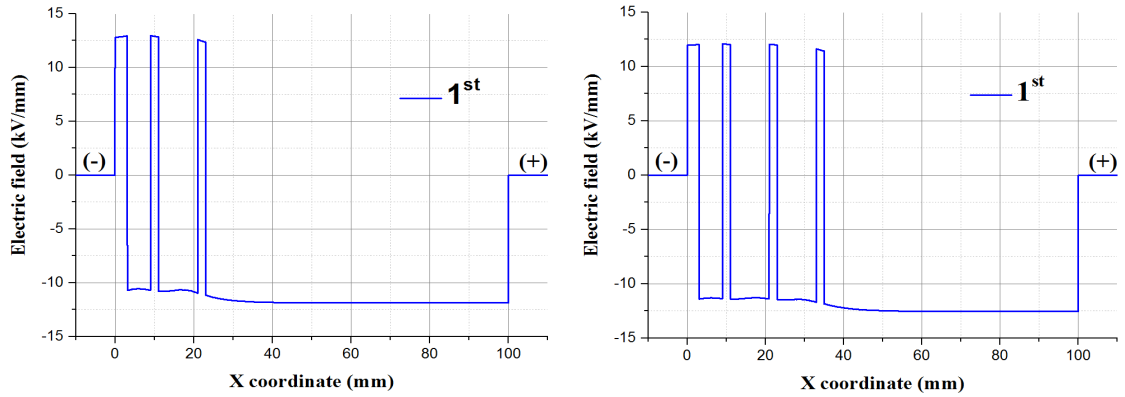

(a) Four layers (b) Six layers

Figure 7-32: Electric field of four and six layers of oil and PB caused by the 1st position line caused by the Maxwell-Wagner theory after the PR time of 10 s.

Figure 7-33 (a) and (b) show a steady state electric field based on the space charge. It shows that the electric field of the PB is enhanced while the electric field of the oil is decreased compared to the external average electric field. This is due to the charge in the PB, which creates the electric field in the same direction as the external electric field. However, the charge in the oil can generate the electric in the opposite direction to the external electric field, leading to the decrease of the electric field in the oil.

Moreover, there is the electric field gradient in four and six layers oil and PB based on the space charge. In Figure 7-33 (a) and (b), the electric field of the PB increases and the oil decreases from the anode to the cathode. This could be explained using the schematic diagram in Figure 7-34. Due to the different thickness ratios of the oil and PB, a large amount of space charge in PB near the cathode increases the electric field in the PB and decreases the electric field in the oil. Therefore, the electric field gradient exists in the thick multilayers oil and PB samples.

When comparing the electric field for four and six layers caused by space charge shown in Figure 7-33 (a) and (b), there is no significant electric field decrease with the increase of the layers caused by the space charge.

A comparison of Figure 7-33 (a) and Figure 7-30 indicates the minimum electric field of the oil gap is lower for Figure 7-33 (a). This results from the higher interfacial charge density due to higher oil to PB thickness ratios, seen when comparing section 1 and section 9 in Figure 7-25.

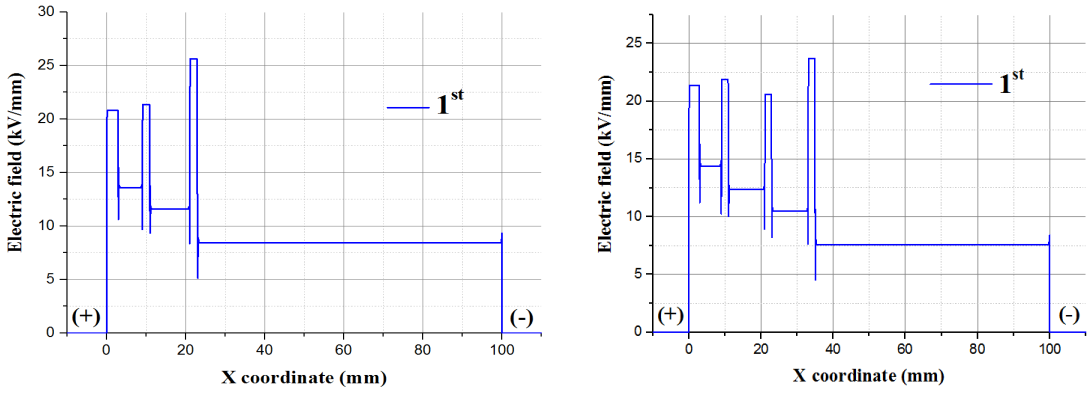

(a) Four layers (b) Six layers

Figure 7-33: Electric field of four and six layers of oil and PB caused by the 1st position line caused by the space charge.

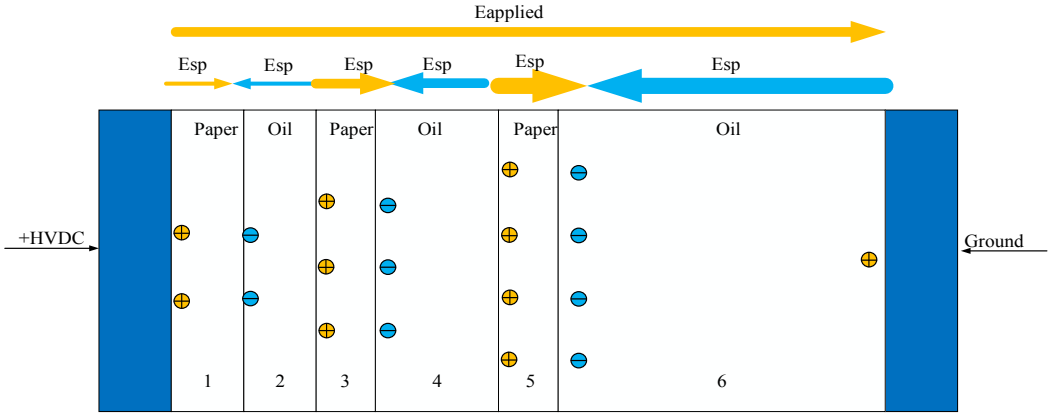

Figure 7-34: Schematic diagram indicating the multilayers oil and PB space charge distribution.

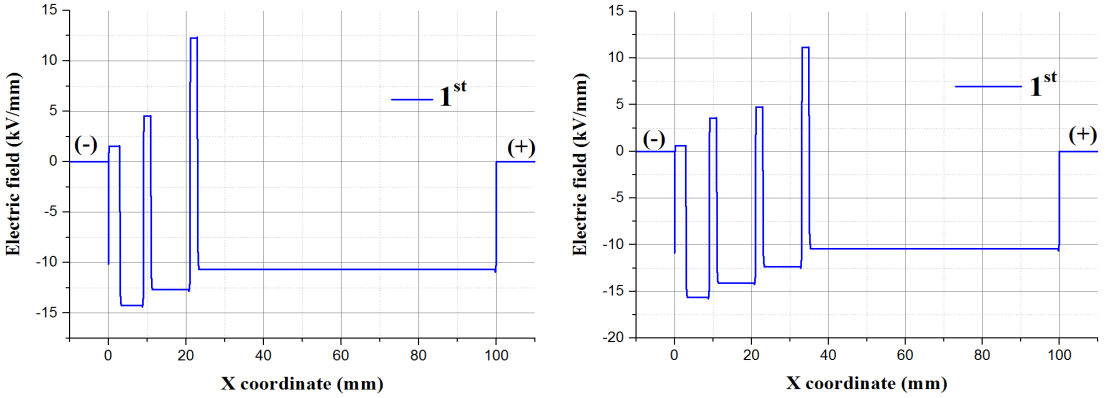

(a) Four layers (b) Six layers

Figure 7-35: The four and six layers electric field of multilayers oil and PB caused by the 1st position line after the PR time of 10 s.

Figure 7-35 (a) and (b) show the electric field of multilayers for oil and PB after the PR operation

time of 10 s caused by the space charge. It shows that the electric field of the oil is enhanced while the electric field in the PB is decreased after the PR operation. The overall electric field consists of the electric field caused by both external applied voltage and space charge, shown in equation (7-25). The heterocharges within the oil could be converted to the homocharges after the PR, which could lead to the electric field enhancement within the oil. However, the homocharges in the previous stage of voltage application within the PB could be viewed as the heterocharges after PR operation, leading to the electric field decrease within the PB.

$$E_{\text{total}} = E_{\text{applied}} + E_{\text{sc}} \tag{7-25}$$

From Figure 7-35 (a) and (b), there is the electric field gradient within multilayers oil and PB after the PR operation. After the PR operation, the electric field of the oil decreases from the cathode to the anode. However, the electric field of the PB increases from the cathode to the anode. This could be explained using the schematic diagram in Figure 7-36. Considering different thickness ratios of the oil and PB, a significant amount of residual space charge within the PB creates the electric field with the opposite direction compared to the external electric field. This leads to the electric field of the PB increase from cathode to anode, resulting the electric field gradient across the multilayers samples.

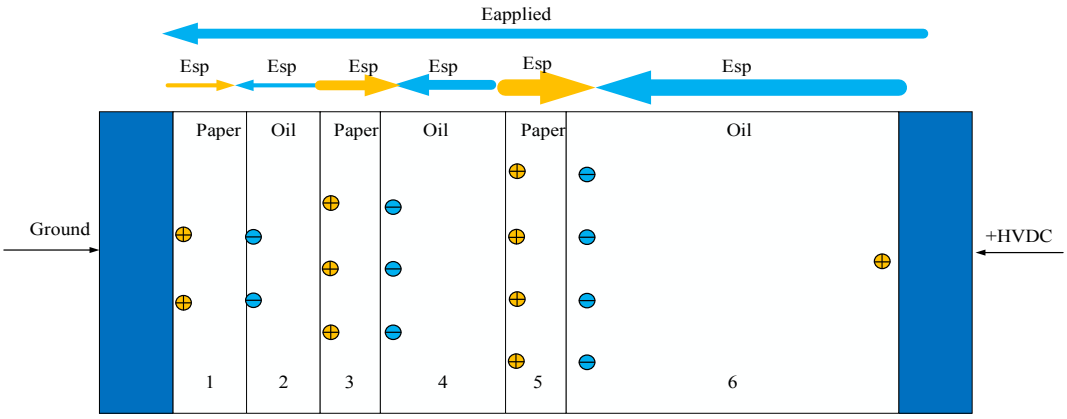

Figure 7-36: Schematic diagram indicates multilayers oil and PB space charge distribution after the PR operation.

Figure 7-37 shows the summary of the electric field calculated by either space charge or the Maxwell-Wagner theory for both four and six layers of the oil layer after different PR operation time. The simulation results show that the electric field of oil caused by the space charge is higher compared to that from the Maxwell-Wagner theory. Moreover, after the PR operation, for the 1st line in four and six layers of oil and pressboard shown in Figure 7-25 (a) and Figure 7-25 (b), the electric field of the oil for six layers is higher compared to four layers calculated by from both

space charge and the Maxwell-Wagner theory.

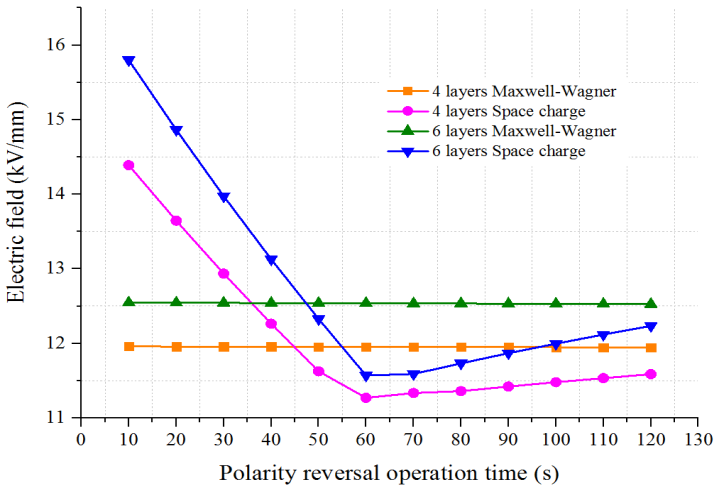

Figure 7-37: Summary of the electric field of the oil for four and six layers caused by the space charge and Maxwell-Wagner theory for different PR time.

The current standard PR operation time is 2 minutes [57]. The transient electric field of oil after PR is lower than its steady state electric field. The transient electric field of oil is -14.4 kV/mm and -15.8 kV/mm for four and six layers after the PR operation time of 10 s. The steady state electric field of oil in four and six layers is 15.4 kV/mm and 16.2 kV/mm, respectively. Moreover, in Figure 7-37, it shows that after the PR time of 60 s, the electric field caused by the space charge does not have the obvious decrease. These two factors show that the current 2 minutes PR operation time may be safely reduced for multilayers oil and pressboard under 10 kV/mm.

7.5 Summary

The space charge behaviour of oil and PB under a DC electric field is investigated via a PEA system. The influence of the ageing, different electric field, thickness, and multilayers on the space charge behaviour in oil and PB is investigated using an experimental approach. The space charge results are then interpolated into the COMSOL software for the electric field simulation with the emphasis on the electric field after the PR operation. The findings are presented as follows.

In terms of the two layers oil and PB, the electric field in oil and oil-impregnated PB insulation should be evaluated using the measured space charge rather than the conventional Maxwell-Wagner theory. After the PR operation, the difference between the electric field calculated using the measured space charge and the Maxwell-Wagner theory is higher for the fresh samples, while

this difference is smaller for the aged samples.

The higher conductivity of aged oil and oil-impregnated PB facilitates the charge migration from the oil/paper interface and charge injection from electrode towards the middle of the oil-impregnated PB. It results in significant electric field enhancement in PB. The mobile charge in oil could contribute to the space charge accumulation at the interface, leading to the charge dissipation on the electrode in oil.

For the aged oil and oil-impregnated PB, the higher applied electric field leads to a large amount of space charge injection, causing more electric field distortion within the oil-impregnated PB. For the fresh oil and oil-impregnated PB, the higher applied electric field could not lead to an obvious increase of charge injection.

After the PR operation, the homocharge injection within the oil impregnated PB can be viewed as heterocharge, which will enhance the electric field in the vicinity of the electrode and the interface between the oil and oil-impregnated PB.

In case of the aged oil and oil-impregnated PB, it leads to higher electric field distortion compared to the average electric field. The decrease in the electric field is higher after longer PR time. Moreover, for the fresh oil and oil-impregnated PB, the electric field distortion is less, and the electric field reduction is slow.

Comparing between the electric field after adding the space charge and the steady state electric field calculated by the Maxwell-Wagner theory, it suggests that the current two-minute PR operation time could be safely reduced for both fresh oil sample and aged oil sample below the electric field of 20 kV/mm.

In terms of the multilayers oil and PB, the increased PB thickness results in a decrease of the interfacial charge and an increased oil thickness leads to an increase of the interfacial charge density.

The same thickness ratio of the PB and oil could shows an approximately similar space charge distribution under the same external electric field. This could allow one to extend the space charge from thinner samples to thicker samples.

There is the electric field gradient for the electric field distribution within the oil and PB caused by space charge. The electric field of the PB increases from the anode to the cathode, and the electric field of the oil decrease from the anode to the cathode. Moreover, after the PR, the electric field of the oil decreases from the cathode to the anode, and the electric field of the PB increases from the cathode to the anode.

After PR, with the comparison of the electric field caused by the Maxwell-Wagner theory and the

space charge, it indicates that the electric field in the oil caused by the space charge is higher than that based on the Maxwell-Wagner theory. Moreover, it also shows that the PR operation time may be reduced from the current two minutes for multilayers oil and PB under the electric field of 10 kV/mm.

Chapter 8 Conclusions and future work

8.1 Conclusions

This dissertation concentrates on the research into temperature gradient effect on space charge in oil and PB materials under various electric stresses. The research work has been accomplished by a purpose-built PEA system. A space charge recovery methodology of oil and PB under a temperature gradient is proposed. The effect of the temperature effect and PR voltage on space charge dynamics of multilayer oil and PB has been investigated. The measured space charge is further interpolated into the COMOSL software to evaluate the electric field of two-layer oil and PB after PR. The model is also extended to four-layer and six-layer models to simulate the electric field after PR. Based on the fundamental research work, several conclusions can be drawn.

The purpose-built new PEA system has been successfully established and is capable of measuring thick oil and PB insulation up to 2 mm under the temperature gradient. The methodology of space charge recovery under a temperature gradient is successfully proposed. For one-layer sample under the temperature gradient, the attenuation and dispersion of the acoustic wave recovery are considered initially. A temperature effect on the magnitude of the charge density and horizontal thickness recovery in the one-layer sample is proposed. For multilayer samples of oil and PB, the attenuation, dispersion, and acoustic velocity of individual materials are calculated separately for space charge recovery. The new transfer function, including the different pulsed electric fields, acoustic wave generation, and transmission factors, are considered for the recovery of space charge in multilayer samples. A temperature effect on the magnitude of the charge density and horizontal thickness recovery in the multilayer sample method is proposed.

The influence of temperature gradient and multiple layers on the behaviour of space charge in oil and PB is studied using an experimental approach. The experiment results reveal that space charge dynamics under a temperature gradient differ compared to the dynamics at ambient temperature, which show that the temperature gradient plays an important role in the dynamics of space charge in oil and PB samples. For one-layer PB, a large amount of positive charge is injected from the high-temperature anode and leads to severe electric field enhancement near the cathode. For two-layer oil and PB, with 20°C at the bottom electrode, the electric field of the oil increases at temperature gradient and decreases at ambient temperature. For three layers, with 20°C at the bottom electrode, the maximum electric field occurs near the cathode under a temperature gradient and occurs close to the anode at ambient temperature. The higher temperature gradient leads to the higher electric field enhancement of multilayer oil and PB.

The PR effect on the space charge behaviour of multilayer oil and PB is also investigated. The

influence of factors including temperature gradient, voltage polarity, different PR duration, and multilayer samples related to the dynamics of space charge after PR has been revealed through an experimental approach. The experimental results reveal that for two layers oil and PB, after PR, the transient electric field in the oil reaches its maximum value at ambient temperature, while the steady-state electric field in the oil reaches its maximum value under a temperature gradient. The polarity effect shows that more charge accumulates at the interface under negative (-) voltage and leads to higher electric field enhancement with the voltage reversed from (-) to (+), especially under the temperature gradient. The electric field enhancement of oil decreases with the longer polarity reversal duration under the ambient temperature, while it increases under the temperature gradient. In terms of multilayer oil and PB, a 'mirror image charge' is seen in the comparison of the steady-state space charge with the voltage of different polarities under the temperature gradient while it cannot be seen under the ambient temperature. The electric field enhancement factor of the multilayers of oil and PB samples is higher compared to the two-layer samples under the same experiment conditions.

The influence of ageing, different electric fields, and thickness on space charge behaviour in oil and PB are investigated under ambient temperature. The space charge is further interpolated into COMSOL software to calculate the electric field with the emphasis on the electric field after the PR operation. The electric field is also calculated by the conventional Maxwell-Wagner theory for comparison. It is found that the difference between the electric field calculated using the space charge and the Maxwell-Wagner is higher for the fresh samples after PR, while the difference is smaller for the aged samples. By comparing the space charge of aged and fresh samples after the PR, it is found that the aged samples can facilitate the charge injection, which leads to a higher electric field enhancement factor of 52% compared to 26.5% of fresh samples under 20 kV/mm. Moreover, the space charge dissipates more quickly if the aged samples are compared to fresh ones for the decay process. The higher electric field leads to a large amount of charge injection for aged samples, while the higher electric field cannot lead to the obvious space charge increase for the fresh samples. In terms of the multilayer oil and PB, the increased PB thickness could decrease the interfacial charge, and an increased oil thickness could increase the interfacial charge density. The same thickness ratios of the PB and oil has been found to have an approximately similar space charge distribution under the same external electric field, which lays the foundation to extend the measured space charge from thinner samples to thicker ones. The COMOSOL model is extended to four and six layers, and the electric field distribution is calculated by the space charge in oil and PB. In general, the electric field of the PB increases from the anode to the cathode, and the electric field of the oil decreases from the anode to the cathode. Moreover, after the PR, the electric field of the oil decreases from the cathode to the anode, and the electric field of the PB increases from the cathode to the anode. After the PR, comparison of the electric field caused

by the Maxwell-Wagner theory and the space charge indicates that the electric field of the oil calculated by the space charge is higher than that based on the Maxwell-Wagner theory.

8.2 Future work

The purpose-built PEA system has been used to investigate the temperature gradient effect on the space charge of multilayer oil and PB throughout the thesis. The different temperature gradient effect on the space charge behaviour has been investigated. However, more specifically, the constant high temperature (such as 60°C) effect on the space charge behaviour of multilayer oil and PB still needs to be investigated, which could mimic the charge dynamics in hot spot areas of converter transformers. Different electric fields can be measured for space charge behaviour, and the electric field can increase from a current of 10 kV/mm to 20 kV/mm under the temperature gradient to investigate the potential to decrease the dimension, weight, and material usage of converter transformers. The bend of the oil-impregnated PB space charge behaviour under the temperature gradient should be investigated, which could be beneficial for space charge dynamics understanding in real converter transformers. The bubble can be injected into the oil of two-layer oil and PB samples to investigate the relationship between the space charge dynamics and the partial discharge. Furthermore, the different thickness ratios, ageing effect, moisture, and AC+DC voltage effect on the dynamics in multilayer oil and PB under a temperature gradient should be investigated to improve the understanding of the space charge behaviour in oil and PB.

The dynamics of space charge under DC voltage in new insulation material such as nano-modified cellulose paper or natural ester oil, which is served as an alternative to the traditional mineral oil and PB due to the cost reduction and environment concerns, still requires the further investigations.

The space charge is further interpolated into the COMSOL software to calculate the electric field with the emphasis on the electric field after the PR operation. The electric field is also calculated by the conventional Maxwell-Wagner theory for comparison. However, the current model still calculates the electric field under the ambient temperature. The temperature effect on the Maxwell-Wagner theory should be considered to compare the electric field calculated by the space charge under the same conditions. The measured space charge is interpolated into the COMSOL model for specific layers of oil and PB. However, an algorithm should be proposed to calculate the electric field distribution of a whole converter transformer based on the space charge distribution. To achieve that, the ionisation model for one layer of oil should be proposed; then, with the bipolar charge transport model, the two-layer oil and PB space charge distribution can be simulated.

The limitation of the current space charge interpolation method is that it is based on the space charge being measured under the ambient temperature. However, the temperature gradient factor

could also be considered and entered, via charge interpolation, into the model, based on the space charge measured under the temperature gradient. In addition, a space charge interpolation method is proposed that can simulate the electric field of the thick multi-layers of oil and PB under the ambient temperature. The relevant space charge must still be measured in order to compare measured space charge with the estimated space charge results. To achieve this aim, new PEA equipment should be set up. Moreover, different electric fields can be measured for the space charge of the multi-layers of oil and PB. In regards to the different parts of the converter transformer, the insulation materials may withstand different electric fields due to the different thickness ratios of oil and PB. The space charge measured under different electric fields can be further interpolated into a whole converter transformer, enabling the calculation of the electric field.

The flow of the oil effect on the space charge of two-layer oil and PB should be considered. A purpose-built PEA system should be built to realise it. The flow of the oil effect on the space charge of two layers of oil and PB can also be investigated with consideration of the temperature effect. A model could be proposed to simulate the flow of the oil effect on the space charge distribution in a whole converter transformer.

References

[1] WEEDY. B. M., CORY. B. J., JENKINS. N, EKANAYAKE. J. B, and STRBAC. G, *Electric Power Systems*, Fifth ed. John Wiley&Sons, Ltd, 2012.

[2] B. Qi, X. Zhao, C. Li, and H. Wu, "Transient Electric Field Characteristics in Oil-Pressboard Composite Insulation under Voltage Polarity Reversal," *IEEE Trans. Dielectr. Electr. Insul.*, vol. 22, no. 4, pp. 2148–2155, 2015.

[3] B. Huang, M. Hao, Z. Xu, G. Chen, and T. Chao, "Effect of Voltage Reversal on Space Charge in Oil and Oil-impregnated Pressboard under Temperature Gradient," in *IEEE International Conference on the Properties and Application of Dielectric Materials*, 2018, pp. 98–101.

[4] J. S. Chahal and C. C. Reddy, "Modeling and Simulation of Pulsed Electroacoustic Measurement Method," *IEEE Syst. J.*, vol. 8, no. 4, pp. 1283–1292, 2014.

[5] M. J. Heathcote, *The J&P Transformer Book*, 13th ed. Elsevier Ltd, 2007.

[6] A. Roberto and T. Campos, "Simulation of a Distribution Transformer," *WSEAS Trans. FLUID Mech.*, vol. 7, no. 3, pp. 106–115, 2012.

[7] H. Okubo, *Handbook of Electric Power Engineering (in Japanese)*. Ohmsha publication Ltd.

[8] M. Hao, "Oil/paper Insulation HVDC Performance," University of Southampton, 2015.

[9] A. Küchler, U. Piovan, M. Berglund, G. Chen, A. Denat, J. Fabian, R. Fritsche, and T. Grav, "CIGRE Technical Brochure No. 646: HVDC Transformer Insulation: Oil Conductivity," 2016.

[10] A. Küchler, *High Voltage Engineering Fundamentals Technology Applications*. Springer Vieweg, 2018.

[11] H. Okubo, R. Nakane, K. Takabayashi, and K. Kato, "Electric Field Distribution with Dynamic Charge Activity in Composite Insulation Systems under HVDC and DC-Polarity Reversal Conditions," in *Electrical Insulation and Dielectric Phenomenon (CEIDP)*, 2017, pp. 600–604.

[12] H. Okubo, T. Nara, H. Saito, H. Kojima, N. Hayakawa, and K. Kato, "Breakdown Characteristics in Oil/Pressboard Composite Insulation System at HVDC polarity reversal," in *Annual Report Conference on Electrical Insulation and Dielectric Phenomena*, 2010, pp. 1–4.

[13] P. Morshuis and M. Jeroense, "Space Charge Measurements on Impregnated Paper: A Review of the PEA Method and a Discussion of Results," *IEEE Electr. Insul. Mag.*, vol. 13, no. 3, pp. 26–35, 1997.

[14] P. M. Mitchinson, "Surface Tracking in the Inter-phase Region of Large Transformers," University of Southampton, 2008.

[15] B. Huang, M. Hao, Z. Xu, G. Chen, X. Wang, Q. Wang, and Y. Long, "Temperature Gradient Effect on the Space Charge Behaviour in Thick Oil and Oil-impregnated Pressboard," in *IEEE International Conference on Dielectric Liquids (ICDL)*, 2017, pp. 1–5.

[16] R. Bodega, P. H. T. Morshuis, and J. J. Smit, "Space Charge Measurements on Multi-dielectrics by Means of the Pulsed Electroacoustic Method," *IEEE Trans. Dielectr. Electr. Insul.*, vol. 13, no. 2, pp. 272–281, 2006.

[17] T. A. Prevost and T. V. Oommen, "Cellulose Insulation in Oil-Filled Power Transformers:

Part I - History and Development," *IEEE Electr. Insul. Mag.*, vol. 22, no. 1, pp. 28–34, 2006.

[18] J. Bidlack, M. Malone, and R. Benson, "Molecular Structure and Components Integration of Secondary Cell Walls in Plants," *Proc.Okla.Acad.Sci.*, vol. 72, pp. 51–56, 1992.

[19] M. C. Silva, O. R. Lopes, J. L. Colodette, a. O. Porto, J. Rieumont, D. Chaussy, M. N. Belgacem, and G. G. Silva, "Characterization of Three non-product Materials from a Bleached Eucalyptus Kraft Pulp Mill, in view of Valorising them as a Source of Cellulose Fibres," *Ind. Crops Prod.*, vol. 27, no. 3, pp. 288–295, 2008.

[20] L. Ruijin, L. Haibin, B. Ge, H. Jian, L. Xiao, and L. Yuandi, "Space Charge Characteristics and Dielectric Properties of Nano-SiO2/Aramid Paper Composite," *Trans. China Electrotech. Soc.*, vol. 31, no. 12, pp. 40–48, 2016.

[21] L. Ruijin, L. Tuan, Y. Lijun, L. Cheng, and W. Weiqiang, "Space Charge Characteristics of Cellulose Insulation Paper with Nano-modified Under DC Field," *High Volt. Eng.*, vol. 41, no. 9, pp. 3006–3013, 2015.

[22] L. Ruijin, L. Cheng, W. Weiqiang, L. Tuan, and L. Haibin, "Insulating Property of Insulation Paper Modified by Nano-TiO2," *High Volt. Eng.*, vol. 40, no. 7, pp. 1932–1939, 2014.

[23] L. Ruijin, C. L V, W. Weiqiang, L. Ningchuan, and Y. Lijun, "Insulating Properties of Insulation Paper Modified by Nano-Al2O3 for Power Transformer," *J. Electr. Power Sci. Technol.*, vol. 29, no. 1, 2014.

[24] L. Cheng, L. Ruijin, W. Weiqiang, and L. Tuan, "Influence of Nano-TiO_2 on DC Space Charge Characteristics of Oil-paper Insulation Material," *High Volt. Eng.*, vol. 41, no. 2, pp. 417–423, 2015.

[25] British Standards Institution, "BS 5730:2001 Monitoring and maintenance guide for mineral insulating oils in electrical equipment," 2001.

[26] Z. Yuan, "Electrical Properties of Mineral Oil and Oil/Impregnated Pressboard For HVDC Converter Transformers," Univerisity of Southampton, 2015.

[27] X. Wang and Z. D. Wang, "Study of Dielectric Behavior of Ester Transformer Liquids under AC Voltage," *IEEE Trans. Dielectr. Electr. Insul.*, vol. 19, no. 6, pp. 1916–1925, 2012.

[28] C. Patrick McShane, J. Corkran, K. Rapp, and J. Luksich, "Natural Ester Dielectric Fluid development," in *Transmission and Distribution Conference and Exhibition*, 2006, pp. 1–5.

[29] X. Wang, C. Tang, B. Huang, J. Hao, and G. Chen, "Review of Research Progress on the Electrical Properties and Modification of Mineral Insulating Oils Used in Power Transformers," *Energies*, vol. 11, no. 3, pp. 1–31, 2018.

[30] I. Fofana, V. Wasserberg, H. Borsi, and E. Gockenbach, "Challenge of Mixed Insulating Liquids for Use in High-voltage Transformers.2. Investigation of Mixed Liquids Impregnated Paper Insulation," *IEEE Electr. Insul. Mag.*, vol. 18, no. 3, pp. 5–16, 2002.

[31] I. Fofana, V. Wasserberg, H. Borsi, and E. Gockenbach, "Challenge of Mixed Insulating Liquids for Use in High-Voltage Transformers,Part 1: Investigation of Mixed Liquids," *IEEE Electr. Insul. Mag.*, vol. 18, no. 3, pp. 18–31, 2002.

[32] Y. Bertrand and L. C. Hoang, "Vegetal Oils as Substitute for Mineral Oils," in *Proceedings of the International Conference on Properties and Applications of Dielectric Materials*, 2003, vol. 2, pp. 491–494.

[33] A. Imburgia, "Modelling of Pulsed Electro Acoustic Method for Space Charge Detection

on Single and Multilayer Dielectrics," University of Palermo, 2018.

[34] K. Wu, Q. Zhu, H. Wang, X. Wang, and S. Li, "Space Charge Behavior in the Sample with Two Layers of Oil-Immersed-Paper and Oil," *IEEE Trans. Dielectr. Electr. Insul.*, vol. 21, no. 4, pp. 1857–1865, 2014.

[35] Y. Wang, "Breakdown Characteristics of Oil and Pressboard Insulation in Converter Transformer," Harbin University of Science and Technology, 2013.

[36] J. Zhao, "Dynamics of Space Charge and Electroluminescence Modelling In Polyethylene," Univeristy of Southampton, 2012.

[37] N. Ando and F. Numajiri, "Experimental Invstigation of Space Charge in XLPE Cable Using Dust Figure," *IEEE Trans. Electr. Insul.*, vol. 14, no. 1, 1979.

[38] M. S. Khalil and B. S. Hansen, "Investigation of Space Charge in Low-Density Polyethylene Using a Field Probe Technique," *IEEE Trans. Electr. Insul.*, vol. 23, no. 3, pp. 441–445, Jun. 1988.

[39] R. E. Collins, "Analysis of Spatial Distribution of Charges and Dipoles in Electrets by a Transient Heating Technique," *J. Appl. Phys.*, vol. 47, no. 11, pp. 4804–4808, 1976.

[40] T. Pawlowski, R. J. Fleming, and S. B. Lang, "LIMM Study of Space Charge in Crosslinked Polyethylene," *IEEE Trans. Dielectr. Electr. Insul.*, vol. 13, no. 5, pp. 1023–1029, Oct. 2006.

[41] Y. Suzuoki, H. Muto, T. Mizutani, and M. Ieda, "Investigation of Space Charge in High-Density Polyethylene Using Thermal-Pulse Response," *Jpn. J. Appl. Phys.*, vol. 24, no. 5, pp. 604–609, 1985.

[42] S. Agnel, P. Notingher, and A. Toureille, "Space Charge Measurements Under Applied DC Field by The Thermal Step Method," in *Electrical Insulation and Dielectric Phenomena*, 2000, pp. 166–170.

[43] T. Andritsch, "Epoxy Based Nanodielectrics for High Voltage DC Applications: Synthesis, Dielectric Properties and Space Charge Dynamics," Delft Univeristy of Technology, 2010.

[44] Q. Zhu, "Study on Space Charge Migration Properties of Oil-impregnated Paper under DC Voltage," Xi'an Jiaotong University, 2014.

[45] "IEC/TS 62758:2012 Calibration of Space Charge Measuring Equipment Based on Pulsed Electroacoustic (PEA) Measurement Principle," PD IEC/TS 62758, 2012.

[46] Y. Li, K. Murata, Y. Tanaka, T. Takada, and M. Aihara, "Space Charge Distribution Measurement in Lossy Dielectric Materials by Pulsed Electroacoustic Method," in *Proceedings of 1994 4th International Conference on Properties and Applications of Dielectric Materials (ICPADM)*, 1994, pp. 725–728.

[47] A. Vázquez, G. Chen, A. E. Davies, and R. Bosch, "Space Charge Measurement using Pulsed Electroacoustic Technique and Signal Recovery," *J. Eur. Ceram. Soc.*, vol. 19, no. 6–7, pp. 1219–1222, 1999.

[48] C. Tang, B. Huang, M. Hao, Z. Xu, J. Hao, and G. Chen, "Progress of Space Charge Research on Oil-Paper Insulation Using Pulsed Electroacoustic Techniques," *Energies*, vol. 9, no. 1, p. 53, 2016.

[49] X. Chen, X. Wang, K. Wu, Z. Peng, and Y. Cheng, "Effect of Temperature Gradient on Space Charge Waveform in Pulsed Electroacoustic Method," *ACTA Phys. Sin.*, vol. 59, no. 10, pp. 7327–7332, 2010.

[50] Q. Zhu, K. Wu, H. Wang, W. Xia, and S. Lv, "The Study of PEA Space Charge Waveform Recovery under Temperature Gradient," in *IEEE International Conference on Solid Dielectrics*, 2013, pp. 464–467.

[51] H. Wang, K. Wu, Q. Zhu, and X. Wang, “Recovery Algorithm for Space Charge Waveform under Temperature Gradient in PEA Method,” *IEEE Trans. Dielectr. Electr. Insul.*, vol. 22, no. 2, pp. 1213–1219, 2015.

[52] M. Fu and G. Chen, “Space Charge Measurement in Polymer Insulated Power Cables Using Flat Ground Electrode PEA System,” *Sci. Meas. Technol.*, vol. 150, no. 2, pp. 89–96, 2003.

[53] X. Wang, C. Chen, J. Hao, K. Wu, X. Chen, W. Li, and C. Zhang, “Recovery Algorithm for Space Charge Waveform in Coaxial Cable under Temperature Gradient,” *Sensors Mater.*, vol. 29, no. 8, pp. 1147–1157, 2017.

[54] D. Fabiani, G. C. Montanari, C. Laurent, G. Teyssedre, P. H. F. Morshuis, R. Bodega, and L. A. Dissado, “HVDC Cable Design and Space Charge Accumulation. Part 3 Effect of Temperature Gradient,” *IEEE Electr. Insul. Mag.*, vol. 24, no. 2, pp. 5–14, 2008.

[55] D. Fabiani, G. C. Montanari, R. Bodega, P. H. F. Morshuis, C. Laurent, and L. A. Dissado, “The Effect of Temperature Gradient on Space Charge and Electric Field Distribution of HVDC Cable Models,” in *IEEE International Conference on Properties and Applications of Dielectric Materials*, 2006, pp. 65–68.

[56] X. Chen, X. Wang, K. Wu, Z. R. Peng, Y. H. Cheng, and D. M. Tu, “Effect of Voltage Reversal on Space Charge and Transient Field in LDPE Films under Temperature Gradient,” *IEEE Trans. Dielectr. Electr. Insul.*, vol. 19, no. 1, pp. 140–149, 2012.

[57] “IEC, BS EN 61378-2:2001, Convertor Transformers — Part 2: Transformers for HVDC applications,” 2001.

[58] “BS IEC 61378-3:Converter Transformers Part 3 : Application guide,” BSI Standards Publication, 2015.

[59] R. F. Dudley, D. Ahuja, S. Andersson, and A. Jack, “IEEE Standard for General Requirements and Test Code for Oil-Immersed HVDC Converter Transformers,” 2008.

[60] G. Chen, T. Y. G. Tay, A. E. Davies, Y. Tanaka, and T. Takada, “Electrodes and Charge Injection in Low-density Polyethylene Using the Pulsed Electroacoustic Technique,” *IEEE Trans. Dielectr. Electr. Insul.*, vol. 8, no. 6, pp. 867–873, 2001.

[61] Y. Zhou, M. Huang, Q. Sun, Y. Sha, F. Jin, and L. Zhang, “Space Charge Characteristics in Two-Layer Oil-Paper Insulation,” *J. Electrostat.*, vol. 71, no. 3, pp. 413–417, 2013.

[62] T. V. Oommen and T. A. Prevost, “Cellulose Insulation in Oil-Filled Power Transformers: Part II - Maintaining Insulation Integrity and Life,” *IEEE Electr. Insul. Mag.*, vol. 22, no. 2, pp. 5–14, 2006.

[63] “IEC/TS 60076-14:2009 Power transformers- Part 14: Design and Application of Liquid-Immersed Power Transformers using High-Temperature Insulation Materials,” 2009.

[64] J. Hao, G. Chen, R. Liao, L. Yang, and C. Tang, “Influence of Moisture on Space Charge Dynamics in Multilayer Oil-Paper Insulation,” *IEEE Trans. Dielectr. Electr. Insul.*, vol. 19, no. 4, pp. 1456–1464, 2012.

[65] P. H. F. Morshuis, R. Bodega, D. Fabiani, G. C. Montanari, L. A. Dissado, and J. J. Smit, “Dielectric Interfaces in DC Constructions: Space Charge and Polarization Phenomena,” in *International Conference on Solid Dielectrics*, 2007, pp. 450–453.

[66] K. Wu and C. Cheng, “Interface Charges between Insulating Materials,” *IEEE Trans. Dielectr. Electr. Insul.*, vol. 24, no. 4, pp. 2633–2642, 2017.

[67] G. Chen, Y. Tanaka, T. Takada, and L. Zhong, “Effect of Polyethylene Interface on Space Charge Formation,” *IEEE Trans. Dielectr. Electr. Insul.*, vol. 11, no. 1, pp. 113–121, 2004.

[68] T. T. N. Vu, G. Teyssedre, B. Vissouvanadin, S. L. Roy, and C. Laurent, “Correlating

Conductivity and Space Charge Measurements in Multi-dielectrics under Various Electrical and Thermal Stresses," *IEEE Trans. Dielectr. Electr. Insul.*, vol. 22, no. 1, pp. 117–127, 2015.

[69] P. Liu, H. Feng, H. Zhang, X. Ning, D. Li, and Z. Peng, "Characteristics of Space Charge Distribution in Epoxy-paper Composite Insulation System," *IEEE Trans. Dielectr. Electr. Insul.*, vol. 23, no. 4, pp. 2385–2392, 2016.

[70] Y. Gong, "Design of the Variable Temperature Measurement System of Space Charge," Harbin University of Science and Technology, 2013.

[71] M. Reading, Z. Xu, A. S. Vaughan, and P. L. Lewin, "On Sample Preparation and Dielectric Breakdown in Nanostructured Epoxy Resins," *J. Phys.*, vol. 310, no. 1, 2011.

[72] I. Iddrissu, "Study of Electrical Strength and Lifetimes of Polymeric Insulation for DC Applications," University of Manchester, 2016.

[73] Y. You, "Design of Variable Temperature Measurement System of Space Charge," Harbin University of Science and Technology, 2013.

[74] P. Yin, "Space Charge Measurement under Different Electrical Field Intensity and Temperature Gradient in Oil-paper Insulation," Harbin University of Science and Technology, 2017.

[75] C. Zhou, "Space Charge Dynamics in Polyethylene under Periodical High Voltage Electric Fields," University of Southampton, 2017.

[76] T. Takada, T. Maeno, and H. Kushibe, "An Electric Stress Pulse Technique for the Measurement of Charges in a Plastic Plate Irradiated by an Electron beam," in *Intern. Symp. Electrets*, 1985, pp. 450–455.

[77] X. Chen, X. Wang, K. Wu, Z. R. Peng, Y. H. Cheng, and D. M. Tu, "Space Charge Measurement in LPDE Films under Temperature Gradient and DC Stress," *IEEE Trans. Dielectr. Electr. Insul.*, vol. 17, no. 6, pp. 1796–1805, 2010.

[78] B. Huang, M. Hao, Z. Xu, G. Chen, X. Wang, C. Tang, J. Hao, and Q. Wang, "Effect of Temperature Gradient on Space Charge in Multilayres Pressboard Oil and Pressboard system," in *IEEE Conference on Electrical Insulation and Dielectric Phenomenon (CEIDP)*, 2017, pp. 74–77.

[79] M. J. P. JEROENSE, "Charges and Discharges in HVDC Cables," Delft Univeristy of Technology, 1997.

[80] C. Tang, B. Huang, J. Hao, M. Hao, S. Guo, and G. Chen, "The Space Charge Behaviors of Insulation Paper immersed by Mineral Oil and MIDEL 7131 after Thermal Ageing," in *International Conference on Condition Monitoring and Diagnosis (CMD)*, 2016, pp. 44–47.

[81] C. Tang, G. Chen, M. Fu, and R. J. Liao, "Space Charge Behavior in Multi-layer Oil-paper Insulation under Different DC Voltages and Temperatures," *IEEE Trans. Dielectr. Electr. Insul.*, vol. 17, no. 3, pp. 775–784, 2010.

[82] M. Fu, L. A. Dissado, G. Chen, and J. C. Fothergill, "Space Charge Formation and its Modified Electric Field under Applied Voltage Reversal and Temperature Gradient in XLPE Cable," *IEEE Trans. Dielectr. Electr. Insul.*, vol. 15, no. 3, pp. 851–860, 2008.

[83] X. Wang, H. Q. He, D. M. Tu, C. Lei, and Q. G. Du, "Dielectric Properties and Crystalline Morphology of Low Density Polyethylene blended with Metallocene Catalyzed Polyethylene," *IEEE Trans. Dielectr. Electr. Insul.*, vol. 15, no. 2, pp. 319–326, 2008.

[84] Z. Wang, "Wave Velocities in Hydrocarbons and Hydrocarbon Saturated Rocks," Stanford University, 1988.

[85] Z. Lv, K. Wu, X. Wang, Y. Cheng, and Dissado.L.A, "Simulation of Space Charge Distribution in Polyethylene under a Temperature Gradient," in *Conference on Electrical Insulation and Dielectric Phenomena*, 2014, pp. 879–882.

[86] Q. Zhu, X. Wang, K. Wu, Y. Cheng, Z. Lv, and H. Wang, "Space Charge Distribution in Oil Impregnated Papers under Temperature Gradient," *IEEE Trans. Dielectr. Electr. Insul.*, vol. 22, no. 1, pp. 142–151, 2015.

[87] M. Hao, G. Chen, X. Chen, C. Zhang, W. Li, H. Wang, M. Zhou, and X. Lei, "Study of Space Charge Dynamics in Oil and Pressboard Composite System under Different Polarity Reversal Voltages," *Sensors Mater.*, vol. 29, no. 8, pp. 1109–1122, 2017.

[88] K. Wu, X. Chen, X. Wang, Z. Wang, Y. Cheng, and Z. Peng, "Effects of Temperature Gradient on Space Charge Accumulation at Applied Voltage Reversal in LDPE Film," in *International Conference on Solid Dielectrics*, 2010, pp. 1–4.

[89] M. Hao, Y. Zhou, G. Chen, G. Wilson, and P. Jarman, "Space Charge Behaviour in Oil Gap and Impregnated Pressboard Combined System under HVDC Stresses," *IEEE Trans. Dielectr. Electr. Insul.*, vol. 23, no. 2, pp. 848–858, 2016.

[90] P. M. Mitchinson, P. L. Lewin, B. D. Strawbridge, and P. Jarman, "Tracking and Surface Discharge at the Oil-Pressboard Interface," *IEEE Electr. Insul. Mag.*, vol. 26, no. 2, pp. 35–41, 2010.

[91] D. Fabiani, G. C. Montanari, L. A. Dissado, C. Laurent, and G. Teyssedre, "Fast and Slow Charge Packets in Polymeric Materials under DC Stress," *IEEE Trans. Dielectr. Electr. Insul.*, vol. 16, no. 1, pp. 241–250, 2009.

[92] T. Hori, K. Kaneko, T. . Mizutani, and M. Ishioka, "Space Charge Distribution in Low-density Polyethylene with Blocking Layer," in *2003 Annual Report Conference on Electrical Insulation and Dielectric Phenomena*, 2003, pp. 197–200.

[93] B. Huang, M. Hao, J. Hao, J. Fu, Q. Wang, and G. Chen, "Space Charge Characteristics in Oil and Oil-Impregnated Pressboard Insulation and Electric Field Distortion after Polarity Reversal Operation," *IEEE Trans. Dielectr. Electr. Insul.*, vol. 23, no. 2, pp. 881–891, 2016.

[94] M. Hao, Y. Zhou, G. Chen, G. Wilson, and P. Jarman, "Space Charge Behaviour in Thick Oil-Impregnated Pressboard under HVDC Stresses," in *IEEE International Conference on Solid Dielectrics (ICSD)*, 2013, pp. 397–400.

[95] L. Lan, J. Wu, Y. Yin, X. Li, and Z. Li, "Effect of Temperature on Space Charge Trapping and Conduction in Cross-linked Polyethylene," *IEEE Trans. Dielectr. Electr. Insul.*, vol. 21, no. 4, pp. 1784–1791, Aug. 2014.

[96] Y. Murakami and G. Chen, "Influence of Film Thickness on Space Charge Formation under DC Ramp Voltage," in *IEEE International Conference on Solid Dielectrics*, 2013, no. 1, pp. 448–451.

[97] B. Huang, M. Hao, Z. Xu, G. Chen, C. Tang, and J. Hao, "Research on Thickness Ratio and Multilayers effect on the Oil and Paper Space Charge Distribution," in *International Conference on Condition Monitoring and Diagnosis (CMD)*, 2016, pp. 40–43.

[98] G. Chen and Z. Xu, "Charge Trapping and Detrapping in Polymeric Materials," *J. Appl. Phys.*, vol. 106, no. 12, pp. 1–5, 2009.

[99] L. Lan, Q. Zhong, Y. Yin, and X. Li, "Effect of Surface Fluorination on Space Charge Behavior at LDPE/EPDM Interface," in *IEEE International Conference on Solid Dielectrics (ICSD)*, 2013, pp. 444–447.

[100] R. Bodega, P. H. F. Morshuis, U. H. Nilsson, G. Perego, and J. J. Smit, "Charging and Polarization Phenomena in XLPE-EPR Coaxial Interfaces," in *International Symposium on Electrical Insulating Materials, (ISEIM)*, 2005, pp. 107–110.

[101] R. Bodega, P. H. F. Morshuis, U. H. Nilsson, G. Perego, and J. J. Smit, “Polarization Mechanisms of Flat XLPE-EPR Interfaces,” in *Proceedings of Nordic Insulation Symposium*, 2005, pp. 224–227.

[102] R. Bodega, G. Perego, P. H. F. Morshuis, U. H. Nilsson, and J. J. Smit, “Space Charge and Electric Field Characteristics of Polymeric-type MV-size DC Cable Joint Models,” in *Annual Report Conference on Electrical Insulation and Dielectric Phenomena*, 2005, pp. 507–510.

[103] C. Zhou and G. Chen, “Space Charge and AC Electrical Breakdown Strength in Polyethylene,” *IEEE Trans. Dielectr. Electr. Insul.*, vol. 24, no. 1, pp. 559–566, 2017.